Karlsruhe Institute of Technology

Geophysical Institute KIT-Dept. of Physics

TOWARDS THE APPLICATION OF 2D ELASTIC FULL-WAVEFORM INVERSION TO ULTRASONIC DATA FOR NON-DESTRUCTIVE TESTING

ANWENDUNG 2D ELASTISCHE WELLENFORMINVERSION VON ULTRASCHALLDATEN FÜR DIE ZERSTÜRUNGSFREIE MATERIALPRÜFUNG

Master's Thesis of

Priscilla Ntengue Chatue

KIT - Department of Physics

Geophysical Institute (GPI)

Date of submission:

12.05.2021

Reviewer:	Prof. Dr. Thomas Bohlen
Second reviewer:	apl. Prof. Dr. Joachim Ritter

Abstract

Non-destructive testing (NDT) has been used over the last years to test materials in order to assure safety and improve product reliability. It usually makes use of ultrasonic waves. This study aims to evaluate if the 2D elastic full-waveform inversion (FWI) of ultrasonic waves can reconstruct the properties of materials in a pipe embedded in a concrete block. The data were acquired at the Fraunhofer Institute for Non-Destructive Testing (IZPF). Prior to the inversion of lab data, synthetic inversion tests on numerically modelled waves are conducted to investigate the feasibility of such a test. On one hand, full data content inversion only simulates the position and shape of the pipe. On the other hand, the inversion of tapered transmitted waves partly displays the characteristics of the material in the pipe. Improvement in result leads to perform a cross talk test, which shows that the high velocity contrast between the concrete and materials in the pipe may contribute to the bad resolution imaging. In the realistic application, only tapered transmitted waves are inverted due to the complexity of late arrivals coda. It was possible to either locate the pipe to an extend but not to size it correctly or designate the material in it. Comparison between modelled and lab data show that in addition to the high velocity contrast, the directivity feature of the transducers might strongly affect inversion. Further tests need to be carried on to assess the hypothesis.

Contents

Chapter 1

Introduction

In the realistic world, we do not often have information about the subsurface, which could explain observations made on the surface. This has been of major interest all over the years. Early methods like tomography uses only the travel time of the different wave types to derive the subsurface parameters. This often results in not so accurate imaging. To ameliorate this, Tarantola (1984) developed a new method called full-waveform inversion (FWI). Unlike early methods, FWI uses the full data information contained in both amplitude and phase to accurately derive the subsurface properties. It focuses on fitting modelled and real data by minimising the error between them. The process is repeated iteratively until a proper model to explain the observations is reached. This results in some high resolution image about the subsurface. The high resolution capability of FWI over the years, made FWI to be applied to other fields than geophysics. FWI shows some good results in discipline like medicine (Agudo et al., 2018), in civil engineering (van der Kruk et al., 2014) and exploration seismic (Asgharzadeh et al., 2018) among others. Recently FWI was applied to non-destructive testing (NDT) for the material.

NDT aims at testing and analysing material component or structure without damaging them. This test usually helps to identify and evaluate the state of flaws or inclusion contained in structures. This is of particular interest as all man-made structures usually deteriorate over the years. So using NDT, potential accidents can be prevented. This made NDT to be applied to evaluate the reliability of materials in bridges, pipelines, aircraft or power stations. Various methods exist to perform NDT. These are for example visual testing, magnetic particle or ultrasonic testing. The latter is widely used, as high frequency ultrasound waves are propagated through a structure and analysed to detect imperfections. To analyse these ultrasonic waves, common methods like the synthetic aperture focusing technique (SAFT) (Baby et al., 2004) or the model-based iterative reconstruction (MBIR) (Almansouri et al., 2017) have been used. These methods proved to be limited as far as complex structures with strong inhomogeneities are concerned. Moreover, they reconstruct the size and position of anomalies

but provide no information about the structure properties. For these reasons, in recent studies, FWI has been applied to ultrasonic data in the domain of NDT. Seidl and Rank (2016) successfully apply FWI to synthetic ultrasonic data for the detection of a flaw in a damaged aluminium plate. They also show that the number of sensors and their relative position to the flaw strongly affect the inversion results. Then Rao et al. (2016a) use guide wave tomography based on FWI to reconstruct the thickness maps of remaining walls in isotropic plates affected by corrosion. The irregular anomalies are reconstructed using a dense acquisition system. However, in reality, such acquisition geometry is not always feasible. Hence Rao et al. (2016b) addresses this problem by introducing a regularisation technique that synthesises missing components. In both publications, a time gate function is applied to the lab data and only the first arrivals mode use for the inversion. Likewise, Köhn et al. (2016) apply FWI to Rayleigh waves and account for the visco-elastic properties of the medium. Using FWI, low velocity anomalies due to weathering could be identified. As far as concrete structures are concerned, T. D. Nguyen et al. (2017) successfully applied FWI to detect delaminations in concrete bridge decks. This study is of particular interest, as my thesis is linked to concrete structures.

The goal of this work is to investigate if FWI can reconstruct the model properties of a pipe embedded in concrete and filled with a different medium. To achieve this, I first describe the theoretical background behind the forward and inverse problem in chapter 2. Secondly, I describe the acquisition system used when acquiring the data in chapter 3. The frequency content and quality data are then examined in chapter 4. In chapter 5, I numerically reconstruct the waves and study the wavefield. The modelled waves are inverted in chapter 6. In chapter 7, I apply FWI to the lab data. Considering the inversion result, I present my conclusion in chapter 8.

Chapter 2

Theory

This chapter will describe the theoretical background on which this work is based. In the first part, I will solve the forward problem, and in the second, the inverse one.

2.1 Forward Problem

The forward problem describes the wave propagation in a given medium. In this work, the wave equation, in an elastic medium is solved for this purpose. To solve this, the finite-difference method is used. In this part, I will derive the main equations for wave propagation in an elastic medium and present the background of the finite difference method.

2.1.1 Elastic wave equation

To derive the wave equation I follow the method described in (G. Müller, 2007). When a body is subjected to external forces, changes are observed. These changes consist of be translation, deformation and rotation. In case of infinitesimal changes, the rotation and translation terms of the displacement can be separated from the deformation term. The deformation is described by the deformation tensor ϵ_{ij} as follows:

$$\epsilon_{ij} = \frac{1}{2}\left(\frac{\partial u_i}{\partial x_j} + \frac{\partial u_j}{\partial x_i}\right) \qquad i, j \in [1, 3] \ . \tag{2.1}$$

The parameter u_i describes one element the displacement vector and x_i one element of the location vector of a particle. The tensor ϵ_{ij} is symmetric ($\epsilon_{ij} = \epsilon_{ji}$). As I mentioned earlier, a body may be subjected to external forces. These forces can either be body F or surface ones P. The latter is referred to as traction. The traction can either be normal or tangential to the body surface and is described by the stress tensor σ_{ij}. The tensor is symmetric $\sigma_{ij} = \sigma_{ji}$, therefore has six independent components. σ_{ii} and σ_{ij} are respectively the deformation and

shear components. When a body under stress shows deformation, it implies that at any time t, there is a relation between σ_{ij} and ϵ_{ij}. This usually depends on time and temperature. If we neglect temperature and consider infinitesimal deformation, the stress-strain relation is considered to be a linear one in an elastic medium. This is is called the Hook's law (Lay & Wallace, 1995)given by

$$\sigma_{ij} = C_{ijkl}\epsilon_{kl} \ , \qquad i,j,k,l \in [1,3] \tag{2.2}$$

where C_{ijkl} is the elasticity tensor. It has 81 components (9×9). Since the σ_{ij} and ϵ_{ij} are symmetric and the medium considered in this work is assumed to be an isotropic one, the stress-strain relation is now written as

$$\sigma_{ij} = \lambda\theta\delta_{ij} + 2\mu\epsilon_{ij}. \tag{2.3}$$

λ and μ, respectively, are the Lamé elasticity constant and the elasticity parameter. θ is the cubic dilatation given by $\theta = \epsilon_{11} + \epsilon_{22} + \epsilon_{33}$. δ_{ij} is the Kronecker symbol and equals 1 when $i = j$ and 0 otherwise.

Equation of motion

If the forces acting on a body are unbalanced, this body will be accelerated. This is Newton's second law. This means that the forces have to be balanced to stay at an equilibrium. The equation of motion is derived from this law. Following Newton's law, I have

$$\int_V F dV + \int_S P df = 0, \tag{2.4}$$

where dV is an element of the volume V and df an element of a surface S. The body forces F include the inertia forces and all other body forces. It can therefore be rewritten as

$$F = \underbrace{-\rho\frac{\partial^2 u_i}{\partial^2 t}}_{\text{inertia forces}} + \underbrace{f_i}_{\text{Other body forces}} \ . \tag{2.5}$$

The traction force P is related to the stress tensor as follows:

$$P_i = \sigma_{ij} n_j, \tag{2.6}$$

where n_j is the normal vector in the direction outside from the surface S. Replacing equations 2.5 and 2.6 in 2.4 gives,

$$\int_V \left(-\rho\frac{\partial^2 u_i}{\partial^2 t} + f_i\right) + \int_S \sigma_{ij} n_j df = 0. \tag{2.7}$$

Applying Gauss's divergence theorem to equation 2.7 I obtain

$$\int_V \left(-\rho \frac{\partial^2 u_i}{\partial^2 t} + f_i) + \int_V \nabla . \sigma_{ij} \right) = 0 \tag{2.8}$$

and

$$\int_V \left(-\rho \frac{\partial^2 u_i}{\partial^2 t} + f_i + \nabla . \sigma_{ij} \right) = 0 \tag{2.9}$$

If the integrand vanishes and knowing that $\frac{\partial^2 u_i}{\partial^2 t} = \frac{\partial v}{\partial t}$, equation 2.9, becomes

$$\rho \frac{\partial v_i}{\partial t} = f_i + \frac{\partial \sigma_{ij}}{\partial x_j} \tag{2.10}$$

Equation 2.10 is the final form of the equation of motion. Because I perform 2D forward modelling, I rewrite the equation 2.10 in the 2D coordinates system and obtain:

$$\rho \frac{\partial v_x}{\partial t} = \frac{\partial \sigma_{xx}}{\partial x} + \frac{\partial \sigma_{xy}}{\partial y} + f_x \tag{2.11}$$

$$\rho \frac{\partial v_y}{\partial t} = \frac{\partial \sigma_{xy}}{\partial x} + \frac{\partial \sigma_{yy}}{\partial y} + f_y \tag{2.12}$$

I replace the expression of ϵ_{ij} in equation 2.3. Introducing a source term for the stress components $\sigma_{ij,0}$ and rearranging it, I obtain:

$$\frac{\partial \sigma_{xx}}{\partial t} = (\lambda + 2\mu) \frac{\partial v_x}{\partial x} + \lambda \frac{\partial v_y}{\partial y} + \frac{\sigma_{xx,0}}{\partial t}, \tag{2.13}$$

$$\frac{\partial \sigma_{yy}}{\partial t} = \lambda \frac{\partial v_x}{\partial x} + (\lambda + 2\mu) \frac{\partial v_y}{\partial y} + \frac{\sigma_{yy,0}}{\partial t}, \tag{2.14}$$

$$\frac{\partial \sigma_{xy}}{\partial t} = \mu \left(\frac{\partial v_x}{\partial y} + \frac{\partial v_y}{\partial x} \right) + \frac{\partial \sigma_{xy,0}}{\partial t}, \tag{2.15}$$

The equations above can be written in a matrix-vector formulation as

$$\mathbf{M}^{-1} \left(\frac{\partial \vec{\zeta}}{\partial t} - \vec{b} \right) = \mathbf{Q} \vec{\zeta} \tag{2.16}$$

where $\vec{\zeta}$ and $\vec{b}$ are respectively the different wavefields and their corresponding sources. $\mathbf{M}$ and $\mathbf{Q}$ are matrices which will be defined in the following.
Adding2.13 and 2.14 gives

$$\frac{\partial \sigma_{xx}}{\partial t} + \frac{\partial \sigma_{yy}}{\partial t} = (2\lambda + 2\mu)(\frac{\partial v_x}{\partial x} + \frac{\partial v_y}{\partial y}) + \frac{\partial \sigma_{xx,0}}{\partial t} + \frac{\partial \sigma_{yy,0}}{\sigma t} \tag{2.17}$$

Assuming $\frac{\partial\tilde{\sigma}}{\partial t} = \frac{\partial\sigma_{ii}}{\partial t} - \frac{\partial\sigma_{ii,0}}{\partial t}$, and replacing it in equations 2.11 and 2.12,

$$\frac{\partial v_x}{\partial x} = \frac{1}{2\mu}\left(\frac{\partial\tilde{\sigma}_{xx}}{\partial t} - \frac{\lambda}{2\lambda+2\mu}\left(\frac{\partial\tilde{\sigma}_{xx}}{\partial t} + \frac{\partial\tilde{\sigma}_{yy}}{\partial t}\right)\right), \tag{2.18}$$

$$\frac{\partial v_y}{\partial x} = \frac{1}{2\mu}\left(\frac{\partial\tilde{\sigma}_{yy}}{\partial t} - \frac{\lambda}{2\lambda+2\mu}\left(\frac{\partial\tilde{\sigma}_{xx}}{\partial t} + \frac{\partial\tilde{\sigma}_{yy}}{\partial t}\right)\right), \tag{2.19}$$

Taking $A = \frac{\lambda+2\mu}{4\mu(\lambda+\mu)}$ and $B = -\frac{\lambda}{4\mu(\lambda+\mu)}$, i will have

$$\frac{\partial v_x}{\partial x} = A\frac{\partial\tilde{\sigma}_{xx}}{\partial t} + B\frac{\partial\tilde{\sigma}_{yy}}{\partial t}, \tag{2.20}$$

$$\frac{\partial v_y}{\partial y} = B\frac{\partial\tilde{\sigma}_{xx}}{\partial t} + A\frac{\partial\tilde{\sigma}_{yy}}{\partial t}. \tag{2.21}$$

The vectors $\vec{\zeta}$ and $\vec{b}$ have the following components considering a 2D spatial distribution:

$$\vec{\xi} = \begin{pmatrix} v_x \\ v_y \\ \sigma_{xx} \\ \sigma_{yy} \\ \sigma_{xy} \end{pmatrix} \qquad \vec{b} = \begin{pmatrix} f_x/\rho \\ f_y/\rho \\ \frac{\partial\sigma_{xx,0}}{\partial t} \\ \frac{\partial\sigma_{yy,0}}{\partial t} \\ \frac{\partial\sigma_{xy,0}}{\partial t} \end{pmatrix} \tag{2.22}$$

The Matrices $\mathbf{M}$ and $\mathbf{Q}$ are defined as follow

$$\mathbf{M} = \begin{pmatrix} \rho & 0 & 0 & 0 & 0 \\ 0 & \rho & 0 & 0 & 0 \\ 0 & 0 & A & B & 0 \\ 0 & 0 & B & A & 0 \\ 0 & 0 & 0 & 0 & \mu^{-1} \end{pmatrix} \qquad \mathbf{Q} = \begin{pmatrix} 0 & 0 & \frac{\partial}{\partial x} & 0 & \frac{\partial}{\partial y} \\ 0 & 0 & 0 & \frac{\partial}{\partial y} & \frac{\partial}{\partial x} \\ \frac{\partial}{\partial x} & 0 & 0 & 0 & 0 \\ 0 & \frac{\partial}{\partial y} & 0 & 0 & 0 \\ \frac{\partial}{\partial y} & \frac{\partial}{\partial x} & 0 & 0 & 0 \end{pmatrix} \tag{2.23}$$

$\mathbf{M}$ consists of model parameters like the ρ, the Lamé λ, μ whereas $\mathbf{Q}$ consists of spatial derivatives. The equations above are the ones implemented in the code used in this work.

2.1.2 Discretization in space and time

To solve the elastic wave equations, methods like the spectral-element method or the finite-difference method are used. The latter is implemented in the forward code I use in this work. Virieux (1986) proposed to discretize the Lamé parameters μ and λ, the particles velocities and the stresses on a standard staggered grid (SSG). This was further developed by Levander (1988). The discretization is both in space and time. I assume that my 2D model has the same grid sampling in X- and Y- direction. dh is the grid space between two adjacent points, and dt the time sampling interval between two time steps. The discretization is expressed as

follow

$$x = i \times dh, y = j \times dh, T = n \times dt, \tag{2.24}$$

where i,j are indices in X- and Y- direction and n is a specific number of time steps. The shape of a 2D SSG is shown in Figure 2.1. On one hand the Lamé parameters λ, μ, the density ρ and the normal stresses σ_{xx}, σ_{yy} (in black) are located on full grid points. On the other hand, the velocity particles (in blue) v_x, v_y are shifted by half a grid point in the x- and y-direction, respectively. Moreover the component σ_{xy} is shifted in both the x and y direction. The time derivative of the velocity and the stress can be approximated using second order centered FD as follow

$$\left.\frac{\partial v_i}{\partial t}\right|^{n+\frac{1}{2}} \approx \frac{v_i^{n+1} - v_i^n}{\mathrm{dt}} \tag{2.25}$$

$$\left.\frac{\partial \sigma_{ij}}{\partial t}\right|^{n} \approx \frac{\sigma_{ij}^{n+\frac{1}{2}} - \sigma_{ij}^{n-\frac{1}{2}}}{\mathrm{dt}} \tag{2.26}$$

Applying the same principle will help discretize equations 2.13 to 2.15 and 2.18 to 2.19 which result as:

$$\sigma_{xx,i,j}^{n+\frac{1}{2}} = \sigma_{xx,i,j}^{n-\frac{1}{2}} + \Delta t \cdot \lambda_{i,j} \left(\left.\frac{\partial v_x}{\partial x}\right|_{i,j}^{n} + \left.\frac{\partial v_y}{\partial y}\right|_{i,j}^{n} \right) + 2 \cdot \Delta t \cdot \mu_{i,j} \left.\frac{\partial v_x}{\partial x}\right|_{i,j}^{n} \tag{2.27}$$

$$\sigma_{yy,i,j}^{n+\frac{1}{2}} = \sigma_{yy,i,j}^{n-\frac{1}{2}} + \Delta t \cdot \lambda_{i,j} \left(\left.\frac{\partial v_x}{\partial x}\right|_{i,j}^{n} + \left.\frac{\partial v_y}{\partial y}\right|_{i,j}^{n} \right) + 2 \cdot \Delta t \cdot \mu_{i,j} \left.\frac{\partial v_y}{\partial y}\right|_{i,j}^{n} \tag{2.28}$$

$$\sigma_{xy,i+\frac{1}{2},j+\frac{1}{2}}^{n+\frac{1}{2}} = \sigma_{xy,i+\frac{1}{2},j+\frac{1}{2}}^{n-\frac{1}{2}} + \Delta t \cdot \mu_{i+\frac{1}{2},j+\frac{1}{2}} \left(\left.\frac{\partial v_x}{\partial y}\right|_{i+\frac{1}{2},j+\frac{1}{2}}^{n} + \left.\frac{\partial v_y}{\partial x}\right|_{i+\frac{1}{2},j+\frac{1}{2}}^{n} \right) \tag{2.29}$$

$$v_{x,i+\frac{1}{2},j}^{n+1} = v_{x,i+\frac{1}{2},j}^{n} + \frac{\Delta t}{\rho_{i+\frac{1}{2},j}} \left(\left.\frac{\partial \sigma_{xx}}{\partial x}\right|_{i+\frac{1}{2},j}^{n+\frac{1}{2}} + \left.\frac{\partial \sigma_{xy}}{\partial y}\right|_{i+\frac{1}{2},j}^{n+\frac{1}{2}} \right) \tag{2.30}$$

$$v_{y,i,j+\frac{1}{2}}^{n+1} = v_{y,i,j+\frac{1}{2}}^{n} + \frac{\Delta t}{\rho_{i,j+\frac{1}{2}}} \left(\left.\frac{\partial \sigma_{yx}}{\partial x}\right|_{i,j+\frac{1}{2}}^{n+\frac{1}{2}} + \left.\frac{\partial \sigma_{yy}}{\partial y}\right|_{i,j+\frac{1}{2}}^{n+\frac{1}{2}} \right) \tag{2.31}$$

2.1.3 Numerical dispersion and stability

To simulate the wavefield using the finite-difference, the model has to be discretized both in space and time. A small grid sampling dh and a small temporal sampling dt will ensure a good and stable result of the forward simulation. This will however require very large computational resources. Therefore a compromise was found to assure good forward modelling while minimizing the cost. This concerns the two parameters space and time.

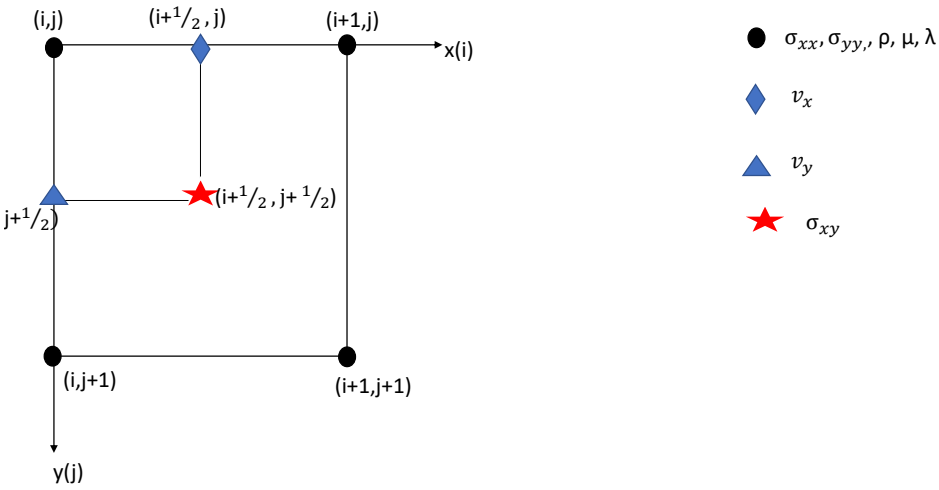

Figure 2.1: The spatial distribution of model parameters, velocities v and stresses σ on the 2D SSG. The black points mark full gridpoints while the blue half gridpoints.

Grid dispersion

To model wave propagation, there is a minimum number of points per wavelength to consider to avoid dispersion or numerical artefacts. This is called *grid dispersion*. This occurs when the space sampling dh is too large. To avoid such case, Köhn (2011) defined a stability criterion defined as

$$dh \leq \frac{\lambda_{min}}{n} = \frac{v_{min}}{n f_{max}} \tag{2.32}$$

where λ_{min} is the minimum wavelength present in the model, v_{min} the minimum velocity in the model and f_{max} the maximum frequency of the source signal. n is the number of grid points per minimum wavelength. This is a function of the finite-difference order. The different values of n as a function of the spatial difference order are resumed in Table 2.1. In this work, I perform a second-order spatial finite-difference ($n = 12$).

Table 2.1: The number of grid points per minimum wavelength as a function of the spatial FD order.

FD order	2	4	6	8	10	12
n	12	8	6	5	5	4

Numerical instability

Another type of instability that can occur during forward modelling is numerical instability. This occurs when the sampling interval dt is too big. This will increase the amplitudes so strongly that the algorithm will get unstable. Courant et al. (1928) defined a Courant-

Friedrichs-Lewy (CFL) criterion. For the elastic wave equation, CFL is defined as:

$$dt \leq \frac{dh}{h\sqrt{D}v_{max}} \tag{2.33}$$

where v_{max} is the maximum velocity in the model. h is the sum of the finite-difference coefficients and depends on the FD order. In the case of this work $h = 1$.

Initial and boundary conditions

The elastic wave equations have multiple solutions. To find a unique solution of the elastic wave equations, I need to define initial and boundary conditions. The initial condition during wave propagation states that at t=0, the model is at equilibrium. This means that the velocity and stresses are zero at any grid points on the model

$$v_x \mid_{t=0} = v_y \mid_{t=0} = 0 \tag{2.34}$$

$$\sigma_{xx} \mid_{t=0} = \sigma_{yy} \mid_{t=0} = \sigma_{xy} \mid_{t=0} = 0 \tag{2.35}$$

The aim of forward modelling is to simulate wave propagation as real as possible. For this reason, a free surface is implemented as a boundary condition in this work. There are many methods to implement the free surface condition. Zahradník et al. (1993) introduced the vacuum formulation (VF). This states that above the free surface, v_p, v_s, ρ equal zero. However, this method showed some limits and was later improved by Zeng et al. (2012) who named it improved vacuum formulation (IVF).

2.2 Inverse problem

The search for information about the Earth has always been of interest. Many methods like tomography have been developed to serve the purpose. Unlike tomography which only uses the first arrival times of P-or S-waves to define the model properties, FWI makes use of the full information contained in both the amplitudes and phases of the data. FWI was first developed by Tarantola (1984). The general algorithm of FWI is shown in Figure 2.2. First, a proper initial model m_0 is chosen. This model should ideally be not far from the real one, though we don't have any informations about it in the reality. To construct such, the known pieces of information about the test field are used. Using this initial model, pseudo-observed data $\vec{d}_{syn}$ are modelled. Second the misfit function E between the observed data $\vec{d}_{obs}$ and $\vec{d}_{syn}$ is evaluated. If the misfit is smaller than a defined abort criterion, the inversion stops and the final model is obtained. Otherwise, the residuals wavefield is backpropagated. Then the gradient of the misfit is calculated and the model updated using equation

$$m_{n+1} = m_n - \alpha \nabla_m E_n \tag{2.36}$$

The parameter α is a scalar called the step length. Equation 2.36 is a generalised equation form to update the model. This is not implemented in the code used in this study. Instead I use the conjugate gradient method introduced by Nocedal and Wright (2006). Here equation 2.36 is only used in the first iteration and from the second iteration the following equation is used.

$$m_{i+1} = m_i - \alpha_i A_i \nabla_m \overline{E_i} \tag{2.37}$$

with

$$\nabla_m \overline{E_i} = \nabla_m E_i - \beta_i \nabla_m \overline{E}_{i-1} \tag{2.38}$$

A is a preconditioning matrix calculated with the K1 method introduced by Plessix and Mulder (2004). The parameter β_n according to Polak and Ribiere (1969) is defined by:

$$\beta_i = \frac{(\nabla_m E_i)^T (\nabla_m E_i - \nabla_m E_{i-1})}{||\nabla E_i - 1||^2}. \tag{2.39}$$

The steps above are repeated until the misfit function is so small, that the model m is good enough to explain the observed data.

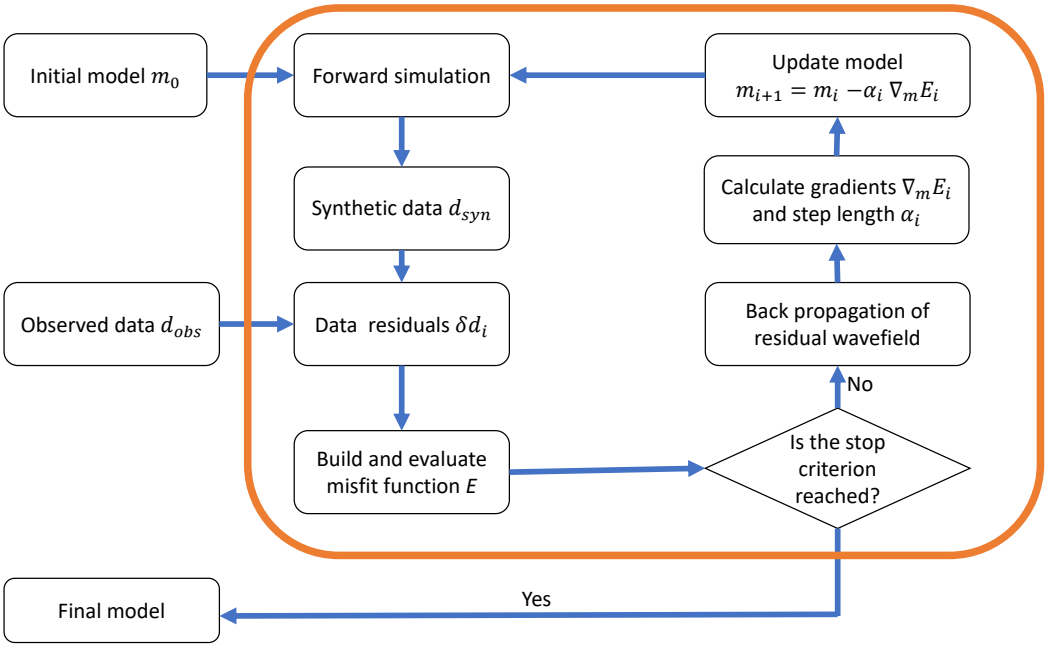

Figure 2.2: Full-waveform inversion algorithm. The steps in the orange box are repeated iteratively until the data fitting is good.

2.2.1 The misfit function

The goal of FWI is to minimise the misfit function between the synthetic modelled and observed data (Fichtner, 2010). The residuals between them is defined as

$$\Delta \vec{d} = \vec{d}_{syn} - \vec{d}_{obs}. \tag{2.40}$$

The $L2$-norm is the misfit used in this study and is defined as:

$$E(m) = \frac{1}{2} \int_x \int_0^T \Delta \vec{d}^2 dt dx \tag{2.41}$$

Equation 2.41 is only valid for one source. To account for each source and receiver position, the misfit is summed. During inversion, if the misfit value is bigger than the stop criterion, the inversion goes on to the next stage and the residuals wavefields are backpropagated. Then the gradient of the misfit function is calculated with the adjoint state method. Details about the method are given in the next section.

2.2.2 The adjoint state method

The FWI problem is a non-linear one. This leads to multiple global minima. FWI problem is linearised to solve this issue. Its linearisation using classical methods will use Fréchet derivatives which are computationally expensive. For this reason the adjoint-state method is introduced in FWI. The method described in this section is from Plessix (2006). The misfit E is defined by a functional h

$$E(m) = h(u(m), m) \tag{2.42}$$

where m are model parameters like v_p, v_s, ρ in my study. u encloses the state variable. These state variables satisfy the state equations as

$$F(u(m), m) = 0 \tag{2.43}$$

F is the forward equation. I use the Born approximation to derive the linear relation between the data and the model. This will introduce a perturbation δm in the model and will induce a perturbation in the state variable δu and another one of the functional δE. So

$$F = (u + \delta u, m + \delta m) = 0 \tag{2.44}$$

. The first order will give

$$F = (u + \delta u, m + \delta m) = F(u, m) + \frac{\partial F(u, m)}{\partial \tilde{u}} \partial u + \frac{\partial F(u, m)}{\partial m} \partial m \tag{2.45}$$

Note that $\tilde{u}$ is a not physical realisation but only an element of the state variable. Replacing 2.43 in 2.45, I obtain:

$$\frac{\partial F(u, m)}{\partial \tilde{u}} \partial u = -\frac{\partial F(u, m)}{\partial m} \partial m \tag{2.46}$$

From equation 2.46,

$$\delta u = -\left(\frac{\partial F}{\partial u}\right)^{-1} \frac{\partial F(u, m)}{\partial m} \partial m \tag{2.47}$$

The first order development of E gives:

$$\delta E = \left\langle \frac{\partial h(u,m)}{\partial \tilde{u}}, \delta u \right\rangle + \frac{\partial h(u,m)}{\partial m} \partial m \tag{2.48}$$

$\langle\rangle$ denotes a scalar product. Inserting equation 2.47 in equation 2.48 rearranging I obtain

$$\delta E = \frac{\partial h(u,m)}{\partial m} \partial m - \left\langle \left(\left(\frac{\partial F(u,m)}{\partial \tilde{u}} \right)^{-1} \right)^{*} \frac{\partial h(u,m)}{\partial \tilde{u}}, \frac{\partial F(u,m)}{\partial m} \delta m \right\rangle \tag{2.49}$$

$*$ denotes the adjoint. Let us define λ

$$\left(\frac{\partial F(u,m)}{\partial \tilde{u}} \right)^{*} \lambda = \frac{\partial h(u,m)}{\partial \tilde{u}} \tag{2.50}$$

λ is the adjoint state variable and equation 2.50 is the adjoint state equation. The left side of this equation is the adjoint of the partial derivative the forward problem. If h is the L_2-norm, the right side of equation is the residuals between the modelled and the field data. The adjoint operator $*$ propagates backward the source term which is the data residuals in this case. Therefore equation 2.50 simply means that residuals are backpropagated in time. Replacing equation2.49 in equation 2.48 gives:

$$\delta E = \left(\frac{\partial h(u,m)}{\partial m} - \left\langle \lambda, \frac{\partial F}{\partial m} \right\rangle \right) \delta m \tag{2.51}$$

I rearrange the equation and obtain

$$\frac{\partial E}{\partial m} = \frac{\partial h(u,m)}{\partial m} - \left\langle \lambda, \frac{\partial F}{\partial m} \right\rangle \tag{2.52}$$

If L_2 is used as the misfit function, the first term of the right side of equation will be 0. This implies that

$$\frac{\partial E}{\partial m} = -\left\langle \lambda, \frac{\partial F}{\partial m} \right\rangle \tag{2.53}$$

Using equation 2.53 the gradient of the functional E is computed. Another method commonly used to compute the gradient of E is the Lagrangian. For more details about this other method, I refer the reader to Plessix (2006)

2.2.3 Other numerical methods during FWI

Step length estimation

The estimation of a step length α is very important in the FWI. A too large step length will result in huge jumps in the misfit function while a too small one will increase the computational costs. According to Wright and Nocedal (1999), an optimum step length is found using a parabolic fit. I compute the misfit E at different step length α for few selected sources. I plotted the misfit values against the step length. These are then fitted by a parabolic function. The step length α used to update the model is obtained when the parabolic function reaches its minimum.

Multiscale approach

The ideal FWI will find a strict global minimum to ensure a unique model to explain observed data Bunks et al. (1995). This is possible only if the starting model is as close as possible to the real one. However, this is not in most cases possible to know the properties of the test model because we don't have enough information about it. To ensure that the inversion converges, I use the multiscale approach. The idea is to find a local minimum that will be as close as possible close to the global minimum. In the multi-scale approach, many stages with different frequencies range are used. So I perform not only one FWI but many of them. At each stage, I filter my data and source with a Butterworth filter. The bandpass of the filter is then widened for the next stage, to add new high frequencies. The misfit function gets smoother and an optimum real model is reached.

Source time inversion

A known source signal function will improve FWI results, in that it will minimize the misfit function from the equation between observed data and modelled one. However, in most data acquisition like the ultrasonic case, the source signal is unknown. This issue is solved using the source time function (STF) by Pratt (1999). The source inversion is done in the frequency domain. I assume a synthetic source signature S_{syn} and the real one S_{real}. The aim is to find a scalar u which when multiplied by S_{real} in frequency domain will give us S_{real}. This is expressed as:

$$S_{real}(w_k) = s(w_k)S_{syn} \tag{2.54}$$

To achieve this, the misfit function has be to minimized. At each frequency the scalar s is derived through the deconvolution of modelled and observed data as

$$s_{w_k} = \frac{d_{obs}^T d_{syn}^*}{d_{obs}^T d_{syn}^* + \epsilon^2} \tag{2.55}$$

The parameter ϵ is called the water level and it helps to stabilize the deconvolution. In my study, I have multi-sources. Therefore I inverted each of them. Moreover, source inversion is done iteratively at each stage to ensure a good estimation of the source function and therefore good FWI results.

Chapter 3

Acquisition geometry

In this section, I will explain how the laboratory data used in this work were acquired. The geometry and the type of instruments used will be described in detail.

3.1 Model

The data used in this thesis were acquired at the Frauenhofer Institut for Non-Destructive Testing (IZPF) in Saarbrücken in December 2019.
A concrete block with a $5\,\mathrm{cm}$-diameter pipe in the middle served as test model (see Figure 3.1. Two sets of data were acquired using this model. For the first set, the pipe was filled up with air and for the second set, the pipe was filled up with water. The velocities values of P- and S- waves and density for the two configurations are presented in Table 3.1

Table 3.1: Velocity and density values of the concrete block. The velocities here are provided by the IZPF.

medium	v_p in $\mathrm{m/s}$	v_s in $\mathrm{m/s}$	ρ in $\mathrm{kg/m^3}$
concrete	4000	2500	2400
air	330	0	1.2
water	1500	0	1000

The concrete block is made up of screed, material that usually lays as a thin layer on top of concrete and contains small and sharp sand grains. The size of the grains varies between $0\,\mathrm{mm}$ and $4\,\mathrm{mm}$. Because of their small size, very low scattering is expected in the lab data. The black small lines marked on the concrete block (see Figure 3.1) represent the different source and receiver positions. These are located at the middle of the X-axis, $x = 40\,\mathrm{cm}$. The spacing between these points equals $3\,\mathrm{cm}$. The numbers highlighted are the first, middle and end positions of each side of the concrete block. These points help to identify the measure-

Figure 3.1: Concrete block with a pipe of $5\,\mathrm{cm}$ in the middle. Different measurement points are spotted as small black lines. They are equally spaced.

ment positions to easily model the concrete block.
When constructing the block, its size was intended to equal $80\,\mathrm{cm} \times 50\,\mathrm{cm} \times 38\,\mathrm{cm}$. However after desiccation, the length of the Z-axis actually varies between $36.5\,\mathrm{cm}$ and $38\,\mathrm{cm}$. The actual dimension of the block is shown on Figure 3.2.

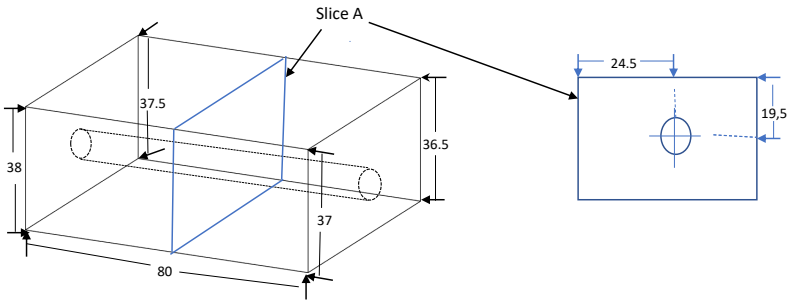

Figure 3.2: Left: 3D model of the concrete block with its actual dimensions. Right: Slice A is a 2D model of the concrete block. This was used as input model for in the synthetic forward modelling

3.2 Source and receiver characteristics

The acquisition system consists of one source, one receiver and one recording device.
The source and receiver are both ACS S1803 DPC transducers. These are transducers with

a nominal frequency of $100\,\mathrm{kHz}$ and a frequency bandwidth between $10\,\mathrm{kHz}$-$160\,\mathrm{kHz}$ (ACS Group). The transducers are shown in the Figure 3.3 below. The wear tip is the part of the transducer which is in direct contact with the test surface. The green material of the figure is the cover. This encloses all the parts of transducer.

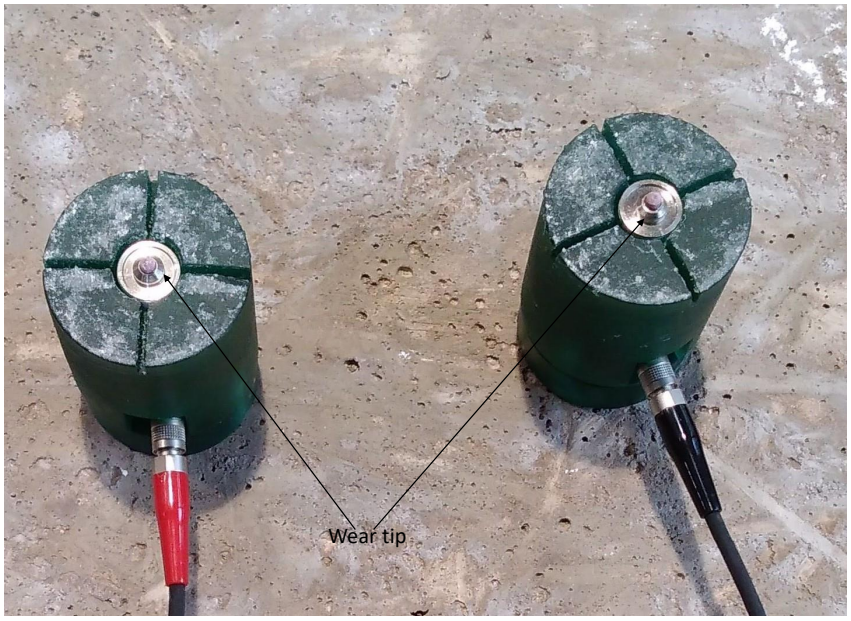

Figure 3.3: Dry point contact transducers. One acts as a source and the other as the receiver. They are connected to the flaw detector unit via cables.

DPC ("dry point contact") transducers allow testing concrete with either longitudinal or shear waves. Their characteristics are described by V. G. Shevaldykin et al. (2003), to which I refer the reader for more details. The DPC transducers used to acquire the data are longitudinal wave transducers. These have the particularity that the contact between them and the test surface is dry. Moreover, the size of the contact zone between them and the surface of the test object is many times smaller than the length of the ultrasonic wave (point contact). Taking, for example, our model, the P-waves will have a wavelength of about $\lambda = 40\,\mathrm{mm}$ in the concrete and the contact zone will be around $1.2\,\mathrm{mm}$. For all the above reasons, the signal emitted is assumed to be not influenced and transformed. Therefore the transducer is said, to act as a point oscillating force. This is very important mostly to derive the source signal. The directivity characteristic of the DPC is depicted in Figure 3.4. The image **a** describes the directivity of the DPC transducers used in this work. The DPC transducer with longitudinal oscillations can radiate and receive both P- and S-waves. The P-waves wavefront is strong in the area perpendicular to the half surface. On the other hand between $30°$ and $60°$ S-waves can be radiated or received.

The other device used during acquisition is the ACS A1220 MONOLITH 3D (ACS, 2018) shown in Figure 3.5. It has an electronic unit with a built-in battery. It is connected to the re-

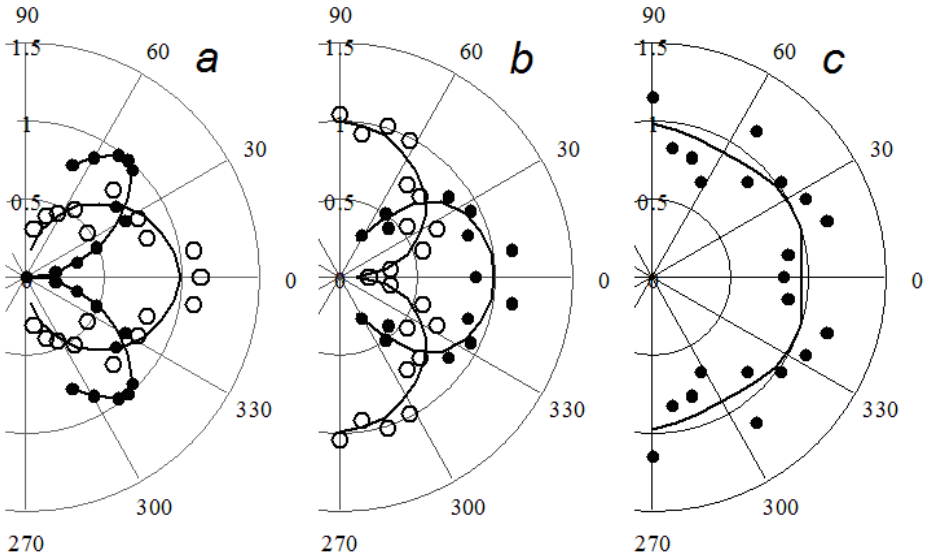

Figure 3.4: Directivity characteristic for Dry point with longitudinal oscillations **a** and shear oscillations **b** and **c**. The black points represent the • are the shear waves and ○ the longitudinal waves V. Shevaldykin et al. (2002).

ceiver/source transducer via cables. During acquisition, the electronic unit forms electronic pulses which activate the transducer then amplifies the signal received from the piezoelectric transducer. The signal is then processed and presented in a digital format. This factor is very important in the sense that one can evaluate directly if the recorded signal is good or not. Therefore one can repeat the process if not satisfied with the results. Moreover, the flaw detector helps to define the operating mode and different parameters like the operating frequency, the gain level, the pulse voltage and many others.

Figure 3.5: ACS A1220 MONOLITH 3D flaw detector unit.

3.3 Measurements

The slice A shown in Figure 3.2 is the model used for this study. This is a 2D model in the YZ plane. Along the Z-axis, there are 15 measurement points while along the Y-axis there are only 12. Since my acquisition setting is symmetric, I ended up with 54 measurement points $(2 \times 15 + 2 \times 12)$. However, each of these measurement point is not a source. Only a total of 24 shots are considered: 7 in the Y- direction and 6 in the Z- direction $(2 \times 7 + 2 \times 5)$. The distance between them is $9\,\mathrm{cm}$. The acquisition is not possible for adjacent points, due to the size of the transducer (see Figure 3.3).

Before recording a signal, some parameters are regularised on the ACS A1220 MONOLITH 3D handle unit. The input pulse has a constant voltage of $200\,\mathrm{V}$ and a repetition rate of $45\,\mathrm{Hz}$. A delay time of $5\,\mu\mathrm{s}$ is used, to ensure that the total actual signal was acquired. To increase the signal-to-noise ratio (SNR), each recorded signal is a result of 8 stacked traces. The sampling interval is $dt = 0.1\,\mu\mathrm{s}$ and the total recording time is $T = 4\,\mathrm{ms}$. Depending on the distance between the source and the receiver a gain level is used. This is one of the most important parameters. If the gain level is too big the amplitudes are clipped and information is lost. On the other hand, if the gain level is too small, the amplitude is too small and may not contain enough information about the test model. For this reason, 5 different levels are used $52\,\mathrm{dB}$, $58\,\mathrm{dB}$, $64\,\mathrm{dB}$, $70\,\mathrm{dB}$, $82\,\mathrm{dB}$. The gain level applied on the source depends on the distance between the source and the receiver. For small offsets, small gain level will be used to avoid amplitude clipping whereas for large offsets we will tend to use higher ones to avoid amplitude loss. There is a difference of $30\,\mathrm{dB}$ between the lowest and highest gain. So

after all the above parameters are defined on the control unit, the signal is recorded. Figure 3.6 shows how one signal is acquired. The whole data acquisition took more than ten hours.

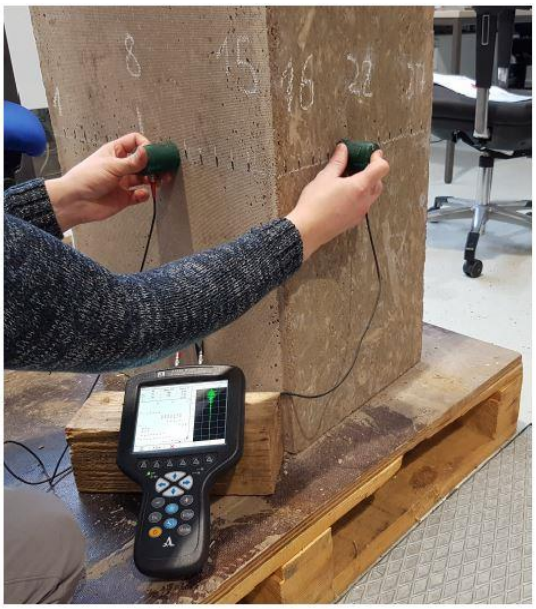

Figure 3.6: Acquisition process on the concrete block. The source and the receiver are positioned on the spotted points and the signal recorded viewed on the handle unit Müller (2020).

Chapter 4

Analysis of laboratory data

We acquired the lab data on a 3D concrete block. Two types of data were obtained during the acquisition: one with air inside the pipe and the other with water. Before making use of the data, I preprocess them. This chapter describes the different preprocessing tools that lead to obtaining the data. These will later be analysed for the identification of the different types of waves and their frequency content.

4.1 Preprocessing of the data

The laboratory data used in this work are given in two different binary formats: *.raw* and *.lbv*. Both of these formats are not recognized as potential input files by the FWI software I use. Moreover, each trace is saved as an individual file, whereas shots are used as input format in the code during inversion. This was taken into consideration when preprocessing the lab data. When acquiring the data, a time delay of $5\,\mu\mathrm{s}$ is introduced on the ultrasonic flaw detector ACS (2018) (see 3.3). The input sampling interval during acquisition was $0.1\,\mu\mathrm{s}$. So first after reading the different files, I remove the 50 first samples which corresponds to this time delay.
Secondly I compute a proper grid and time sampling according to equations 2.32 and 2.33 temporal) in chapter 2. The velocities of the different media present in my study are saved in Table 3.1. From this Table, $v_{min} = 330\,\mathrm{m/s}$. The instrument used as source, is supposed to produce a source signal with main frequency $f_c = 100\,\mathrm{kHz}$. Thus $f_{max} = 2f_c = 200\,\mathrm{kHz}$. In this work I perform the second order spatial inversion, thus equation 2.32 becomes

$$dh \leq \frac{330\,\mathrm{m/s}}{12 \times 200\,\mathrm{kHz}} = 1.3 \times 10^{-4}\,\mathrm{m} \tag{4.1}$$

Because the inversion will be a 2D one, the time sampling interval using equation 2.33 becomes as follows:

$$dt \leq \frac{1.3 \times 10^{-4}\,\mathrm{m}}{1 \times \sqrt{2} \times 4000\,\mathrm{m/s}} = 2.2 \times 10^{-8}\,\mathrm{s} \tag{4.2}$$

These will require huge computational needs. Müller (2020) to reduce the computational needs allowed grid dispersion in the air. Because pipe size is small compared to the whole model, its influence can be neglected. Following this, I have

$$dh \leq \frac{1500\,\mathrm{m/s}}{12 \times 200\,\mathrm{kHz}} = 6.2 \times 10^{-4}\,\mathrm{m} \tag{4.3}$$

Replacing dh in equation and computing the time sampling I have:

$$dt \leq \frac{6.2 \times 10^{-4}\,\mathrm{m}}{1 \times \sqrt{2} \times 4000\,\mathrm{m/s}} = 1.0 \times 10^{-7}\,\mathrm{s} \tag{4.4}$$

For consistency with Müller (2020), I define $dt = 7.0 \times 10^{-8}\,\mathrm{s}$. To approximate T, I assume that the longest distance travelled by the body waves is the diagonal distance $d = 0.6\,\mathrm{m}$. I can't consider the direct surface waves because they do not penetrate the model, hence provide no piece of information about the model. For both acquisitions, P-waves in water have the smallest velocity. So if P-waves travel along d, they will need $T = 4.0 \times 10^{-4}\,\mathrm{s}$. To be sure that to have more information about the model, I choose a longer recording time $T = 4.9 \times 10^{-4}\,\mathrm{s}$. So each of my traces will have 7000 samples. Using this new parameter, I resample my data using linear interpolation. Then I normalize each trace to its maximum. I couldn't consider absolute values because different gain levels are used when acquiring the data. So there is a difference in energy between the signals. Considering absolute amplitude will tend to make the amplitude of signal acquired with low gain level. After normalization, the traces are saved as shots. To save the traces as shots, I use the order: top, bottom, left and right. Receivers 1 to 15 located are at the top of the model, followed by receivers 16 to 30 located at the bottom of the model. The receivers 31 to 42 are located to the left of the model, and receivers 43 to 54 located at the right of the model. I save all my data in this series.

4.2 Data quality check

After preprocessing my data, I save them in a gathered format. In this section, I analyze the given data. I identify the different types of waves and investigate the frequency content of the data. For consistency, I check one shot located at the edge of the model shot 0 with component v_y and another one located in the middle of the right side shot 21 with component

v_x.

4.2.1 Water-filled pipe data

Shot 21 is shown in figure 4.1 below. This shot is located at $y = 50\,\mathrm{cm}$ and $z = 20\,\mathrm{cm}$. That is in the middle-right of my model. Looking at this shot, I note the high signal-to-noise ratio (SNR). Going over other shots, I notice that almost all shots had good SNR except shot 19. This source located on the right side of the concrete, had one bad trace. The shot is shown in the appendix B. For further investigations, I cancel the bad trace. On receivers 1 to 30, located at the upper and lower surface of the model, I cannot assign with precision the types of waves. These waves are radiated at angles between $22°$ and $76°$. This corresponds according to 3.4, to pattern in which we might have both longitudinal and shear waves. The waves on these receivers have very low amplitude and average length of $0.5\,\mu s$. I cannot really explain or identify the waves types that arrive later on those receivers. The coda is quite complex. Some of the waves with high amplitude might correspond to surface waves, whereas other low ones cannot be adequately identified. This might explain the low amplitude of the first arrivals since each trace is normalized to its maximum. I identify clearly the P-waves onsets on receivers 31 to 43, as they travelled perpendicular to the surface of the half-spaced. They have higher amplitudes compared to the first arrivals waves on lower receivers. On receivers 43 to 51 located on the same side as the source, Rayleigh waves are dominant. They have a very high amplitude to that of the P-waves identified on other receivers.
Shot 0 is depicted on figure 4.2. This shot is located at the edge of the 3D concrete block, exactly at the top left. The SNR is as good as for shot 0. On some receivers like 20 to 27 and 48 to 50, I have some noise before the P-waves onsets. This may be due to the acquisition environment. As we were in a basement and workers were moving in and out during acquisition. On receivers 1 to 13 located at the top of the model, Rayleigh waves are dominant. These have very high amplitudes. On receivers 14 to 28 located directly opposite to the source, I identify the P-waves onsets. These P-waves have a high amplitude compare to the one on receivers 29 to 51. At late arrivals, I cannot also identify the coda. Rayleigh waves are also dominant on receivers, which are located at the left side of the model. Still, on this site, I see that the further the receiver is located, the clearer the P-onsets become. For receivers 41 to 50, I can also identify the P-waves arrivals. They are radiated between $2°$ for the nearest receiver and $36°$ for the furthest one. This corresponds approximately to longitudinal waves according to Figure 3.4. Around $0.2\,\mu s$, I also identify some coherent data. These waves are the scattered P-waves. As the Rayleigh waves travel along the upper surface of the concrete block, they are scattered and converted to P-waves when in contact with the top left corner point. This is why they have higher amplitude as they are derived from the Rayleigh waves, which are known for their high amplitude. Looking over the

gathers, I notice that these waves are present on all gathers located at the edge of my model except shots 14 and 19. This my be due to a bad source/receiver coupling for the mentioned shots.

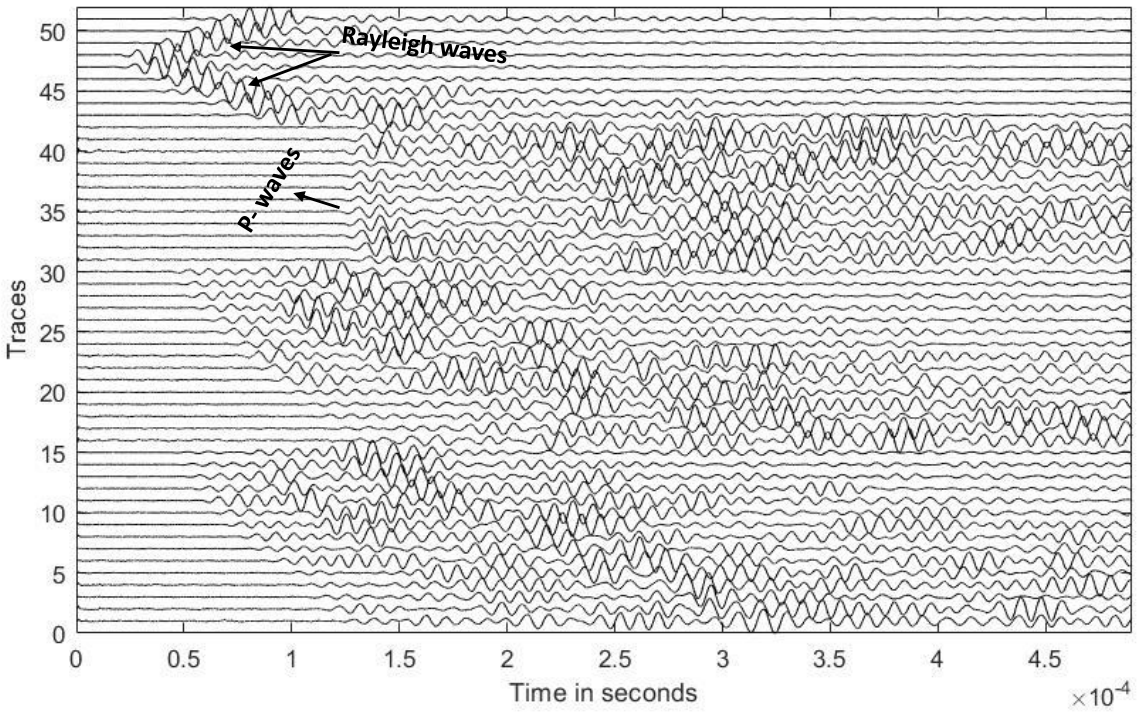

Figure 4.1: Shot 21 located at $y = 50\,\mathrm{cm}$ and $z = 20\,\mathrm{cm}$. The traces are acquired on the 3D beton block and normalised. The pipe is filled up with water. The different waves types are marked.

Frequency content

After analyzing the field data, I check their frequency content. To do this, I applied a simple Fourier transformation to the data. The average amplitude spectrum of all 24 shots in the window from $0\,\mathrm{kHz}$ to $800\,\mathrm{kHz}$is shown in Figure 4.3a. The amplitudes are normalized to the global maximum. For better visualization, I reduce the frequency window between $0\,\mathrm{kHz}$ and $170\,\mathrm{kHz}$. This is shown in Figure 4.3b. The peak frequency is around $114\,\mathrm{Hz}$. From $0\,\mathrm{Hz}$ to $2\,\mathrm{kHz}$ the amplitude increases from 0 to about 0.1. But from $2\,\mathrm{Hz}$ to around $53\,\mathrm{Hz}$, I observe a decrease amplitude value. This means that in this frequency range, there is little information about my data. The main information in my data is between $60\,\mathrm{kHz}$ and around $140\,\mathrm{kHz}$. In this range, I have lots of minima, of which the lowest is at $105\,\mathrm{kHz}$. The frequency content of my data differs from what I expected. The main frequency of the transducer is $100\,\mathrm{kHz}$ and the bandwidth of $40\,\mathrm{kHz}$-$160\,\mathrm{kHz}$. This differs from the observation. This might be due to the source/receiver coupling as it depends on the person holding them. Another reason can also be the noise present in the data.

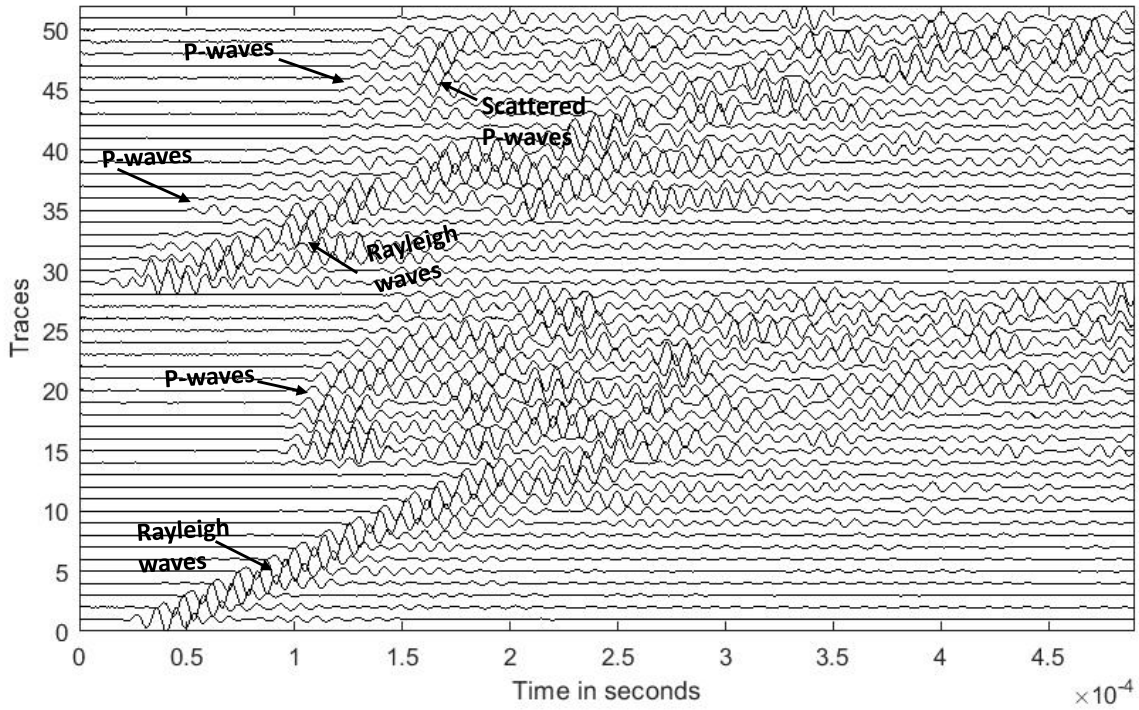

Figure 4.2: Shot 0 located at $y = 3.5\,\mathrm{cm}$. The traces are acquired on the 3D concrete block and normalised. The pipe is filled up with water. The different waves types are marked.

4.2.2 Air-filled pipe data

As I did for the water data, I also analyze the air data shots. Shot 21 is shown in Figure 4.4. As for shot 0, for the water-filled pipe data, I cannot assign the first waves on the receivers 1 to 30 located at the top and bottom of my model. I notice that they have also very low amplitude. On receivers 31 to 42, the amplitude of the P-waves is higher compare to that of other receivers. However, on all the receivers I cited, it is difficult for me to explain the coda at late arrivals. At late arrivals, I have Rayleigh waves and other types of waves that I cannot identify. The Rayleigh waves are mostly dominant on receivers 43 to 51, and have very high amplitude.

The gather 0 is shown in Figure 4.5. Rayleigh waves are dominant on receivers 1 to 13 located at the top of the model as the source. On receivers 14 to 28, I identify the P-waves onsets. They have a high amplitude. On receivers 29 to 40 the surface waves dominate and have higher amplitude. The P-waves onsets can also be identified on the receivers 41 to 51. At around $17\,\mathrm{ms}$, I also observe the scattered. These are scattered P-waves. They have higher amplitude compared to the amplitude of P-waves of other receivers. They also have same origin as for the water-filled data.

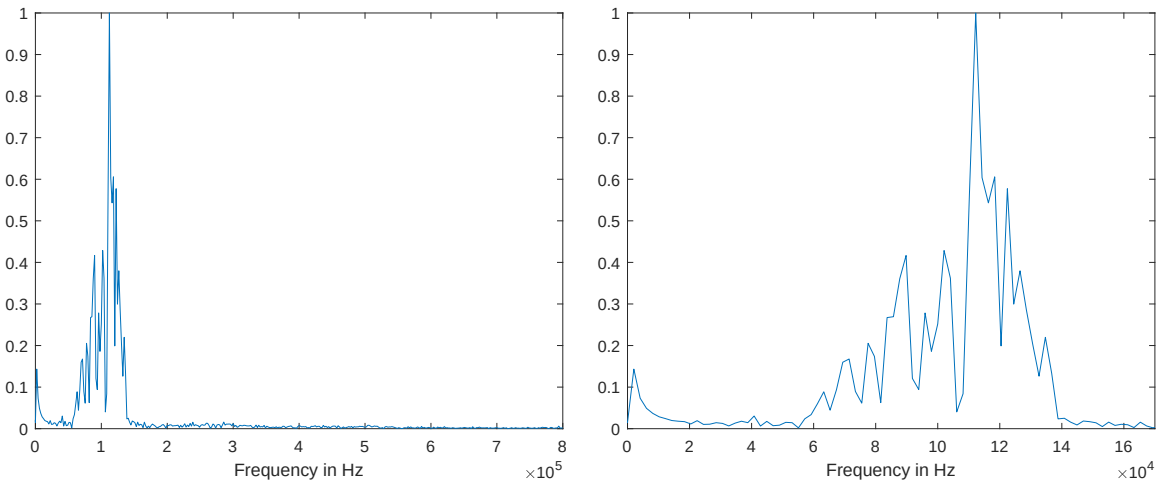

(a) Frequency window from 0-800 kHz **(b)** Frequency window from 0-170 kHz

Figure 4.3: Average frequency spectrum of all 24 water-shots.

Frequency content

The average amplitude spectrum of all the 24 shots is shown is in Figure 4.6. Between 0 kHz to 2 kHz, the amplitude increases to a value of 0.4. After this frequency until around 60 kHz, the amplitude decreases. Till 60 kHz, there is little information present in the data. I also observe a lot of local minima. The bandwidth of data is 60 kHz-140 kHz and the peak frequency is around 110 kHz. This is totally different from the properties of the transducers I used. This might also be due to the noise present in the data or the source/receiver coupling.

4.2.3 Summary

I browse over all my shots for both data sets. Gathers located at edges of my model have the same structure like a shot 0 in both data sets, while shots located in the middle of the side of the model look like shot 21. Rayleigh waves are dominant on all shots and have high amplitude. P-waves have high amplitude on receivers located directly opposite the source. On these receivers, after the P-waves, I identify the scattered P-waves. On receivers located near the source, Rayleigh waves dominate and have very high amplitude. This observation is made on all shots independently of the medium in the pipe. It is difficult to assign late arrivals coda for each data set.
The frequency content of my data differs from what I expected, according to the transducer's characteristics.

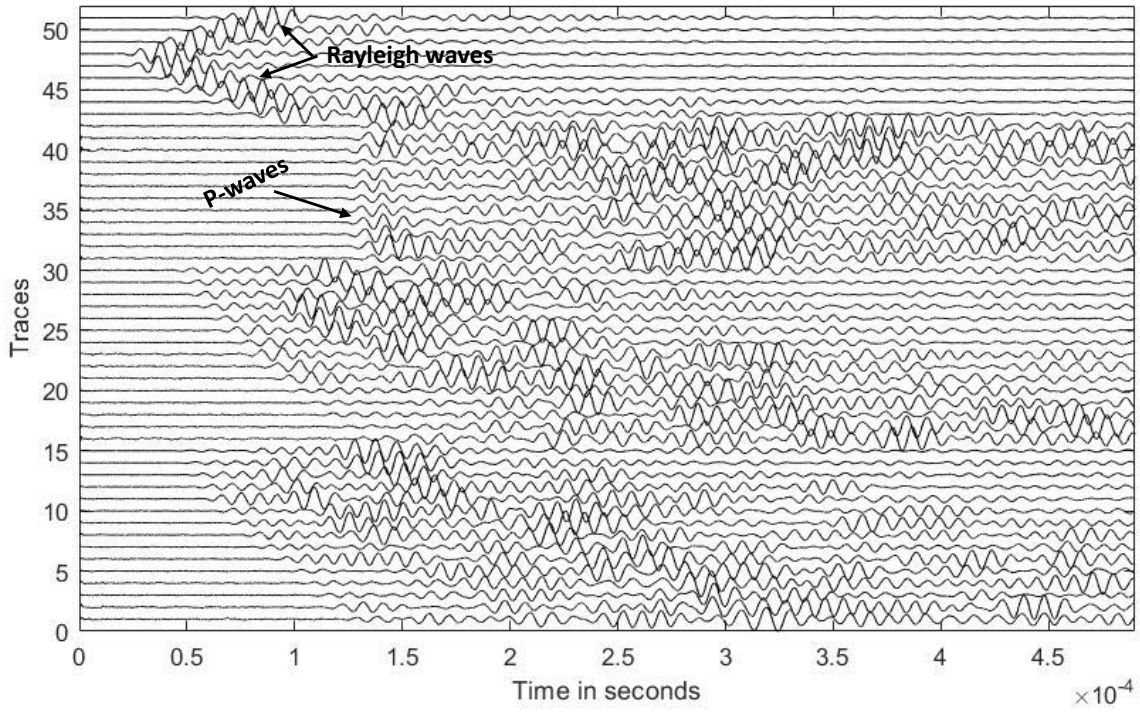

Figure 4.4: Shot 21 located at $y = 50\,\mathrm{cm}$ and $z = 20\,\mathrm{cm}$. The traces are acquired on the 3D beton block and normalised. The pipe is filled up with air.

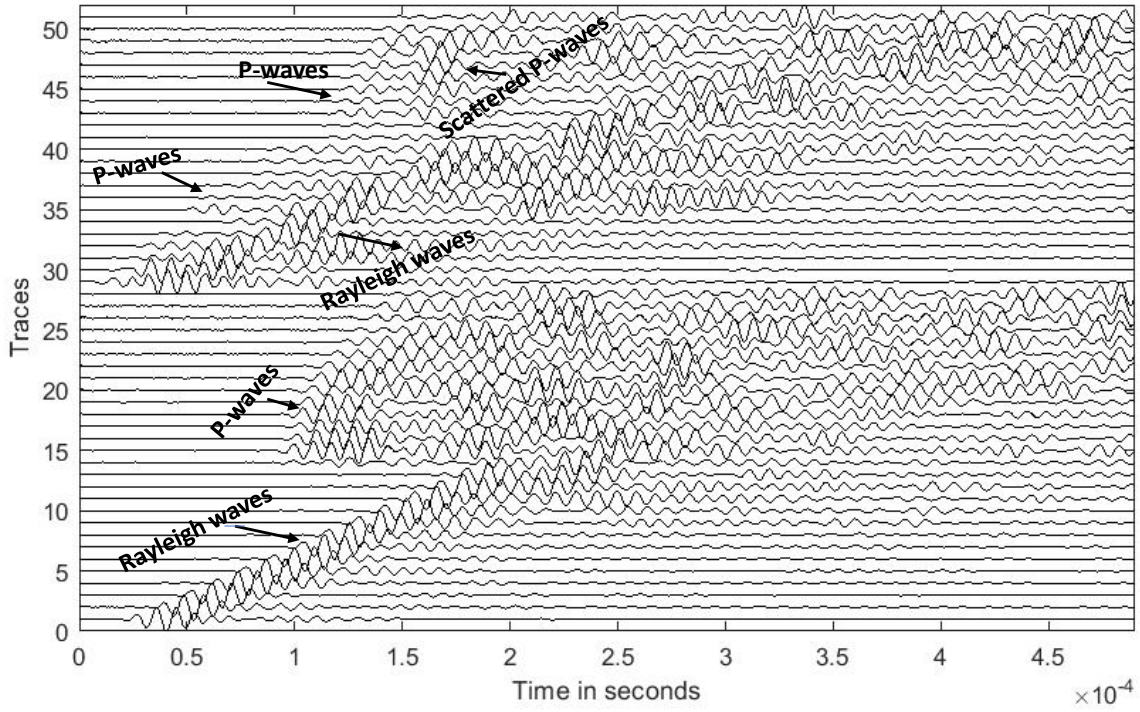

Figure 4.5: Shot 0 located at $y = 3.5\,\mathrm{cm}$. The traces are acquired on the 3D concrete block and normalised. The pipe is filled up with air.

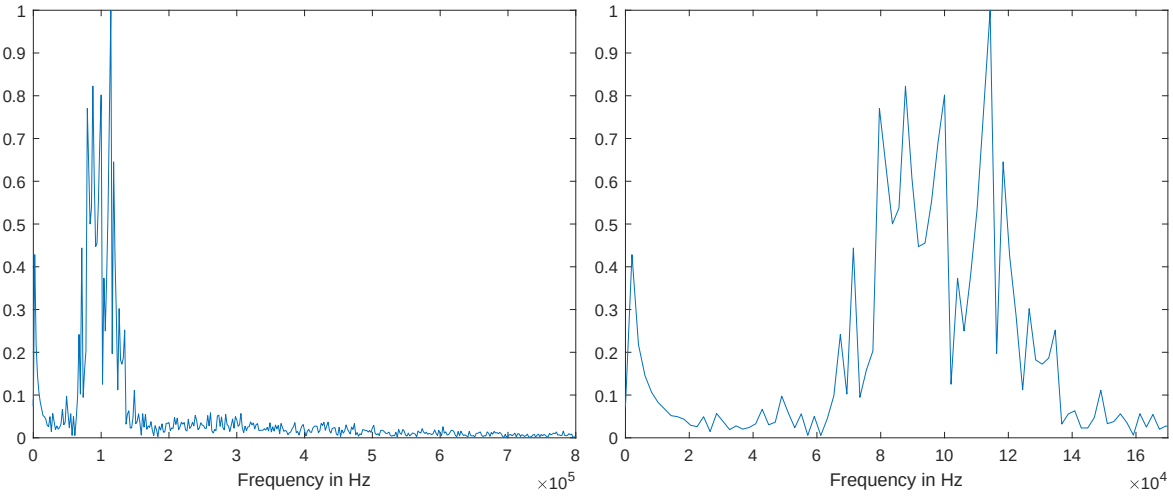

(a) Frequency window from 0-800 kHz

(b) Frequency window from 0-170 kHz

Figure 4.6: Average frequency spectrum of all 24 air-shots.

Chapter 5

Forward Modelling

In chapter 3, I describe my model and the acquisition system used for this work. Following this, I proceed with a synthetic reconstruction. This synthetic test aims not only to model seismograms that will look similar to the lab data but also to understand the wavefield. Indeed, the wavefield will not explain the 3D lab data, but it will help to overview the wave propagation. In this chapter, I will numerically model the 2D slice (Figure3.2) of the concrete block using a given source function. Using them, I perform the forward simulation using the finite-difference method explained in chapter 2. The seismograms generated by the modelling will, later on, be used for the inversion.

5.1 Model reconstruction

To perform the forward modelling, I first design the 2D model numerically along the YZ plane using MATLAB. As shown in Figure 3.2, I assume that slice A, corresponding to the 2D model, is taken exactly where the measurement points are located. Therefore the dimensions of the 2D concrete block are $y = 50\,\mathrm{cm}$ and $z = 37.5\,\mathrm{cm}$. I already define the time, grid sampling and total simulation time in 4.1. I use the same values during the synthetic test to ensure consistency with the lab data. To simulate a free surface boundary condition, I implemented a vacuum with 10 grid points surrounding the model. In the vacuum, v_p v_s and ρ are zero. Considering this, I ended up with a model of size 827×625 grid points. Since I have two datasets, air-filled and water-filled, I build two different models. I use the same values for v_p, v_s and ρ presented in Table 3.1.

As far as the acquisition system is concerned, the same configuration as described in 3.3 is used. This means I have 54 measurement positions with 24 sources symmetrically distributed: 7 along the Y-axis and 5 along the Z-axis. The space between each point is $3\,\mathrm{cm}$. Since I remove the bad traces during the preprocessing of the data, I also remove the corresponding receiver in my synthetic modelling. This ensures that I have the same geometry

acquisition for each source as in the real data. Figure 5.1 shows an example of the model and geometry configuration for shot 0 when the pipe is filled with water. This model represents v_p. If I consider v_s or ρ, the background model will look the same, but the values of density/velocity will be different on the pipe according to Table 3.1.

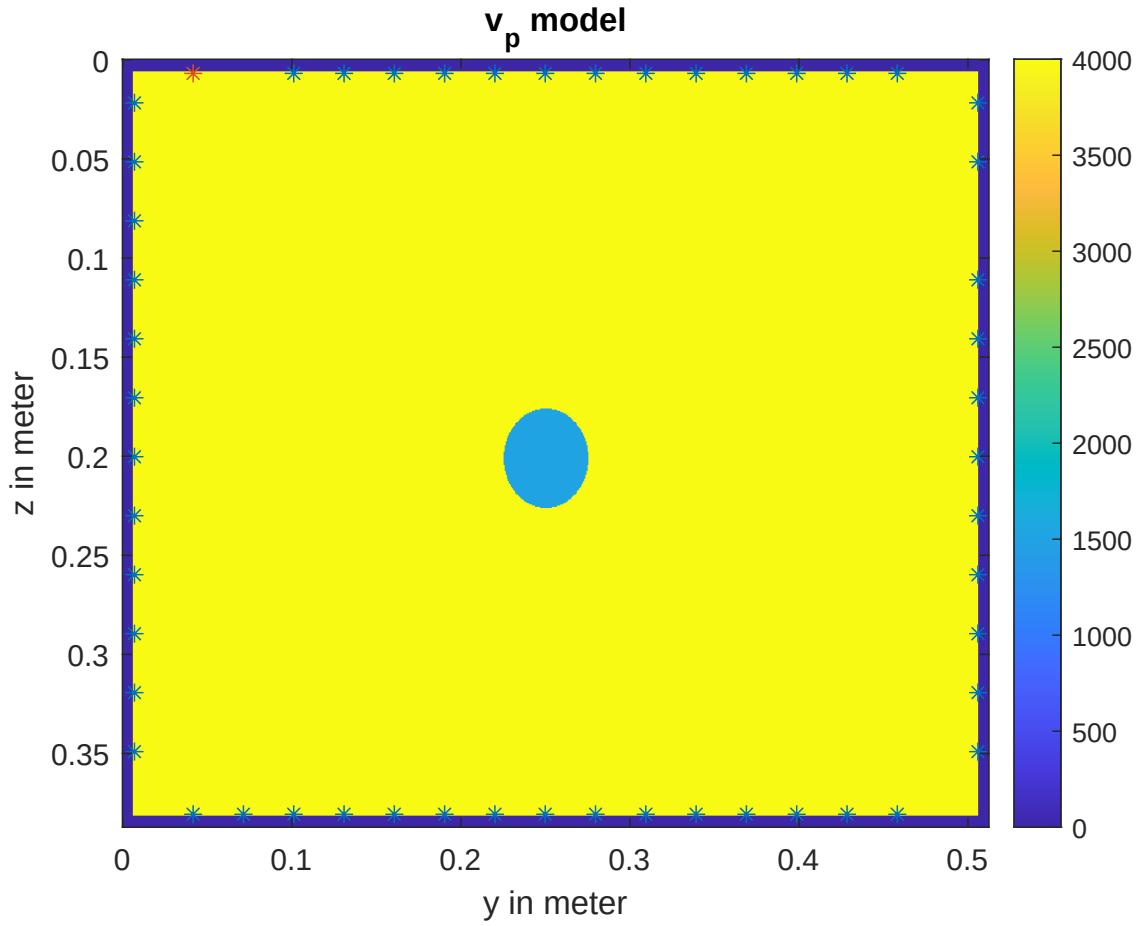

Figure 5.1: v_p velocity model with the pipe filled with water with the acquisition system for shot 0. The point spotted in red is the source while the ones in blue are the receivers.

5.2 Source time function

To properly reconstruct the wavefield, the source signal is significant. The source signal used for the NDT at IZFP was not given. In his work, for synthetic modelling Müller (2020) used a Ricker wavelet. However Seidl (2018) when applying FWI to NDT, stated that most source signals from transducer are Hann-Windowed tone bursts. He even mentioned the influence the number of cycles might have on the inversion results in his work. Following this, I look for a number of cycles of a Hann-windowed tone burst, which could describe my lab data. I finally choose a three cycles tone burst. This source signal has a s a nominal frequency of $100\,\mathrm{kHz}$ as the ACS S1803 DPC transducer used to acquire the data. I use the

same time sampling to sample the lab data so that the CFL criterion will be satisfied. Hence $dt = 7.0 \times 10^{-8}\,\mathrm{s}$ and $T = 4.9 \times 10^{-4}\,\mathrm{s}$. The source time function will have 7000 samples. The source signal and its corresponding spectrum are shown in Figure 7.5. Both the source wavelet and amplitude spectrum are normalized.

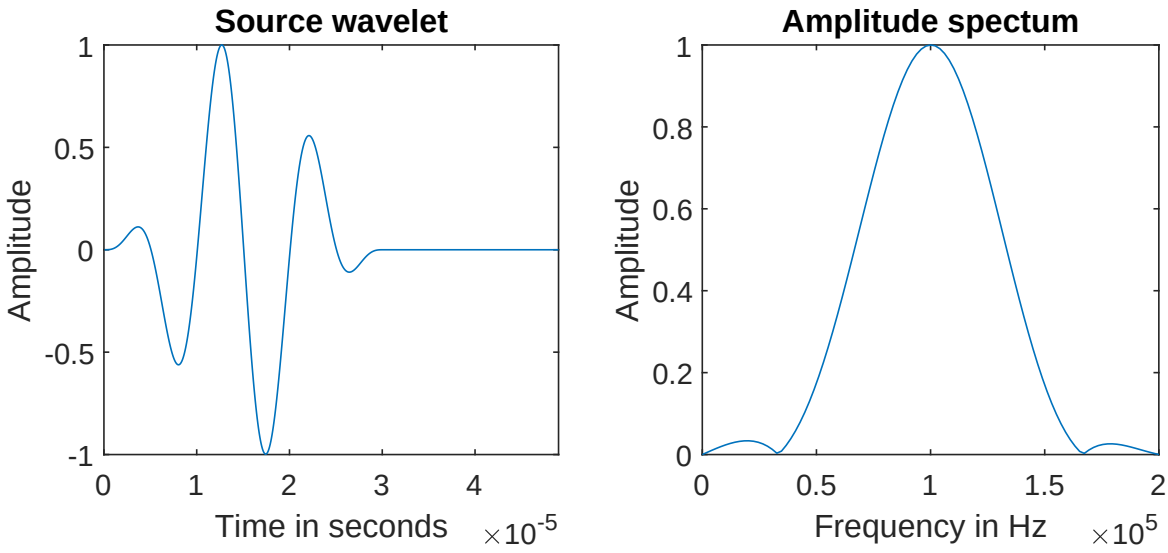

Figure 5.2: Left: the 3-cycles Hann-windowed tone burst with a center frequency $f_c = 100\,\mathrm{kHz}$. Right: The ampltiude spectrum of the source time function with bandwidth $0\,\mathrm{kHz}$-$160\,\mathrm{kHz}$

5.3 Results of the forward modelling

After defining my parameters, I perform forward modelling for both water and air datasets. This section presents the wavefield for water-filled pipe data and exmaples of seismograms.

Water-filled simulation: wavefield and seismograms

I execute the simulation of the data with the water-filled pipe. I analyse the wavefield for two different shots: shot 0 and shot 21.

Figure 5.3 shows the wavefield evolution for shot 0. The snapshots represent the v_y component of the wavefield. The amplitudes are clipped ton enhance visualization. At $T = 5.6 \times 10^{-5}\,\mathrm{s}$ I identify the direct P-wave front. The Rayleigh waves propagate along the upper surface of the model. As they reach the upper left corner of the model, they are scattered. This is because corner points act as diffraction points. The surface waves are then converted to P-waves. These scattered P-waves have higher amplitude as the P-waves $T = 8.4 \times 10^{-5}\,\mathrm{s}$. When $T = 1 \times 10^{-4}\,\mathrm{s}$, the pipe filled up with water is illuminated, both the direct P-waves and the scattered waves penetrate the pipe. S-waves do not penetrate the pipe as the pipe is filled up with water. Instead, part of their energy is reflected at the

boundary while the other travel round the pipe. The P-waves in water have a smaller velocity than in the concrete. So they will be slowed down, and the signal will mostly reflected at the concrete-water boundary. Part of the signal however penetrates the pipe. In water, the waves are dispersive. The lower corner of the model also acts as diffraction points. On the last snapshot $T = 15 \times 10^{-4}\,\mathrm{s}$, there are different type of waves, multiple reflected waves from boundaries, scattered waves from edges and those reflected from the pipe. I decide not to show snapshots for further time as they become more complex and will not bring new information.

The shot gather corresponding to this wavefield propagation is depicted in Figure 5.4. One can first notice that the Rayleigh waves have very high amplitudes compared to those of the P-waves. On receivers 1 to 13 located at the upper surface of my model, the Rayleigh waves are dominant. Reflected waves follow them. On receivers 14 to 28, I identify the P-waves. On these receivers, the P-waves have the highest amplitudes. They are followed by reflected waves with almost similar amplitudes and surface waves with higher amplitude. On the receiver 29 to 40 located on the left side of the model, I also have P-waves onsets. The larger the offset on this side, the more difficult it becomes to identify the P-waves onsets to be identified. The surface waves are also dominant, and I have reflected waves. The P-waves still have small amplitudes for the receivers 41 to 51 while the surface waves has higher amplitudes. Around $T = 1.5 \times 10^{-5}\,\mathrm{s}$ I have the scattered P-waves. They have higher amplitude than the P-waves, although the difference isn't that much as for the lab data 4.2. At late arrivals, I have many reflections coming either from the boundaries of the model or the pipe and scattered waves.

The other wavefield I studied, is that of shot 21, located in the middle of the right side of my model. The snapshots of the wavefield of shot 21 are shown in Figure 5.5. On the first snapshot $T = 5.6 \times 10^{-5}\,\mathrm{s}$, one can identify the P-wave wavefront. The S-wave wavefront also starts to form. This is well depicted on the second snapshot $T = 8.4 \times 10^{-5}\,\mathrm{s}$. The Rayleigh waves, which have already reached the boundaries of the model, are reflected. At $T = 1.0 \times 10^{-4}\,\mathrm{s}$, the waves have already penetrated the pipe. Part of them are reflected while the other move through the pipe. On the last snapshot $T = 1.5 \times 10^{-4}\,\mathrm{s}$, many waves are superimposed. As for shot 0, I didn't show the further snapshots since the wavefield becomes more chaotic.

The seismograms of shot 21 are shown in Figure 5.6. The Rayleigh waves are also dominant. They have very high amplitudes compare to those of other waves present. From receivers 1 to 30, located at the upper and lower surface of the model respectively, the P-waves onsets can be identified. Their amplitude is very low. They are followed by the S-waves, which have higher amplitude. These do not penetrate the pipe since it is filled up with water. The surface waves are dominant on these receivers. At late arrivals, we have multiple reflections. On receiver 31 to 42, the P waves have the highest amplitude. Multiple reflections also follow

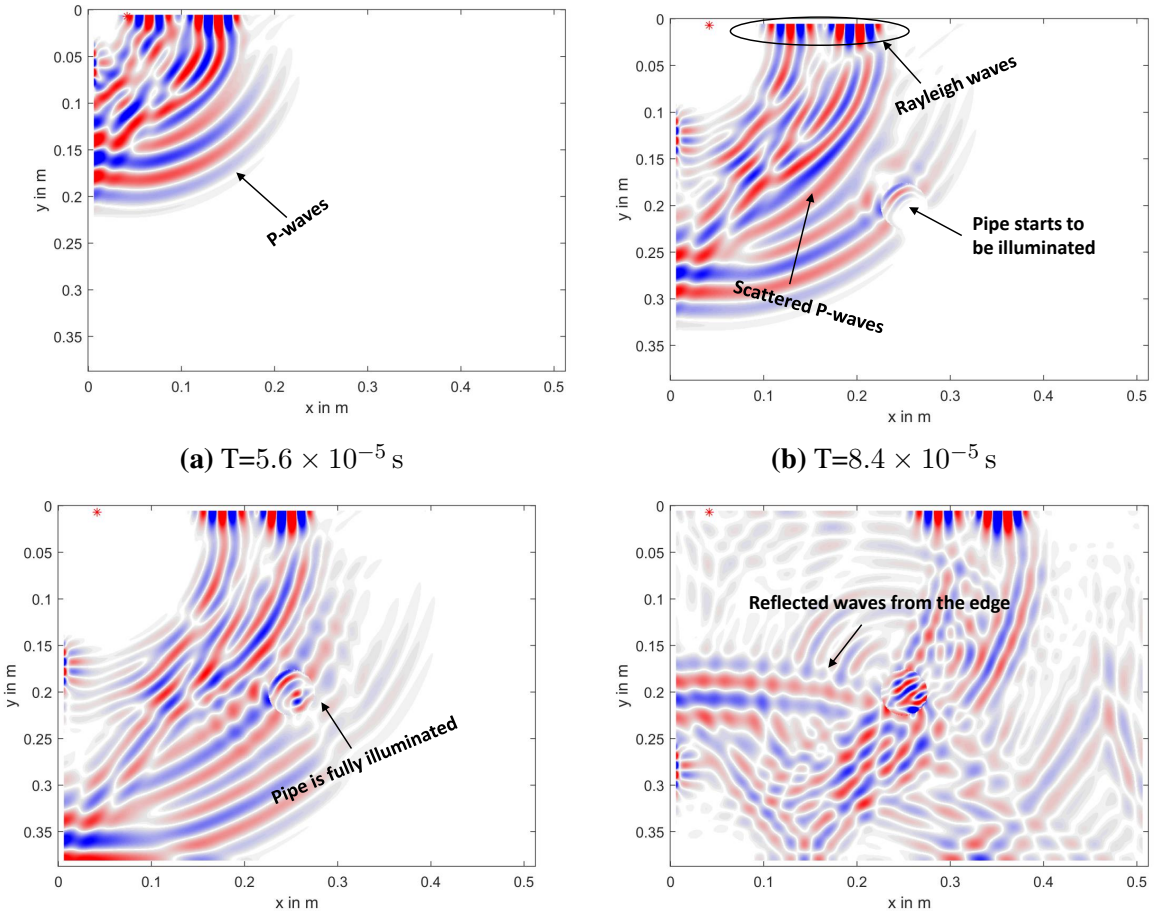

(a) T=5.6×10^{-5} s **(b)** T=8.4×10^{-5} s

(c) T=1.0×10^{-4} s **(d)** T=1.5×10^{-4} s

Figure 5.3: Snapshots of the v_y component of shot 0. The source is spotted in red. The pipe is filled with water.

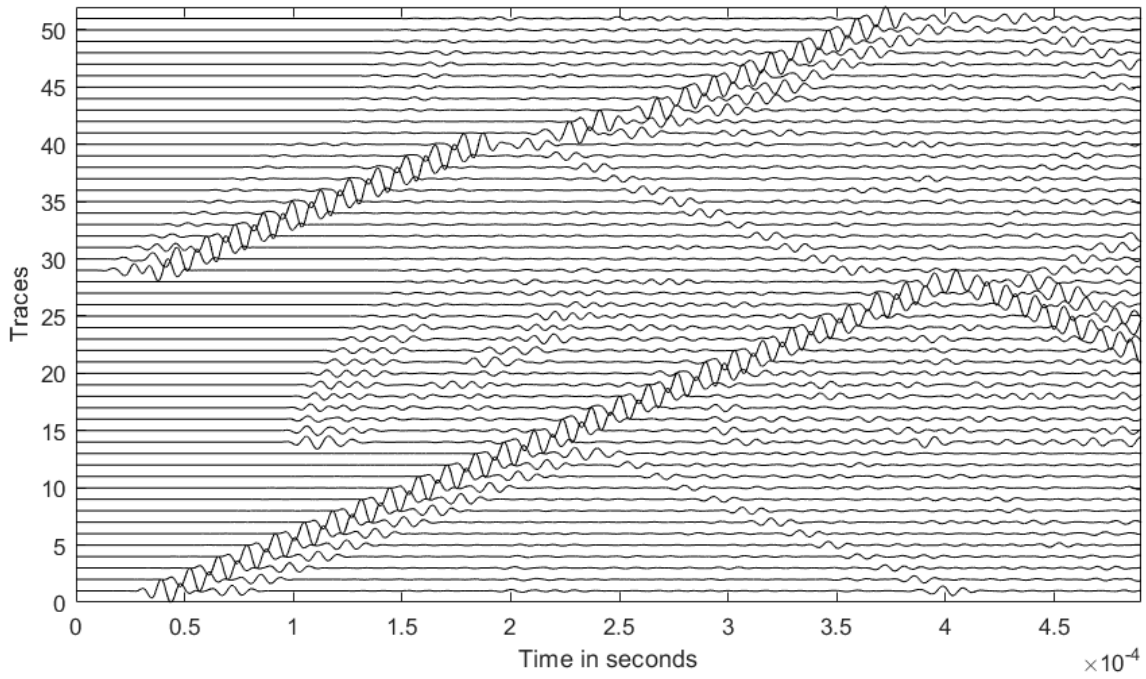

Figure 5.4: Seismograms of shot 0. The traces are normalised. The pipe is filled up water.

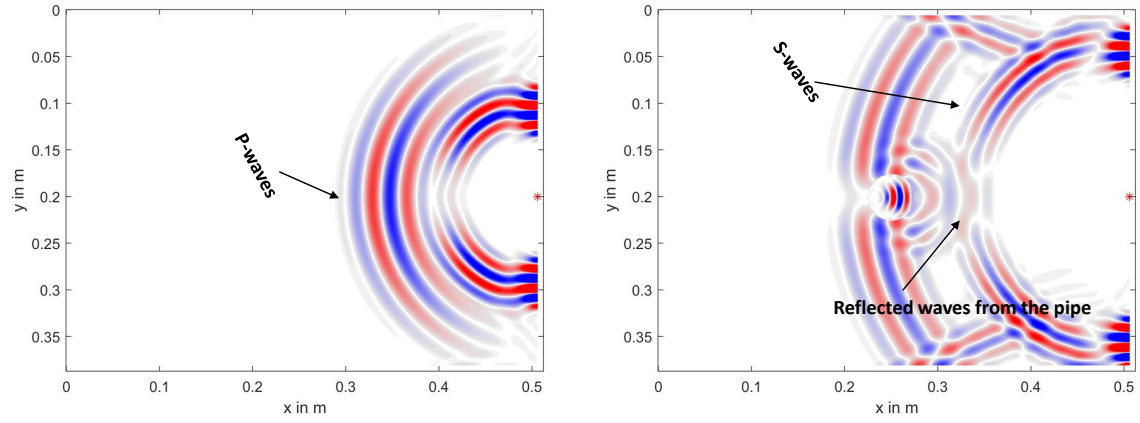

(a) T=5.6×10^{-5} s **(b)** T=8.4×10^{-5} s

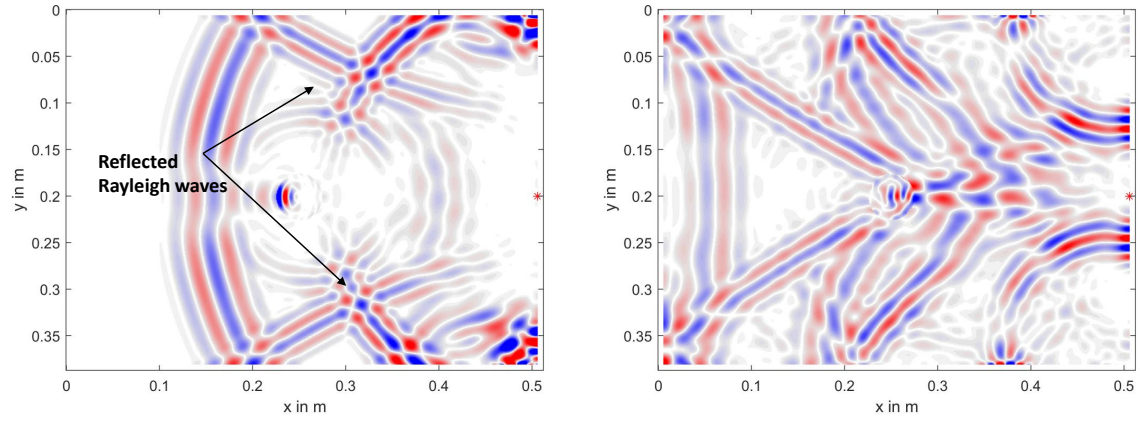

(c) T=1.0×10^{-4} s **(d)** T=1.5×10^{-4} s

Figure 5.5: Snapshots of the v_x component of shot 21. The source is spotted in red. The pipe is filled with water.

them. On the receivers 43 to 51, the Rayleigh waves are also dominant with high amplitude. I also model the data when the pipe is filled with air. In air the values of v_p, v_s, ρ are smaller. The background model remains the same. So I expect the same general structure of the wavefield and the gathers. There is no difference between with the water-filled data. For this reason, I didn't show them here.

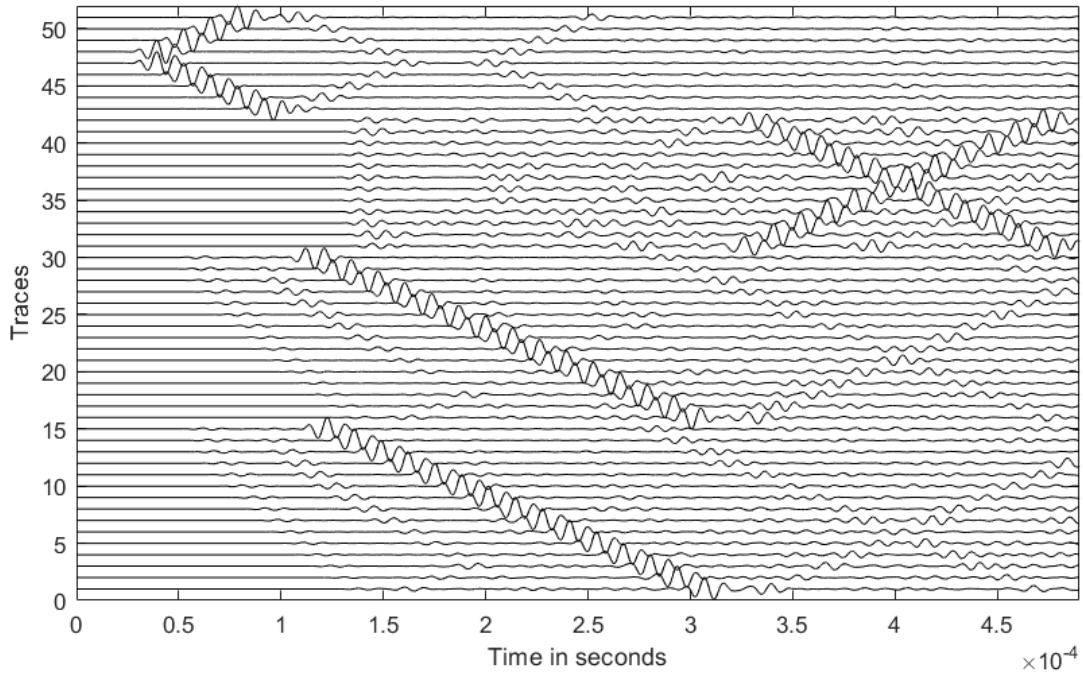

Figure 5.6: Seismograms of shot 21. The traces are normalised. The pipe is filled up water.

Chapter 6

Inversion of synthetic data

To evaluate the potential for the applicability of FWI on lab data, I carry out different inversion tests. The seismograms used for inversion are the ones I numerically modelled in chapter 5. First I use the full data information content and second only transmitted ones to invert v_p, v_s, ρ simultaneously. The results of both inversions lead me to discuss the challenges of FWI for the concrete model.

6.1 Full data information inversion

6.1.1 General inversion settings

In this section, I perform the FWI using the full data content for both data sets. Figure 2.2 shows the algorithm of FWI. In this synthetic FWI reconstruction, observed data are the numerically modelled seismograms from chapter 5. Since the pipe in the model is actually the body to reconstruct, the initial model is a homogeneous one (see Figure 6.1. The source time function is still the three cycles Hann-windowed tone burst, so I didn't invert for the source function. As a misfit function, I use, the L_2-norm and to optimize the inversion, I apply the conjugate gradient and step length method (chapter 2). According to my data's source signal spectrum, I invert the data between $40\,\mathrm{kHz}$ and $160\,\mathrm{kHz}$. To avoid cycles skipping, I use the multiscale approach, and the different stages for both data sets are presented in Table 6.1. The relative misfit is the abort criterion. For the air-filled data, the relative misfit is constant, whereas for water-filled data, I use a higher abort criterion for high frequencies. This will stabilise the inversion. A 12^{th} order Butterworth filter is applied to the data to filter them. The maximum iterations per stage are 30.

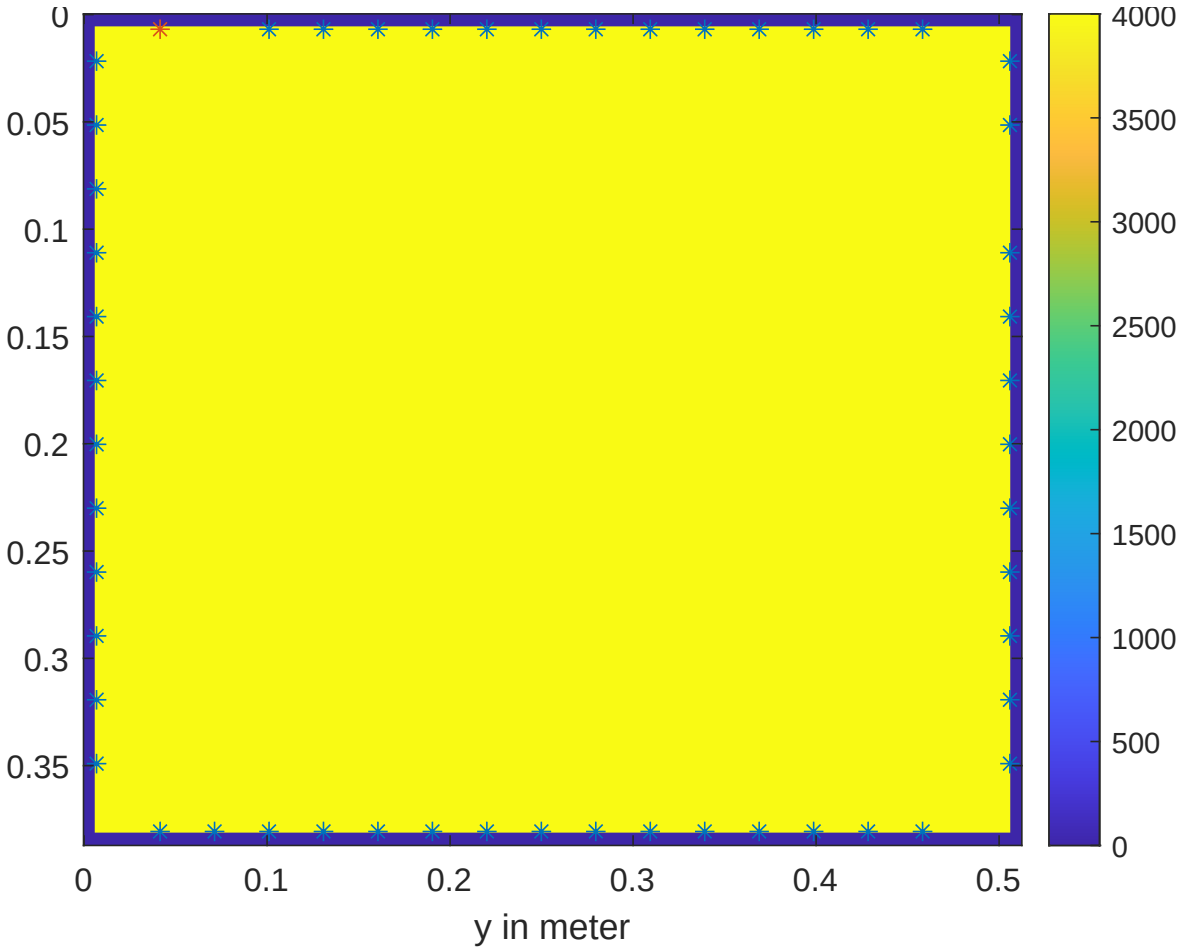

Figure 6.1: Initial model used for the FWI for both water-filled and air-filled datasets.

6.1.2 Inversion results

Water-filled pipe data

After defining all the inputs parameters, I invert v_p, v_s, and ρ simultaneously. The inversion stopped after 114 iterations. Figure 6.2 shows the final models for all the model parameters. On the first row, I plot the true and inverted v_p. We can see the shape and boundaries of the pipe. The boundaries are smooth and continuous. For v_s (see Figure 6.2d), the boundaries of the pipe are not continuous as it breaks. We can also observe small zones of the pipe where we have velocity information which lies between $1000\,\mathrm{m/s}$ and $1500\,\mathrm{m/s}$. These values are actually higher than the true v_s. The final model of ρ is shown in Figure 6.2f. The shape and position of the water inclusion are well reconstructed. Unlike the two models, ρ contains more information about the true density value of the model. This value is not true though as it $\approx 1500\,\mathrm{kg/m^3}$ and is actually higher than true ρ.

The normalized misfit is depicted in Figure 6.3. The misfit jumps to a higher value each time the inversion goes to another stage as higher frequency are considered. The misfit decreases from 1 to around 0.45. To evaluate the inversion, I compare the pseudo-observed data and the modelled data of shot 0. This is depicted in Figure 6.4. The results of the inversion weren't

Table 6.1: Workflow with different stages used to invert the full waves content.

Medium	Lower frequency corner in kHz	upper frequency corner in kHz	Relative misfit
Water	40	50	0.005
	40	60	0.005
	40	70	0.005
	40	80	0.005
	40	90	0.005
	40	100	0.005
	40	120	0.01
	40	140	0.01
	40	160	0.01
Air	40	60	0.005
	40	70	0.005
	40	80	0.005
	40	90	0.005
	40	100	0.005
	40	120	0.005
	40	140	0.005
	40	160	0.005

good but on the contrary the pseudo-observed and modelled data match well especially the surface waves.

Air-filled pipe data

The inversion stopped after 160 iterations. The final models of the inverted parameters are shown in Figure 6.5. The reconstruction doesn't work well for all the model parameters as they don't reach the true v_p, v_s or ρ values. This might be because ultrasonic waves are known to be highly attenuated in air. However for all the parameters, the exact shape and position of the pipe are well reconstructed. In Figure 6.5d, we can see small regions with velocity on the left side of the inverted v_s model. The inverted density ρ is the only final model which shows more information. The updated ρ is far from the real one and is instead higher ($\approx 1000\,\mathrm{kg/m^3}$) than the true density.

The normalized misfit function is shown in Figure 6.6. The misfit decreases over the iterations but not continuously as it jumps to a higher value at the beginning of a new stage. The decrease in the misfit is a proof that the inversion tries at each stage to fit both lab and modelled data. Looking at the final inverted parameters results, we could expect that pseudo-observed data and modelled data do not match. But this not the case. Pseudo-observed and modelled data for shots 0 are depicted in Figure 6.7. The amplitude and phase of the surface waves match well. But on receivers 14 to 28, located at the lower surface of the model, we can observe a light difference amplitude for both data on the P-waves. A slight difference in amplitude is also observed at late arrivals for all receivers.

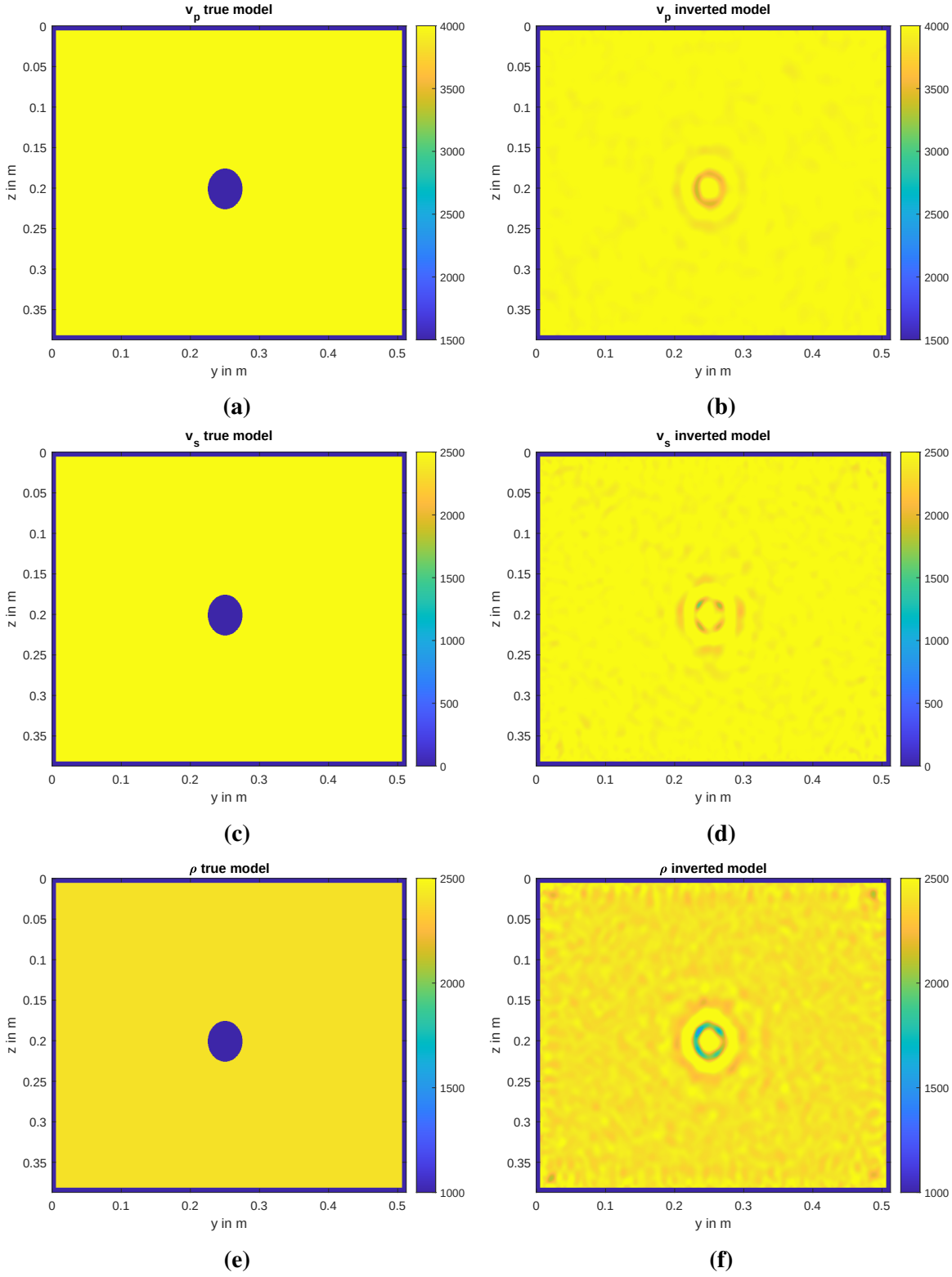

Figure 6.2: True models and results of the FWI of full data with water-filled pipe.

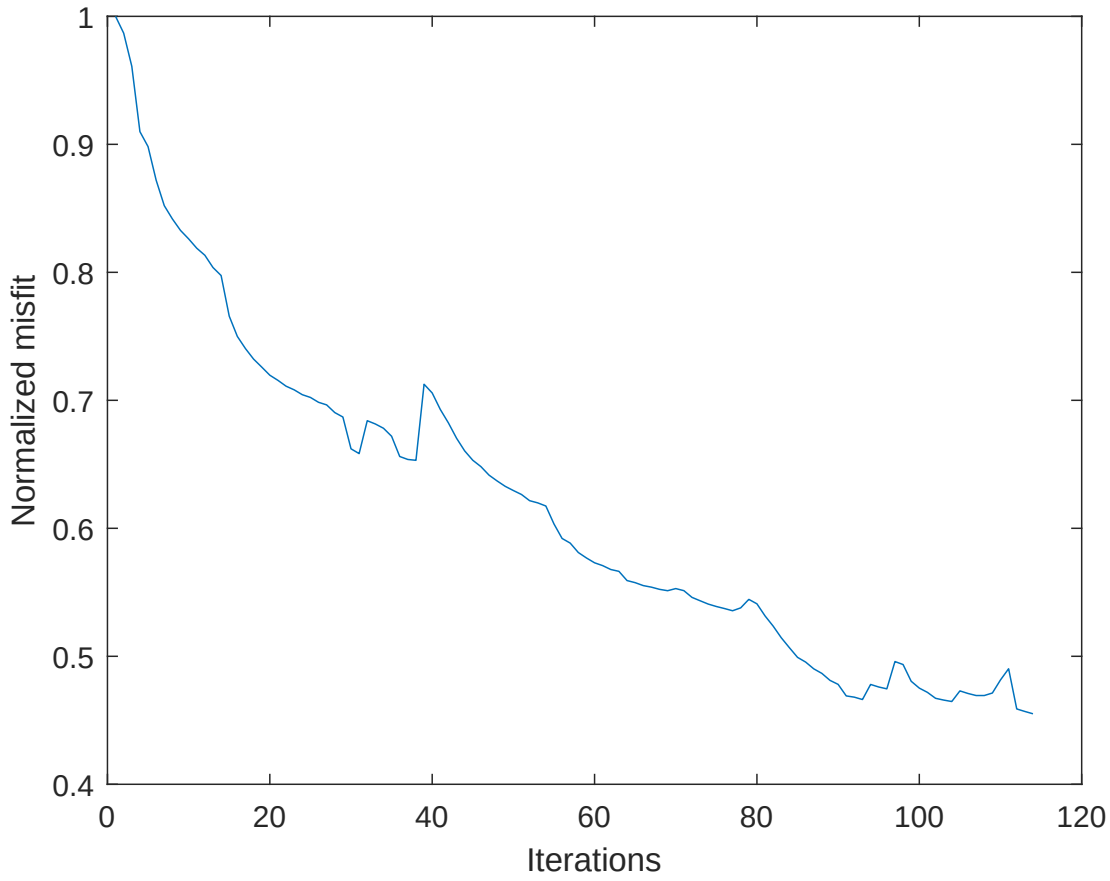

Figure 6.3: Evolution of the misfit function as the pipe is filled up with water. The full data content is inverted.

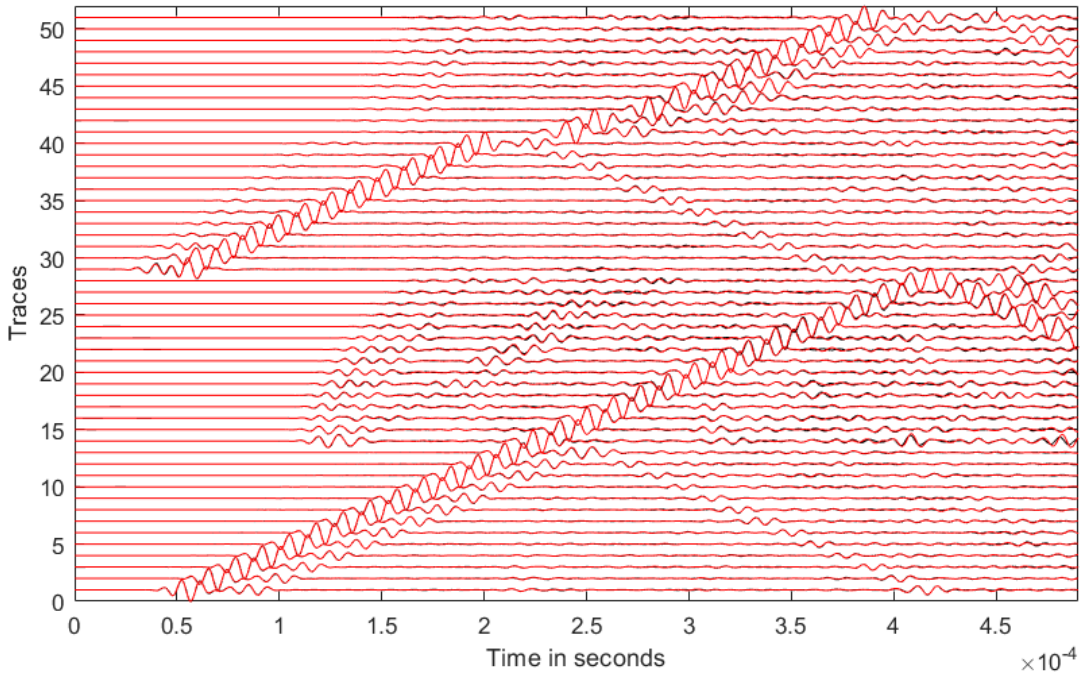

Figure 6.4: Comparison between the pseudo-observed data (black) and modelled data (red) for shot 0 after 114 iterations when the pipe is filed with water.

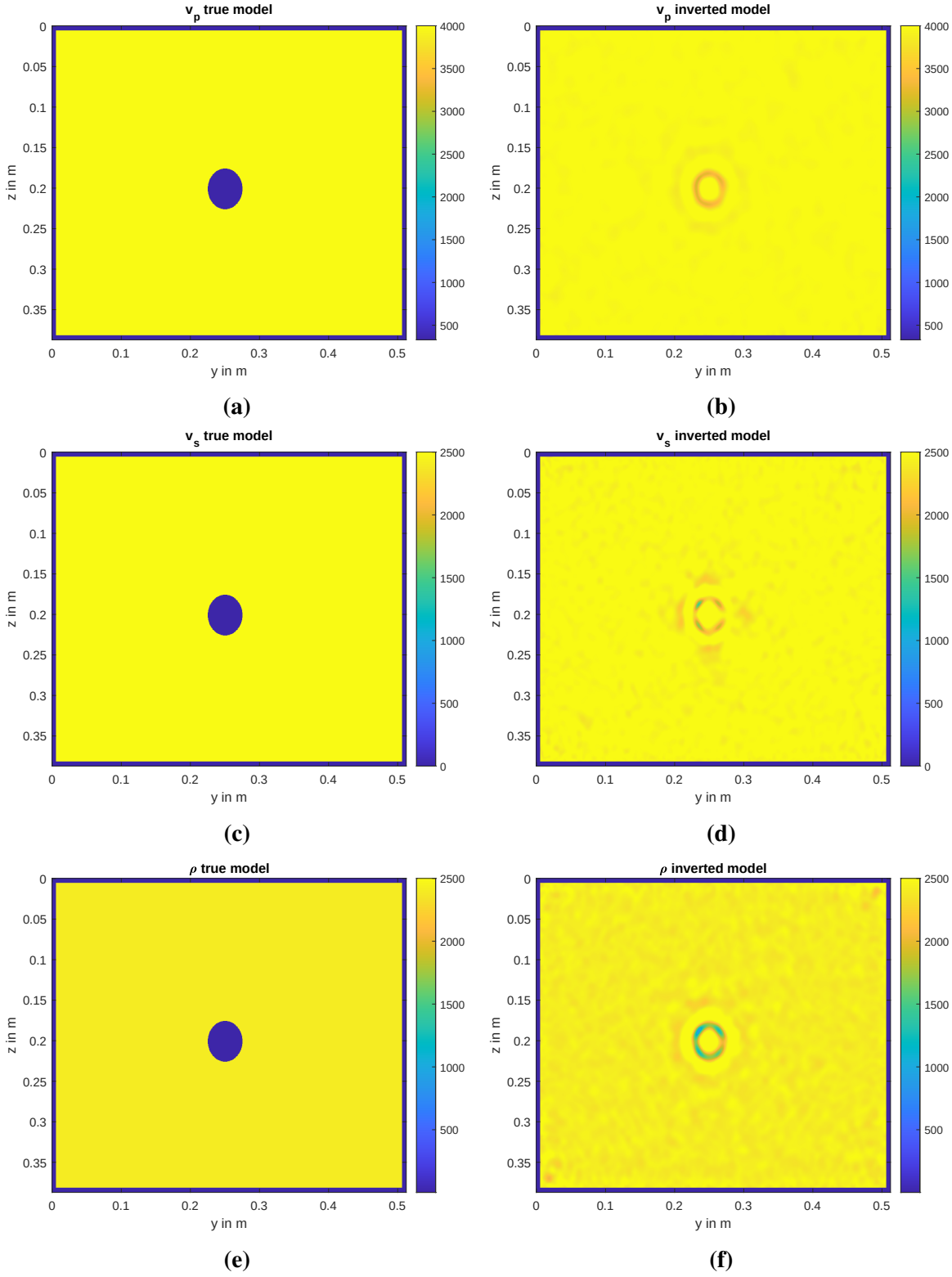

Figure 6.5: True models and results of FWI on full data with air-filled pipe.

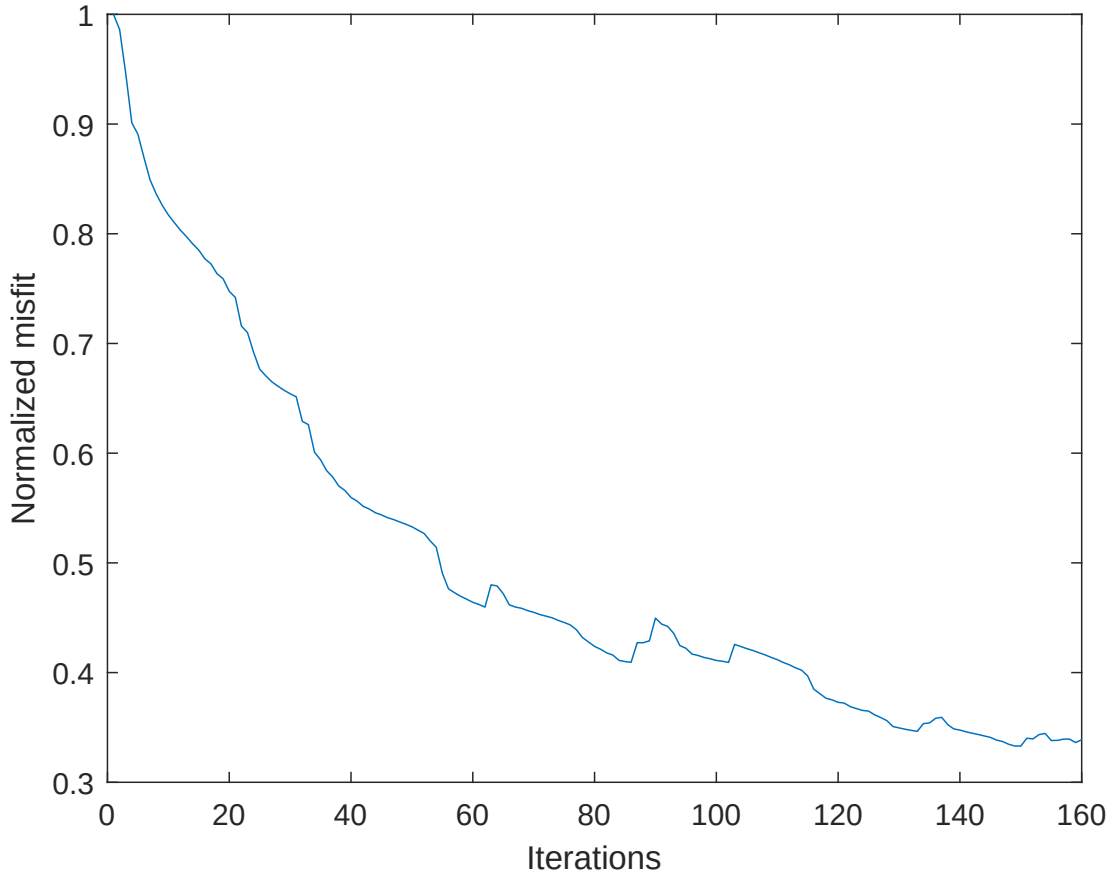

Figure 6.6: Evolution of the misfit function as the pipe is filled with air. The full data content is inverted.

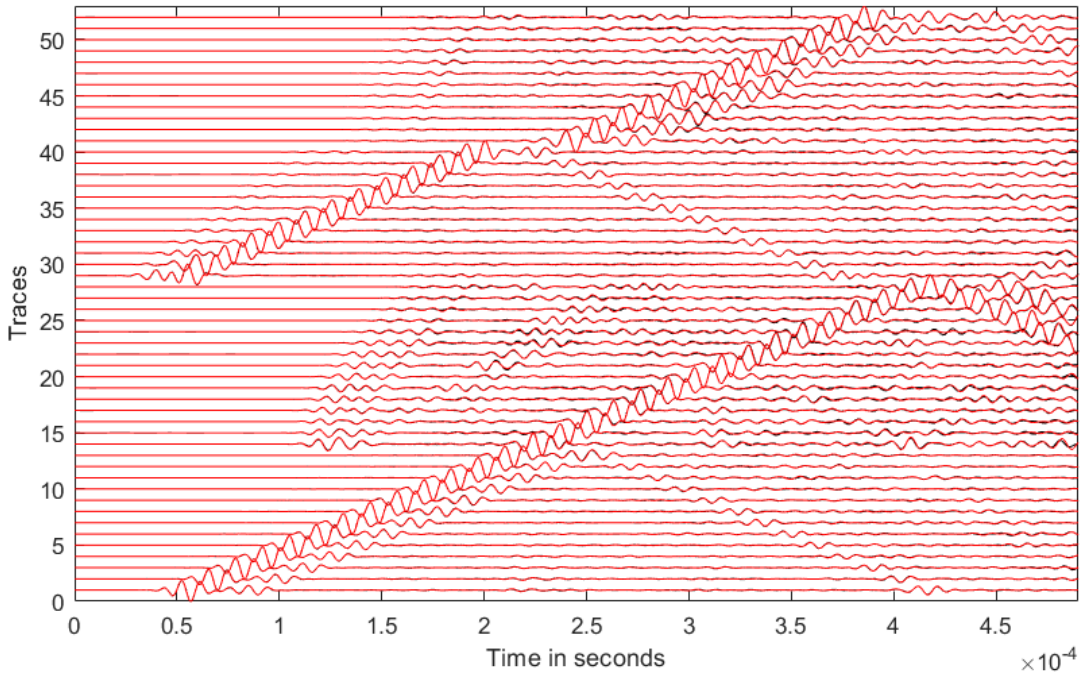

Figure 6.7: Comparsion between the pseudo-observed data (black) and modelled data (red) for shot 0 after 160 iterations when the pipe is filled with air.

6.2 Transmitted data inversion

The result of full data inversion was not good as one could only identify the pipe's dimensions and position but not the true velocity or density values. This reconstruction test aims to evaluate the feasibility of FWI on the lab data. But we observe in chapter 4, the far field in the pseudo-observed data is very complex as we cannot assign the origin of each wave. Moreover, Müller (2020) showed that it would be difficult to reconstruct the late arrivals of the different gathers in his work. When modelling the wavefield, I use as boundary conditions the free surface. So to avoid reflections from the edges of my model, I decided to mute them. Additionally, the direct Rayleigh waves travel only along the surfaces of the model and contained no information about the pipe. I am therefore not really interested in them. For these reasons, I apply a time gate to remove the unwanted components of each trace in my gathers and completely mute seismograms by which the surface waves arrive first and are dominant. Before applying this time window, I first select the receivers which have useful informations. I compare the wavefield of respectively a numerically homogeneous model and the true model. Using model in Figure 6.1, I model waves that I then compare with the synthetic reconstructed waves from chapter 5. In Figure 6.8, resulting seismograms for both the homogeneous and inhomogeneous models are plotted. On receivers 1 to 13, the amplitude of direct surface waves matches well together but is not of interest. It is essential to keep in mind that I am only interested in the first arrival package and reflections. I notice a difference in amplitude on receivers 14 to 28, located at the lower surface of the model. The difference in amplitude is present on the P-waves and the reflected waves which follow. There is a difference also in amplitude on receivers 41 to 51, located on the right side of the model. The scattered P-waves and the reflections which follow have different amplitude. I assume that this difference might be due to the presence of pipe in the model. I observe this same configuration difference for all shots located at the edge of the model. If a source is located in the middle of each side of the model, I observe a different configuration. The conclusion, therefore, is that the difference highly depends on the source/receiver positions. Because of these differences, I design a configuration to help select the receivers with useful information with respect to the source position. This configuration is presented in Table 6.2 After selecting my receivers, I define the time window function. If we look at seismograms on Figure 6.8, traces 14 to 28, the first arrival P-waves plus the reflections that follow have an average length of approximately $0.8 \times 10^{-4}\,\mathrm{s}$. Traces 41 to 51, both the P-waves and scattered waves have an average length of approximately $0.5 \times 10^{-4}\,\mathrm{s}$. This is important to design a uniform time window that takes all the information in . I select trace 2 of shot 0 to explain my window. Figure 6.9 shows the time gate and the selected trace. T_{start} is the arrival time of the signal at the receiver. To compute the arrival time, I use the normal moveout (NMO) equation stated as follows:

Table 6.2: The different traces from receivers used for FWI of transmitted waves. The configuration depends on the position of the source and is the same for both data sets.

Sources	Receivers positions			
	Top(v_y)	Bottom(v_y)	Left(v_x)	Right(v_x)
0	–	✓	–	✓
1	–	✓	–	✓
2	–	✓	✓	✓
3	–	✓	✓	✓
4	–	✓	✓	✓
5	–	✓	✓	–
6	–	✓	✓	–
7	✓	–	–	✓
8	✓	–	–	✓
9	✓	–	✓	✓
10	✓	–	✓	✓
11	✓	–	✓	✓
12	✓	–	✓	–
13	✓	–	✓	–
14	–	✓	–	✓
15	–	✓	–	✓
16	✓	✓	–	✓
17	✓	–	–	✓
18	✓	–	–	✓
19	–	✓	✓	–
20	–	✓	✓	–
21	✓	✓	✓	–
22	✓	–	✓	–
23	✓	–	✓	–

$$T_{start} = \frac{d^2 + \Delta x^2}{v^2}, \tag{6.1}$$

$$T_{end} = T_{start} + \Delta T \tag{6.2}$$

where d is the depth at which the receiver is located. Δx is the distance between the source and the receiver, and v is the velocity of P-waves in concrete block. $\Delta T = 0.8 \times 10^{-4}\,\mathrm{s}$ is used to ensure that all useful information is considered in the gather. At the end of the wavelet, a steep descending cosine taper with a length of $0.2 \times 10^{-4}\,\mathrm{s}$ is applied. This is to avoid an abrupt cut in the data. This taper reduces the number of samples from 7000 to 3429. For each shot, seismograms are tapered tracewise. Figure 6.10 shows shots 0 and 21 after selecting the receivers and applying the taper on the selected traces. The obtained gathers are then used for inversion.

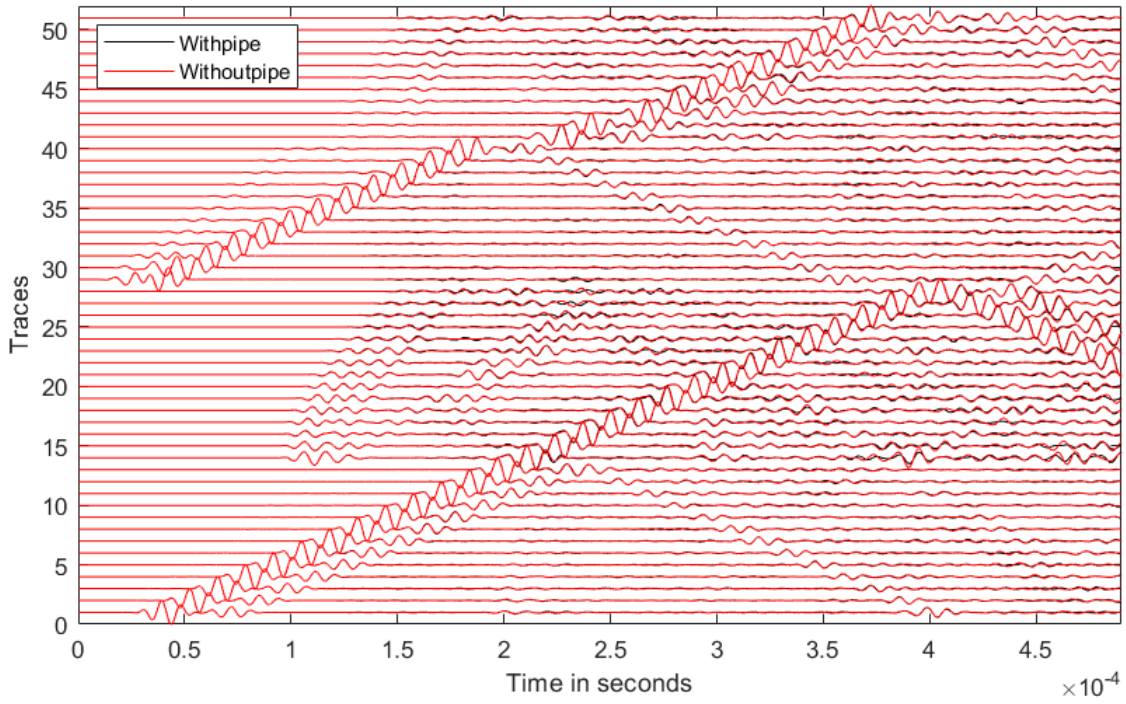

Figure 6.8: Comparison between the waves modelled using the homogeneous model (read) and the ones modelled using the true model (black). The trace are normalized.

6.2.1 Inversion settings

To invert the transmitted data, I use the L_2-Norm. To optimize the inversion, I apply the conjugate gradient and step length method (chapter 2). I still use the three cycles Hann-windowed tone bursts with only 3429 samples and still didn't perform a source inversion. The general algorithm of FWI shown in Figure 2.2 isn't the same as I taper the modelled data and pseudo-observed data during FWI. This very important to assure that the difference between the pseudo-observed and synthetic data is minimised. If this is not done, the model will not converge and will be unstable. The time window functions applied on pseudo-observed data before the inversion are also applied to modelled ones. These were saved in input files. I implemented in my code a taper function, which reads in the files and applies them to both data. I then define a gradient in other to circumcise a region where my model will be updated. The workflow of the transmitted data is shown in Table 6.3.

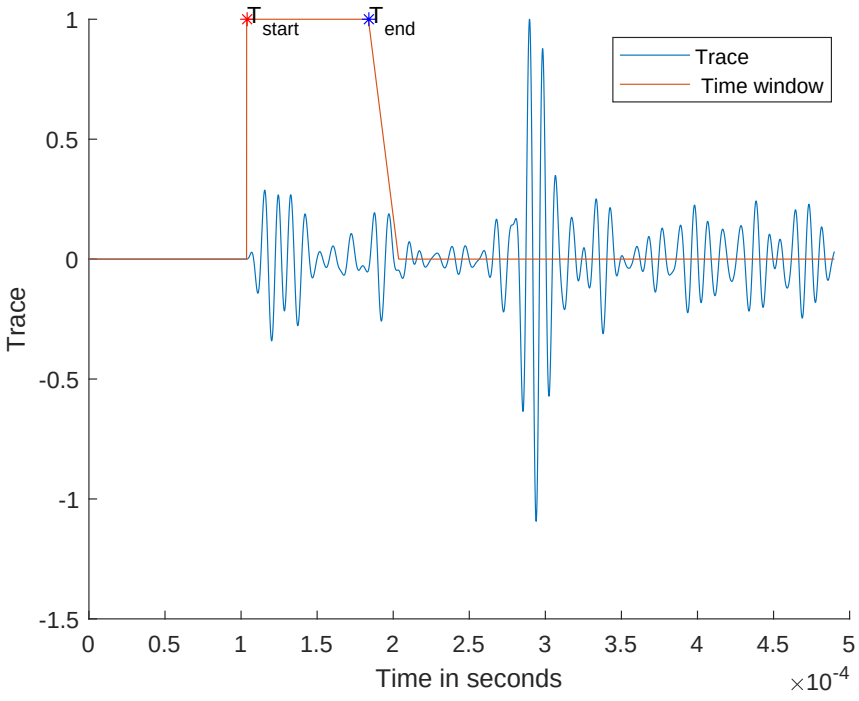

Figure 6.9: Trace 2 of shot 0 and an example of the time gate.

6.2.2 Inversion Results

6.2.3 Water-filled pipe data

The inversion ended up after 57 iterations. The inverted results are shown in Figure 6.11. The final models are not still good enough. We can see some artefacts in the region where the gradient taper is applied on all inverted results. In Figure 6.11a, we can identify the shape and position of the pipe. We can also see that the velocity content of the model starts to define itself. The boundaries of the inclusion are not continuous. But some velocities zones are identifiable. The final v_s is poor. This result is expected as I mainly used the P-waves to run the inversion, and no S-waves goes through the pipe. Compared to the two velocity models, the inverted ρ is better because it displays more information about the true density model.

The misfit function shown in Figure 6.12 is normalized. It has the shape of stairs. The jumps when the inversion is going to next stage are more steep. The misfit value decreases from 1 in the first stage to approximately 0.35 in final one. The misfit does not differ too much as the one for the full data inversion. I plot seismograms for shot 0 and 21 to further evaluate the inversion result (see Figure 6.13). For shots 0 and 21, the data fit for both pseudo-observed and modelled data works pretty well at first arrivals. This gets a little bit worse at late arrivals. On late arrivals, we observe a slight difference in amplitude in both data.

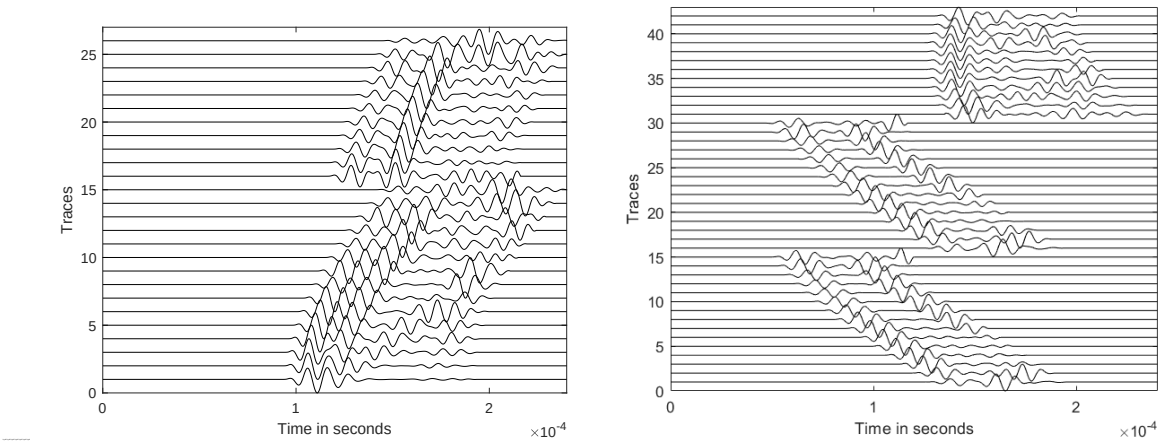

(a) **(b)**

Figure 6.10: Shots 0 (left) and 21 (right) after I apply the time window function. Traces are normalized and the number of receivers has reduced.

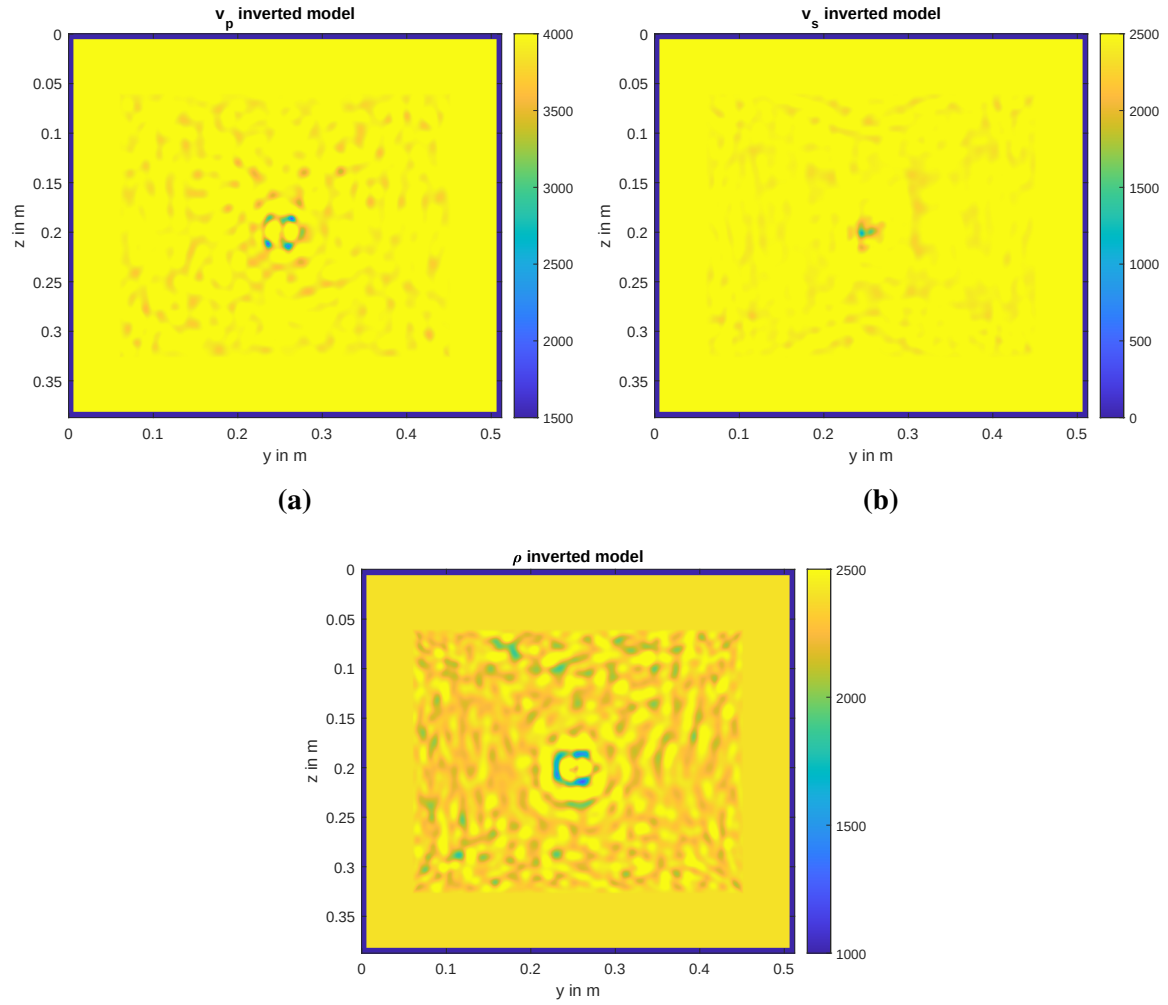

(a) **(b)**

(c)

Figure 6.11: The resulting inverted models using the transmitted waves. The pipe is filled with water.

Table 6.3: The workflow with different stages used to invert the transmitted waves for the water- and air- filled pipe datasets.

Medium	Lower frequency in kHz	High frequency corner in kHz	Relative misfit
Water	30	50	0.005
	30	60	0.005
	30	70	0.005
	30	80	0.005
	30	90	0.005
	30	100	0.005
	30	120	0.02
	30	140	0.02
	30	160	0.02
Air	30	50	0.005
	30	70	0.005
	30	80	0.005
	30	90	0.005
	30	100	0.005
	30	120	0.005
	30	140	0.005
	30	160	0.005

6.2.4 Air-filled pipe data

The inversion results for the air-filled pipe are shown in Figure 6.14. The inversion stopped after 44 iterations. The v_p inverted model is shown in figure 6.14a. We can identify the shape and position of the pipe but not clearly. Compare to the results of the full data inversion, the boundaries are not smooth. v_p value of the pipe can't however be clearly identified. There are tiny anomalies areas where the inclusion is located with relative value. These values are higher than that of the actual velocity. There are artefacts also around the pipe. v_s result is poor as neither the shape of the pipe nor its position is depicted. This result was also expected as I mostly use the information contained in P-waves for the inversion. The final result ρ inverted result is shown in Figure 6.14c. The inverted result is also poor. But at least we can better identify the actual position and the shape of the pipe.

The evolution of the misfit is shown in Figure 6.15. The value of the misfit decreases with the number of iterations. It also has the shape of steep stairs. The value of misfit at the end is ≈ 0.3 and is not better than the one obtained in the full wave content inversion. Looking at this, one could wait that the result will be better, but this not the case. The pseudo-observed data and the simulated one for shots 0 and 21 are shown in Figures 6.16a and 6.16b. As for the water-filled pipe data, both waves match very well for the first arrival package for both shots. However, there is a difference in amplitude for late arrivals.

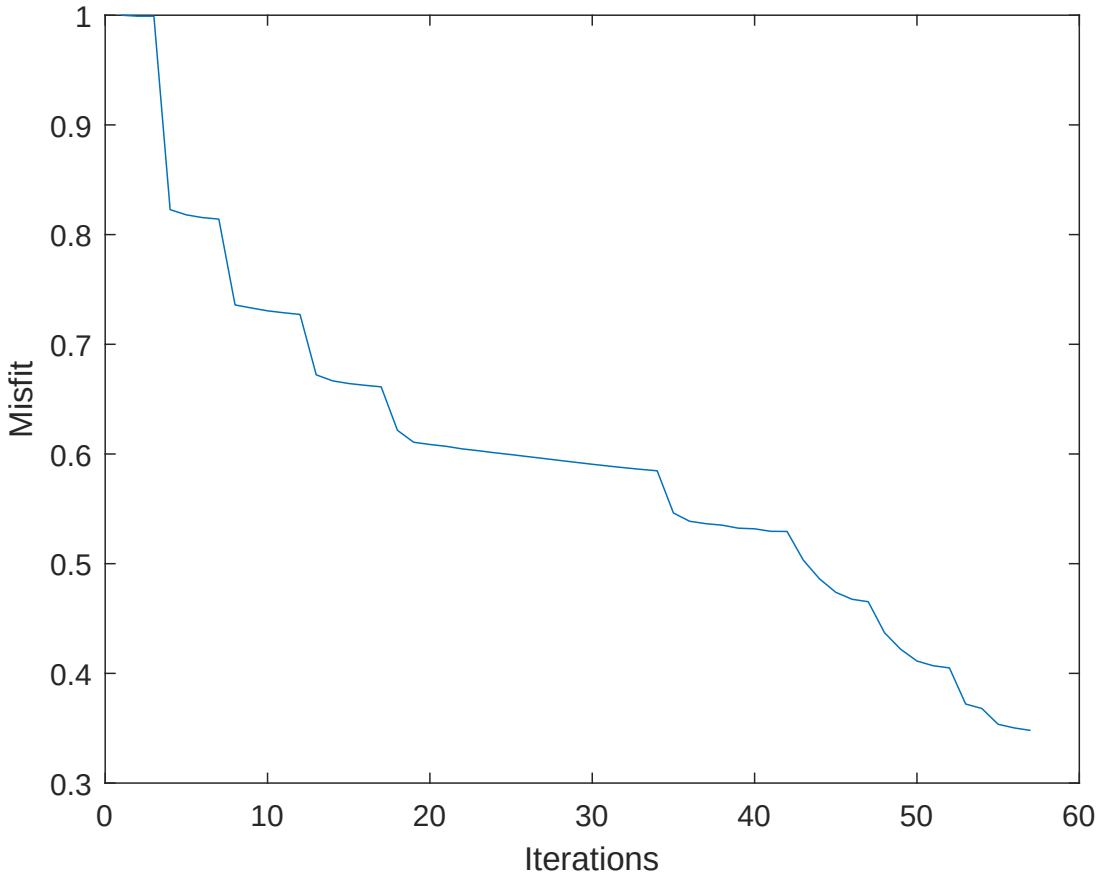

Figure 6.12: Evolution of the misfit function after FWI using transmitted waves.

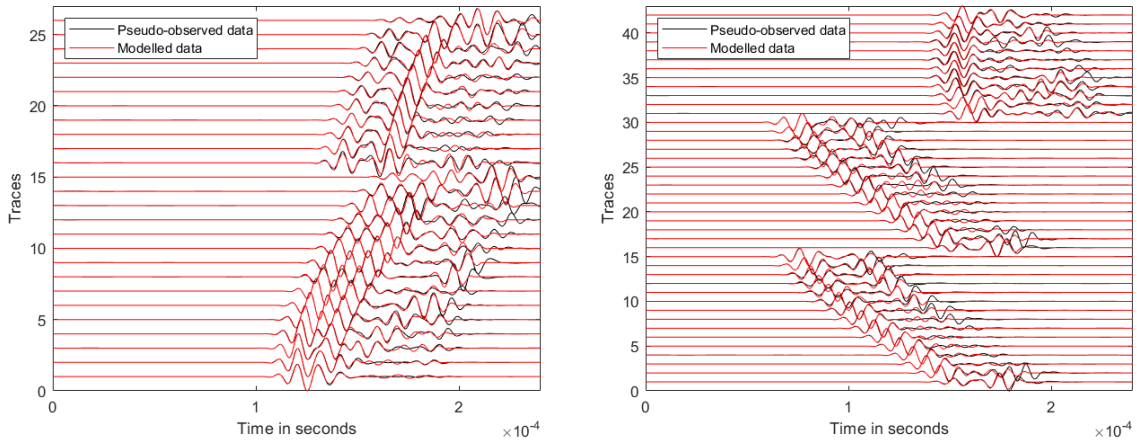

(a) **(b)**

Figure 6.13: Pseudo-observed waves (black) and modelled transmitted waves (red) for shot 0 (left) and shot 21 (right). The traces are normalized and tapered.

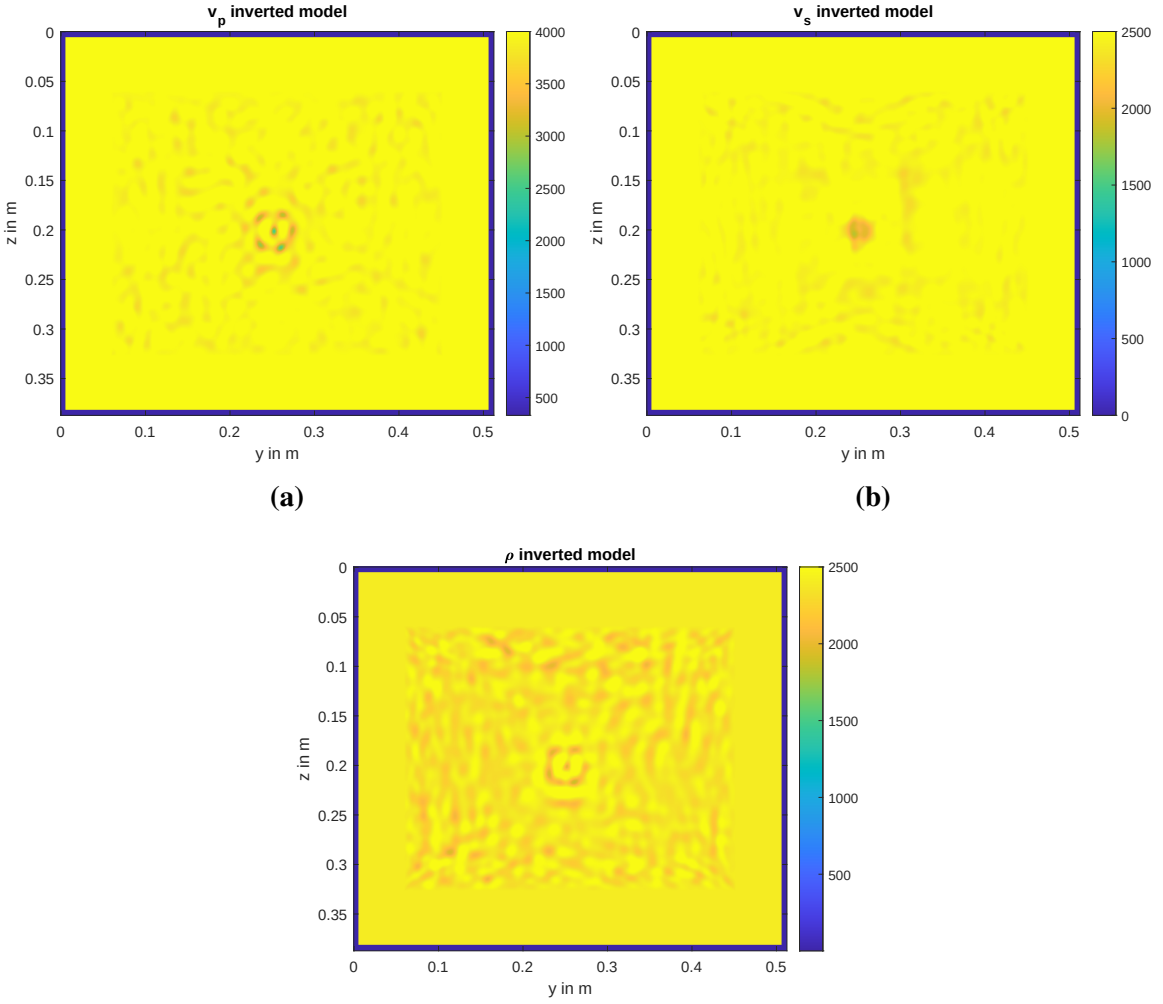

Figure 6.14: The resulting inverted models using the transmitted waves. The pipe is filled with air.

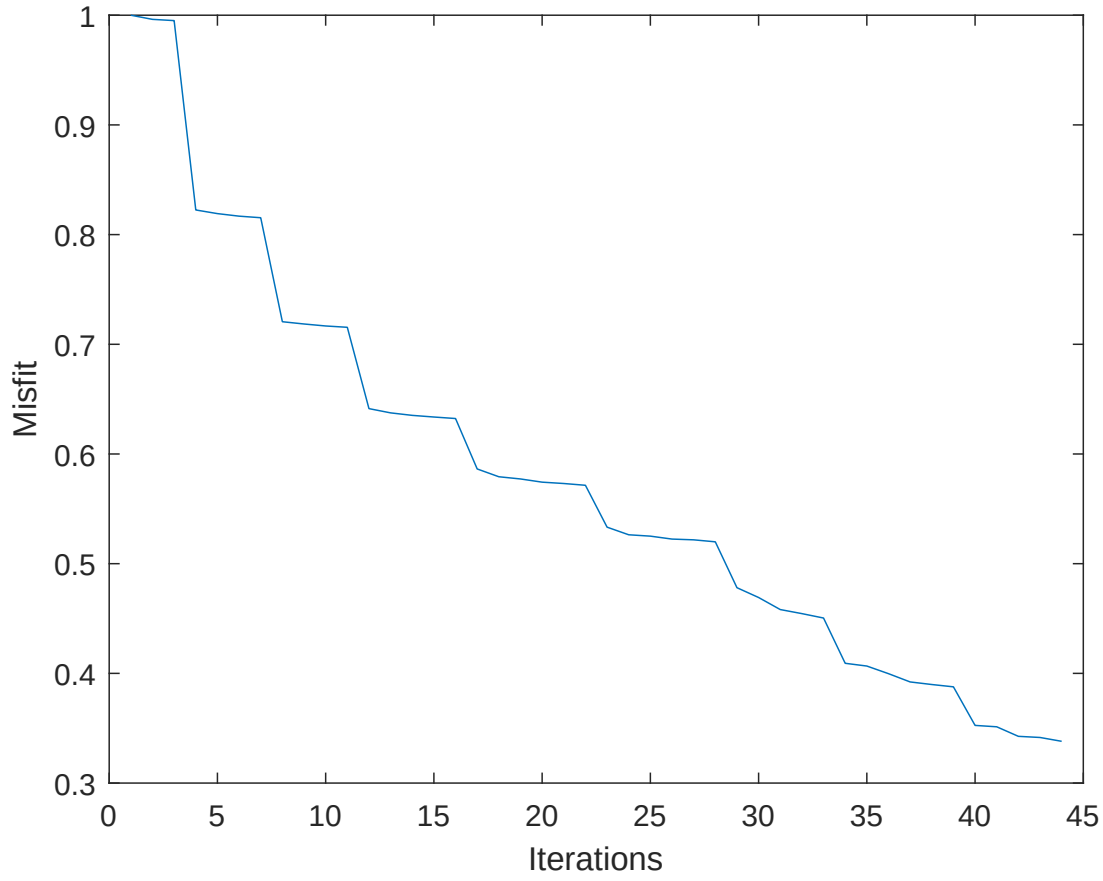

Figure 6.15: Evolution of the misfit function after FWI using transmitted waves. The pipe is filled with air.

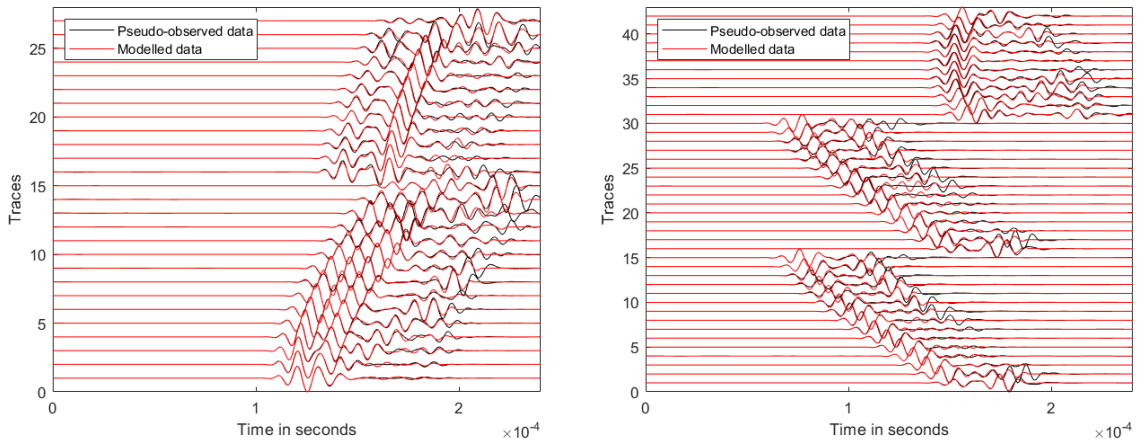

(a) **(b)**

Figure 6.16: Pseudo-observed waves (black) and modelled transmitted waves (red) for shot 0 (left) and shot 21 (right). The pipe is filled up with air. The traces are normalized and tapered.

6.3 Cross talk test

The results of previous inversion tests were good. The finals results of the model didn't converge to true velocity/density parameters. However the seismograms of the pseudo-observed data and the modelled data match well for the inversions with the full data content and the one with the transmitted waves. However the little improvement in the velocity model update I observe in the data inversion with transmitted data raise a question. This test helped me understand the inversion might actually converge if good conditions are set. One of the hypothesis, for poor result might be the high velocity contrast between the velocity in the concrete block and the one in the pipe. To confirm this hypothesis, I conduct one last test. Let us assume that instead of water or air inside the pipe, we have another concrete type. The model parameters in this medium are $\approx 10\%$ lower than the one in the concrete. So we have $v_p = 3400\,\mathrm{m/s}$. v_p, v_s, and ρ are inverted simultaneously. The final model for v_p is depicted in Figure 6.17. We can see that the shape and position of the pipe could be reconstructed and the velocity content. This result is also good for other parameters like v_s and ρ. The velocity contrast might be then one reason why true velocity/density in the previous tests couldn't be reconstructed.

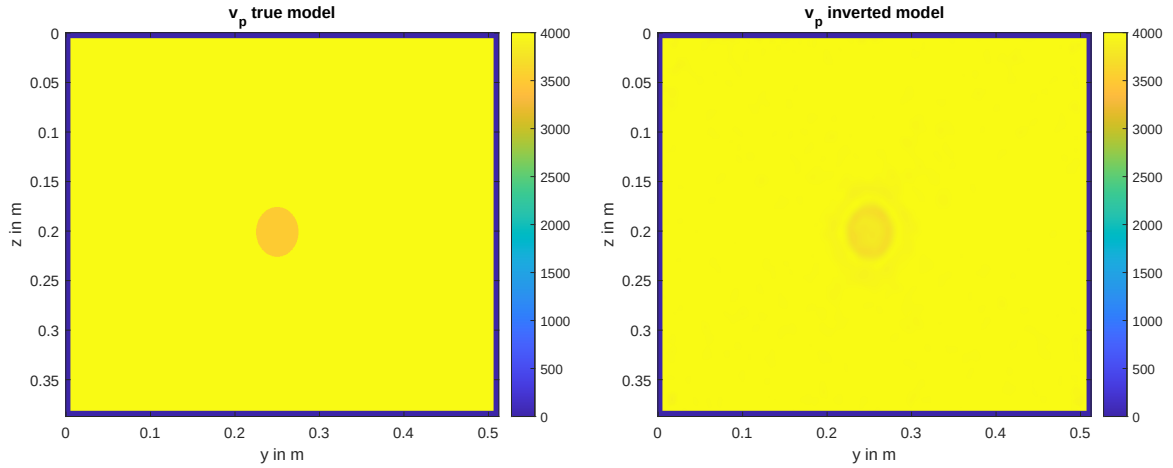

Figure 6.17: v_p inversion result for a pipe filled with another type of concrete.

6.4 Summary and discussion

In this chapter I present the results of all the synthetic inversion tests I perform for both datasets. With the full data content, the shape and position of the pipe could be reconstructed but not the true velocity or density values for both datasets. On one hand I notice that the density of inverted result for both datasets shows more information than the velocity. I cannot explain this observation. This is particularly interesting as it has been observed in past studies Thiel (2018). In the inversion results with the transmitted data, the shape for the pipe and

its position could be modelled for v_p, ρ. Moreover I could have more informations about the relative value of v_p for water-filled data. The result is no still good for the air-filled dataset as the true v_p couldn't be reconstructed. The fact that I could have some information about the true v_p for water and not for air, lead me to perform one last inversion test. In this, I invert the full content of the data but this time the pipe is filled up with another type of concrete. The inversion result proves that it is not possible to reconstruct the absolute v_p, v_s and ρ. The high velocity contrast between concrete and water/air might be a problem for the inversion.

Chapter 7

Inversion of laboratory data

In this chapter, I apply FWI to the water-filled lab data. Before using FWI, I correct the data for the geometrical spreading. Another challenge, I have to resolve is the approximation of the source time function. Because of the complexity of the coda at late arrivals observed in the lab data, I also taper to late arrivals waves. I discuss the challenges and the limitations of the inversion to the lab data.

7.1 Geometrical spreading correction

The concrete block used as model is a three dimensional body. This means that to apply 2D elastic inversion on the lab data, I have to correct for the geometrical spreading. The spreading in 2D differs from the one in 3D. This is because to generate field data point sources are used (in my work the DPC transducers), whereas to generate 2D data a line source is imagined. Schäfer et al. (2014) describe the *single-velocity transformation* to correct geometrical spreading, which works for elastic wave propagation. This consists of convolving the data $\sqrt{t^{-1}}$ (which produces a phase shift of $\pi/4$)and correct the amplitudes by multiplying them with $\sqrt{2rv_{ph}}$. r here is the distance between the source and the receiver (offset) and v_{ph} is the phase velocity. I neglect the constant $\sqrt{2v_{ph}}$ because I am not interested in absolute amplitude values but only relative ones. Figure 7.1 shows the point to line conversion for shot 1, when the pipe is filled up with water. The traces are normalized tracewise. The 3D to 2D conversion works pretty well on all the receivers. There is a little time shift between the two waves but the amplitudes match well. These is crucial steps to be sure that the we still have the same data.

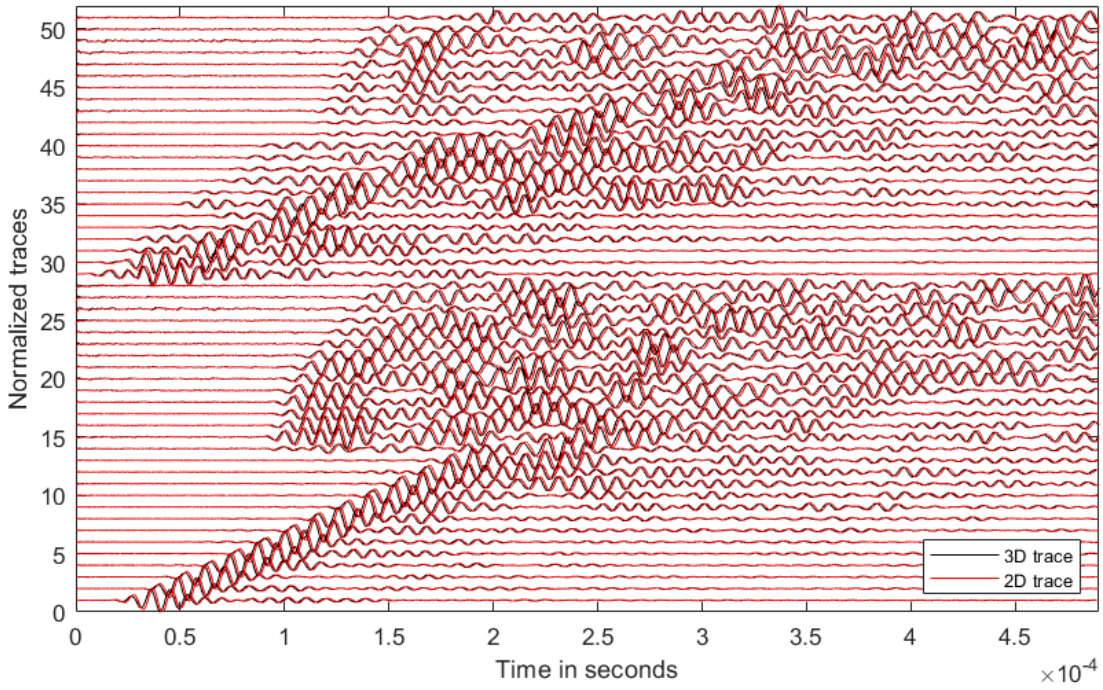

Figure 7.1: Comparison of the 3D seismograms (black) and 2D seimograms (red) of the lab data after geometrical spreading correction.

7.2 Data windowing

In chapter 6, I apply FWI to the full data and the transmitted waves. But the late arrivals coda for my real data is too complex and Rayleigh waves, reflected/refracted waves, cannot be differentiated from others. Moreover, Müller (2020) show that it will be difficult to reconstruct the far field coda. For these reasons, I decided to invert the transmitted waves of the lab data. I use the same configuration as the one in table6.2. So the number of traces per shot are reduced. The complexity of the other components of the shots leads me to also taper the data. To taper the data, I also define a time function for the data. The window I apply is different to that of the synthetic data. Adding to the steep descending cosine taper applied to the end of each trace, I use a steep ascending cosine taper at the beginning of each wavelet. I did this to taper the noise present before the P onsets for some receivers and to also avoid an abrupt cut at the beginning of the wavelet. Figure 7.2 below shows an example of the time window, which is applied on the trace 2 of shot 2. T_{start} and T_{end} are computed using equations 6.1 and 6.2. Both the ascending and descending tapers have the same length 0.2×10^{-4} s. After multiplying the trace and the window, it was reduced to only 3143 samples. Figure 7.3 shows trace 2 after multiplication with the time gate function.

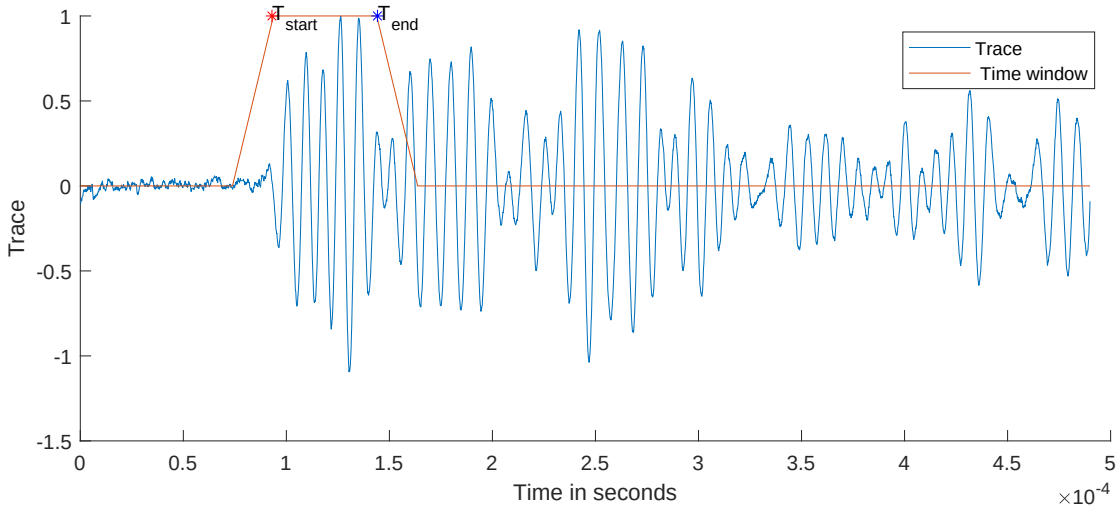

Figure 7.2: Trace 2 of shot 2 and the time gate function.

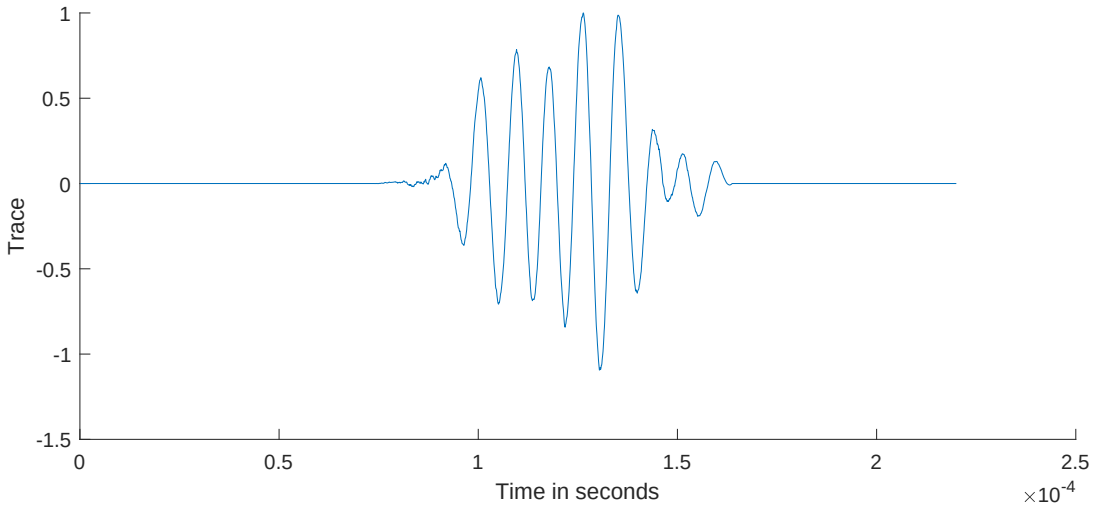

Figure 7.3: Result of tapering trace 2 of shot 2.

7.3 Source Time approximation

The source time used as input pulse to acquire the lab data was not given. So when doing inversion, I invert for the source. But before inverting the source time function, I approximate the transducer characteristics. This reduces the difference between the lab and synthetic data to ensure that FWI converges to a good model which could explain the observed data. According to the characteristics of the transducers , the DPC are oscillating point forces. So my source and receivers are point oscillating forces. The signal emitted by transducers is assumed not to be influenced (V. G. Shevaldykin et al., 2003). Müller (2020) proposed a successful approach to approximate the transducer characteristics. In his work, he assumed that the direct surface wave that arrived at the receiver has the same waveform as the original

source time function. This assumption is valid in reference to the characteristics of my transducers described by V. G. Shevaldykin et al. (2003). I follow this method.
Let us have a look over shot 0. As stated before, this shot is located at the top left of my model. The nearby receiver is located $6\,\mathrm{cm}$ away from it. So I choose the first trace and extract the direct surface wave. I design a time window with a steep descending cosine taper at its end. I then multiply this trace with the time window. I remove the first samples to ensure that the signal starts at $t = 0$. The time window and the trace are shown in Figure 7.4. Figure 7.5 depicts the final source time function.

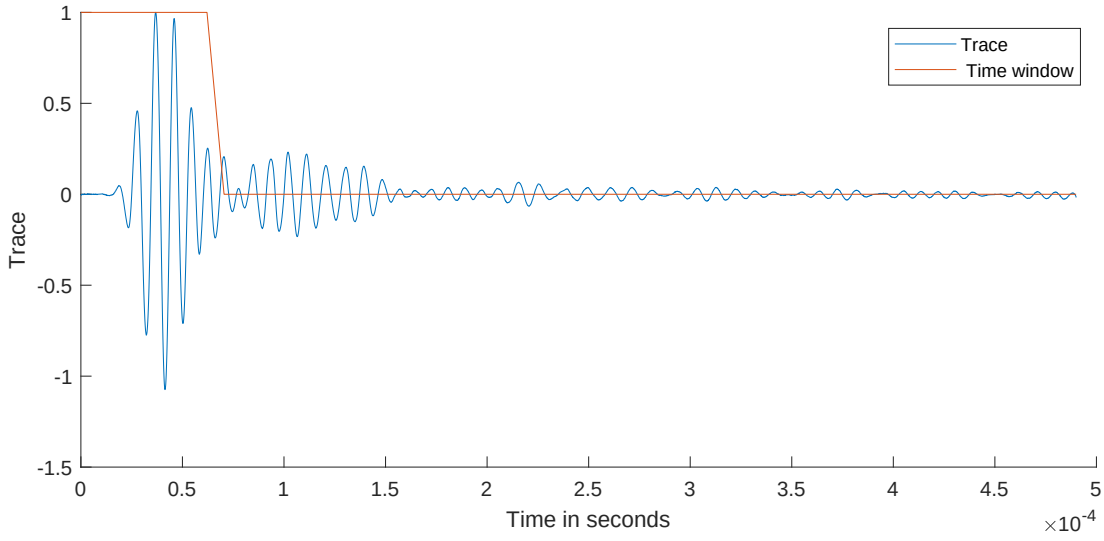

Figure 7.4: Approximation of the source time function. Trace 1 of shot 0 and the time gate function.

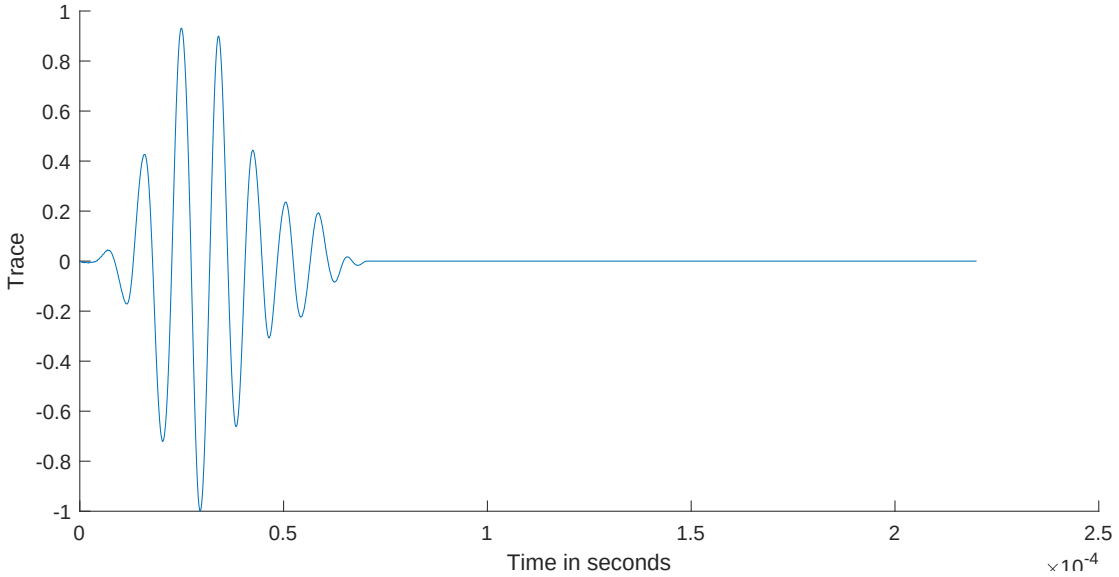

Figure 7.5: The source time function used in time inversion.

7.4 Inversion results

To invert the water-filled data, I use the initial model shown in figure 6.1 and the same settings as for the FWI performed in synthetic reconstruct. I also apply a gradient taper to the model. Instead of the multiscale approach, I first apply a one stage inversion in order to first evaluate FWI. The frequency range of the inversion lies between $0.01\,\mathrm{Hz}$-$150\,\mathrm{kHz}$. The maximum number of iterations is 30. The source signal function is inverted for each source. I invert for v_p, v_s ρ simultaneously.

The first test performed using transmitted waves ended after 24 iterations. The results for all the parameters are shown in Figure 7.6. In general, the results are poor. We cannot identity nor the pipe's shape or its position, or the velocity content. On the inverted v_p in Figure 7.6a, we can notice at a depth of $z = 5\,\mathrm{cm}$ one small anomaly. v_p in this inclusion is $\approx 3000\,\mathrm{m/s}$. This value is higher than the true velocity. At a depth of about $z = 30\,\mathrm{cm}$, we can observe a bigger inclusion with a velocity of about $3000\,\mathrm{m/s}$, closer to the true v_p value. In the centre of the model, around where the pipe is expected, we have a number of small anomalies. v_p in these anomalies lies between $2000\,\mathrm{m/s}$ and $3500\,\mathrm{m/s}$. These observations of the anomalies in the centre of the model tell us that the model converges but is no stable enough. There are artefacts in the final v_p model. On the final v_s and ρ results depicted in Figures 7.6a and 7.6a nothing appears. The result for v_s is understandable as no S-waves penetrates the water-filled pipe. The inverted ρ shows only artefacts. Nothing is updated. The misfit function of this inversion is shown in Figure fig:misrealall and it is normalized. The misfit drops only to about 10%, which is very small. To further evaluate the result of this inversion test, I plot both the lab and modelled data for shots 0 and 7 (see Figure fig:realtransallwater). For shot 0 7.8a, we first notice that the data fit is better for receivers 1 to 15 located directly opposite the source than for the receivers 16 to 26 located on the right side of the source. On receivers 1 to 15, the P-waves of both modelled and field data have the identical arrival time and are on the phase. For the receivers 16 to 26, the modelled waves reached the receiver late and have a different polarity than that of the lab data. However, around $T = 1.3 \times 10^{-4}\,\mathrm{s}$, this phase shift disappears. The polarity of both waves is inverted. On Figure 7.8b, the seismograms of the lab data are compared to the modelled data for shot 7. The data fit is bad for all the receivers as the modelled data arrived earlier than the lab one. But between $1.1 \times 10^{-4}\,\mathrm{s}$ and $1.3 \times 10^{-4}\,\mathrm{s}$ on receivers 1 to 15, the amplitudes of both seismograms match pretty. On the other side, for receivers 16 to 26, we can notice low frequency noise in the modelled data. They tend to be attenuated with far offsets. At late arrivals, amplitudes match also well. In all and all, the P-waves onsets cannot be defined accurately during the inversion. But at late arrivals the data fit is optimised. This is just the example of two shots. Taking a look at all my shots, I notice that the data fit between observed and modelled seismograms for almost receivers located directly opposite to the source is encouraging. So I decided to do an inver-

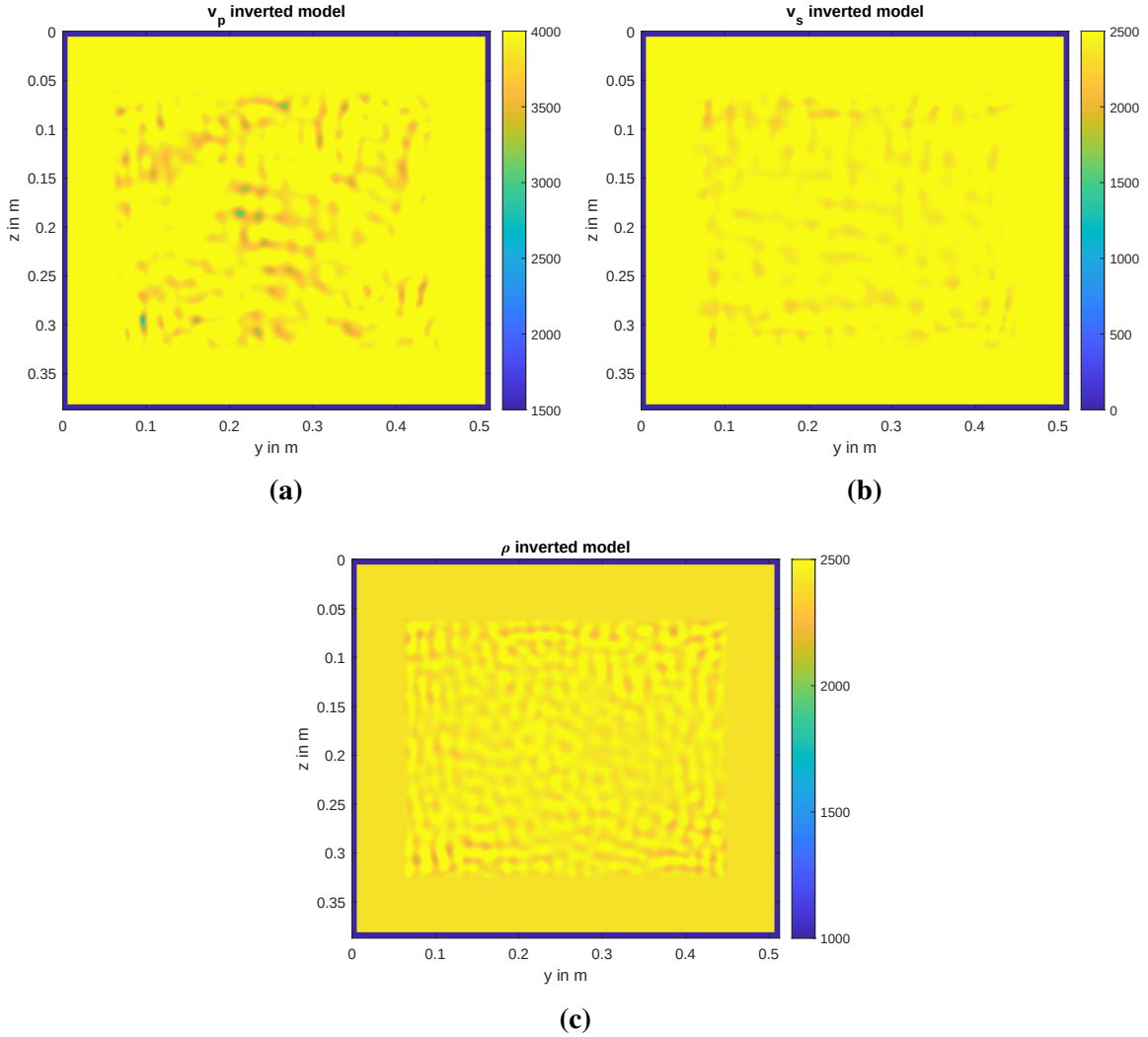

Figure 7.6: The resulting inverted models using the transmitted waves. The pipe is filled with water.

sion with only receivers located opposite to each source.

In the second inversion test, I inverted data only for receivers located opposite the source. So my receivers will have the same components as the source. The number of seismograms is reduced again, and the same tapers are used. The inversion is performed in one stage between $0.01\,\mathrm{Hz}$-$150\,\mathrm{kHz}$ and ended up after 22 iterations. The source time function inversion is still used. Figure 7.9 shows the inversion result. The inversion result is not still better overall. We still don't have any model update as far as v_s, ρ are concerned. But on for v_p inverted result (see Figure 7.9a), at a depth of $z = 20\,\mathrm{cm}$, at the location where the pipe is expected, we can see a smooth area having the shape of the pipe. This is already some information that the inversion tries to converge. This can also be explained as the misfit function decreases from 0.85 in first test to 0.75 in this test (see Figure 7.11). This amelioration of the misfit can be seen in the data fit for shots 0 shown in Figure 7.11. On one hand, for the two first

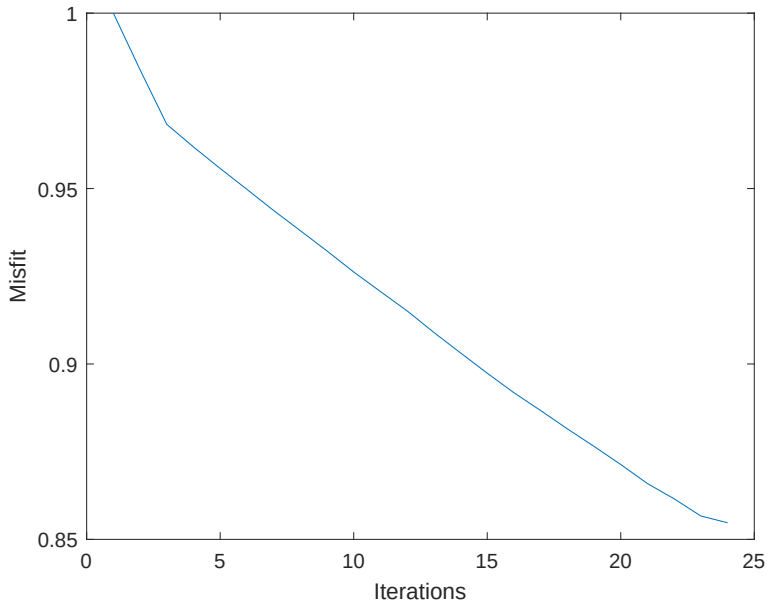

Figure 7.7: The evolution of the misfit function when inverting water-filled pipe with transmitted data.

receivers the amplitude of the inverted P-waves do not match those of the lab data. For the other receivers the phase and amplitude for both data match well for the first arrivals. This gets, however worse at late arrivals. On some traces like 12 to 16, there is some noise at the beginning of the traces. Since the inversion with races located directly opposite to each source work pretty well, I decide to perform one last inversion test.

For the last inversion, I remove all the shots for which I observe the high noise frequency noise which mostly located at the edges of my model. This reduces the number of shots to 20. Most of these. The inversion stopped after 24 iterations. Figure 7.12 shows the inverted v_p, the data fit for shot 0 and the evolution of the misfit function. v_p inverted result is better even though the noisy gathers have been removed. At the centre of the model, we can still observe a smooth area and some anomalies are still around it. If we have a look at Figure 7.12b, we can see that the data fit for the P-waves is good, whereas for the S-waves located on the right side of the model, this is still bad. The misfit gets worse as it increases from 0.75 in the second inversion to 0.86 (see Figure 7.12c). This means that the inversion does not improve even though information from other receivers is added.

All things considered, the reconstruction of the true velocity/density values of pipe is not possible looking at the above result. The inversion with the waves located directly opposite to the source show some improvements as we observe a smooth area around where the actual pipe is expected. But nothing exact. The data fit between the lab and modelled data at this stage is quite good as both phase and amplitude match well for early arrivals. For some

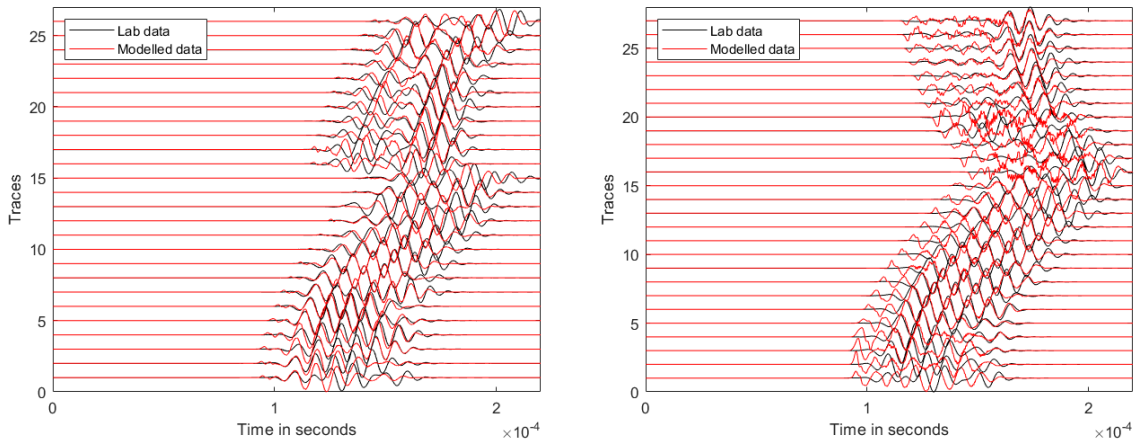

Figure 7.8: Lab data (black) and modelled transmitted waves (red) for shot 0 (left) and shot 21 (right). The pipe is filled up with air. The traces are normalized and tapered.

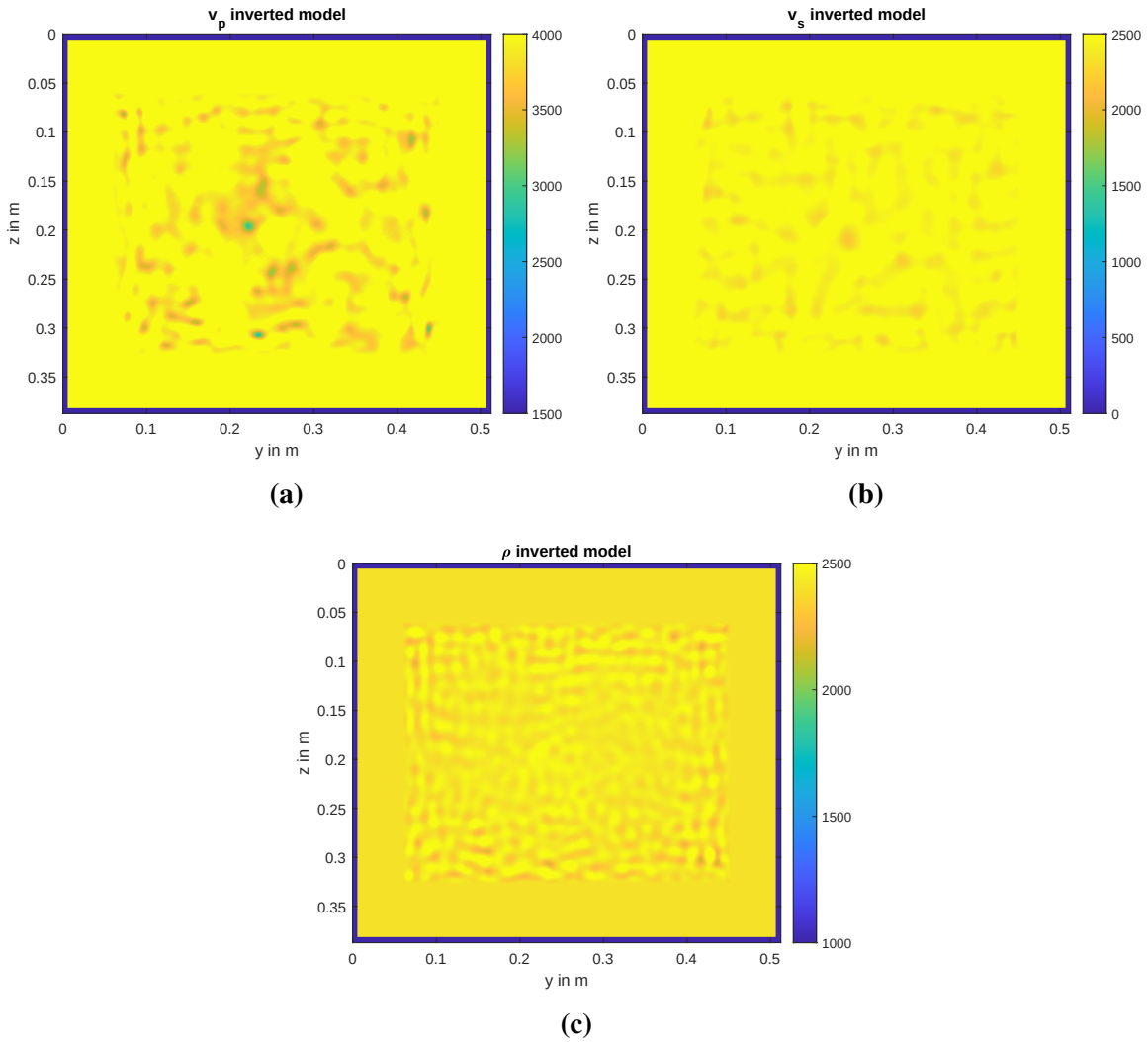

Figure 7.9: The resulting inverted models using traces located opposite to each source. The pipe is filled with water.

gathers, we observe some high frequency noise. The noise is mostly located at receivers having different components as the source. I cannot yet asset the origin of this high frequency noise. The data fit for the S-waves doesn't work well. The assumption for a line source is not correct in this work. This can be explained by the directivity characteristic displayed in Figure 3.4. The wavefront of the P-waves is strong perpendicular to the half surface. In this case, the point-line approximation works as we can see in our results. On the other hand this is not the case when the DPC radiates and emits ultrasound with an angle. The angle of radiation from the source has to be taken into account when calculating the displacement of the elastic waves. This has been studied by Danilov and Samokrutov (2004). I will refer the reader to this for more information. Due to time constraints I will not be able to exploit this condition.

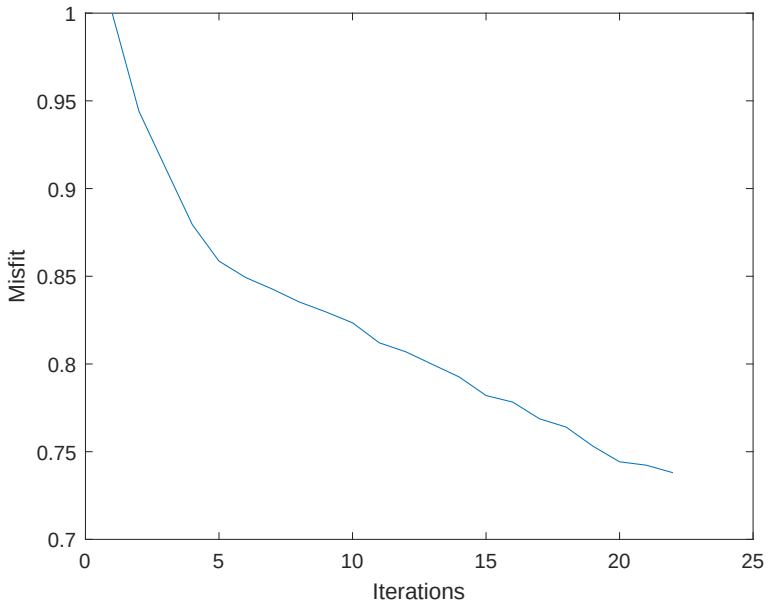

Figure 7.10: The evolution of the misfit function when only the receiver located opposite to the source are used. The misfit is normalized.

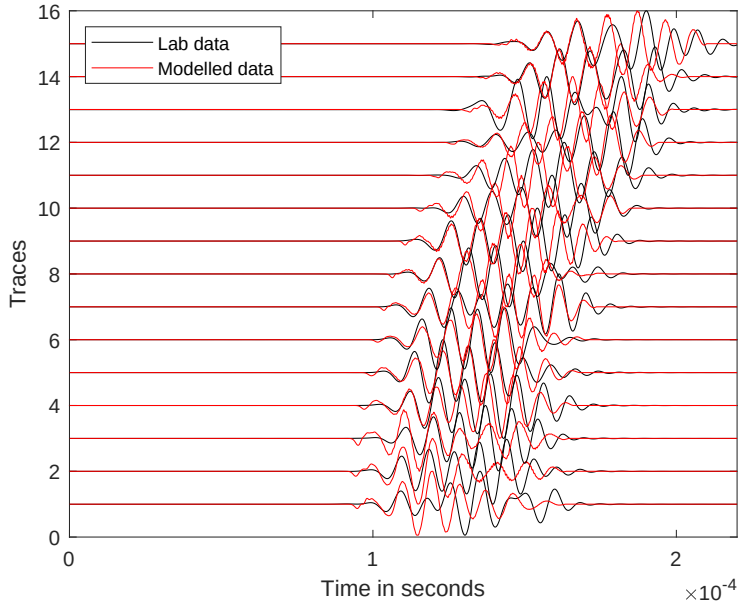

Figure 7.11: Comparison between lab data and modelled data for shot 0 when the receivers located opposite the source are used.

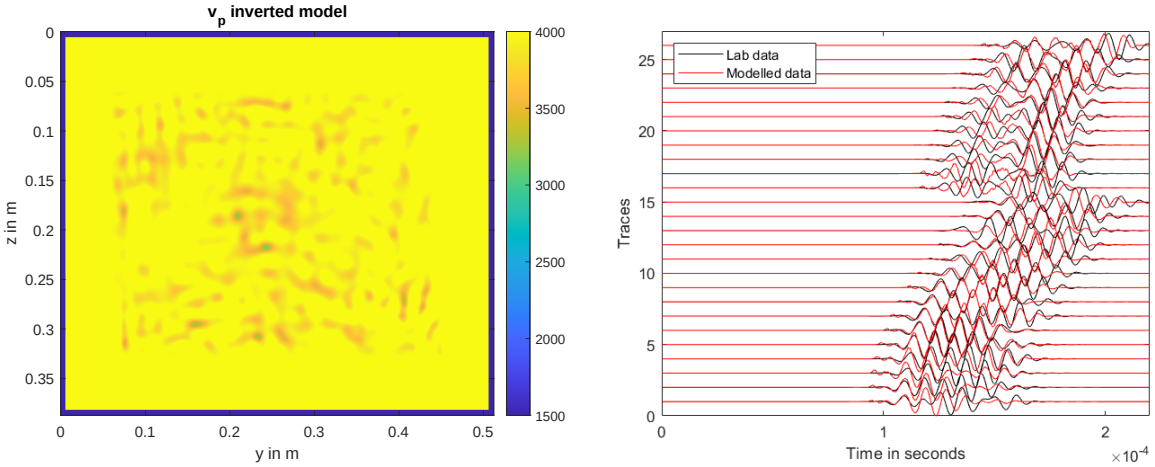

(a)

(b)

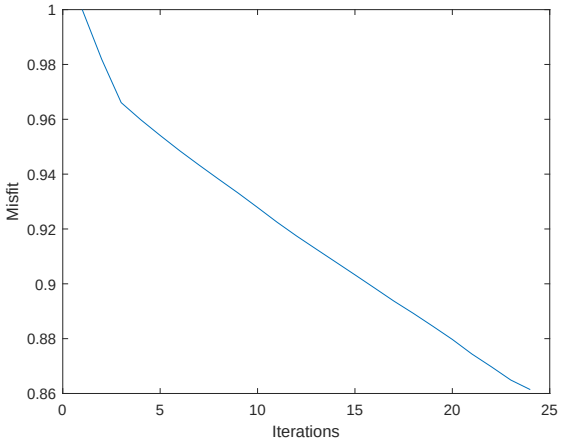

(c)

Figure 7.12: Left: v_p inverted result. Right:modelled and lab data for shot 0. Only 20 are used for the inversion.

Chapter 8

Conclusion

The purpose of this work was to evaluate the ability of FWI applied on ultrasonic data to map an anomaly located in a concrete structure in the case of NDT of materials. The anomaly in this study was a pipe filled with air in the first place and then with water. The data provided were acquired at the IZPF in Saarbrücken. Before applying FWI to the given data, I conducted some synthetic tests to investigate the feasibility of such a work.

Several 2D inversion tests show some challenges and limitations of the applications of FWI to ultrasonic data. I modelled two datasets: a water-filled pipe and an air-filled one. On both data sets, the main observation was that the surface waves were really dominant with very high amplitudes compared to the one of body waves. I first inverted the full data for the different parameters v_p, v_p and ρ. The inversion results, in general, were rather poor for both datasets. For all the final models, only the shape and position of the inclusion could be reconstructed. Even though we could deduce relative density/velocity information, the true values could not be determined accurately. In general, the inverted density model resembles its true structure much better than the velocity model. I could not explain this result as it has already been observed in other studies. It will be important to investigate this for further explanation.
In the second inversion test, only transmitted waves were used. I muted traces from receivers located near the source as they were highly dominated by the direct surface waves. This was mainly done as they travelled along the edges of the model and therefore contained no information about the pipe. Moreover, I tapered the late arrivals coda for the remaining traces. Analysing the lab data of both datasets shows that it will be complex to reconstruct the far field. The coda at late arrivals was very complex and I couldn't assign the origin of each wave. I applied a time gate to my seismograms, in order to consider only the first arrival of the body waves. I inverted for all the parameters. In the final v_p model, some information about velocity could be obtained for the water-filled pipe. But on the other side, the bound-

aries of the pipe could not be well reconstructed. The inversion result of v_s was still poor as mostly P-waves were used for the inversion and S-waves don not penetrate the pipe. The inversion result of v_p for air, was still poor as neither the true velocity nor the shape/position of the pipe could be imaged. This advises the cross talk test. In this test, the pipe was filled with another type of concrete. The result of this inversion, proved that the high contrast between the concrete and air/water might contribute to poor inversion results. This also explains why the inversion with transmitted waves is better when the pipe is filled with water as the contrast is lower. As the body waves reach the concrete-water/air interface, they are mostly reflected, thus provide almost no information about the media in the pipe.

The result of the synthetic data lead me to only consider lab water-filled data. Before inverting the lab data, I first converted them from 3D to 2D. Then I approximated the pulse emitted by the DPC transducer. As first application on the field data, I used the same configuration as in the synthetic reconstruction with transmitted waves. On one hand, the final model was poor for all the model parameters. The true parameters, shape and position could not be mapped. On the other hand, the data fit was quite good for traces from receivers located directly opposite to the source location. This leads me to conduct a second inversion test that only uses shots with good data fit for all traces. The result was poor as the true v_p could not be reconstructed. But at the location where the pipe was expected, we could identify a smooth area. The data fit was good, but not for all shots. I still observed some high frequency noise on some traces for shots located at the edges of my model. In the last test, I removed these shots. For the remaining shots, I consider the traces for receivers located both opposite and on the site of sources. Even though I removed the bad shots, the inversion didn't get better. As far as the data fit is concerned, it was still bad for traces located at the side of the sources. This might be due to the fact that the directivity characteristic of the transducer was not considered when calculating the displacement of the elastic waves. Adding to that, the high velocity contrast observed between media might have contributed to the poor result.

All in all, I think there is a great potential for NDT for materials using FWI on body waves. The high velocity contrast between media most likely contributes to the poor result. Another step to improve the inversion might be the implementation of the directivity characteristic in the forward modelling. As it will take into account the angle of radiation and reception of the waves in the inversion. This study shows that FWI is a good imaging tool for NDT. Further investigations with other datasets may also help in evaluating this potential.

References

ACS. (2018). A1220 monolith operation manual [Computer software manual].

Agudo, O. C., Guasch, L., Huthwaite, P., & Warner, M. (2018). 3d imaging of the breast using full-waveform inversion. In *Proc. int. workshop med. ultrasound tomogr.* (pp. 99–110).

Aki, K., & Richards, P. G. (2002). *Quantitative seismology*. University Science Books.

Almansouri, H., Johnson, C., Clayton, D., Polsky, Y., Bouman, C., & Santos-Villalobos, H. (2017). Progress implementing a model-based iterative reconstruction algorithm for ultrasound imaging of thick concrete. In *Aip conference proceedings* (Vol. 1806, p. 020016).

Asgharzadeh, M., et al. (2018). The use of fwi in coal exploration. *ASEG Extended Abstracts*, *2018*(1), 1–7.

Baby, S., Balasubramanian, T., Pardikar, R., Jayakumar, T., Rajkumar, K., & Raj, B. (2004). Sizing of cracks embedded in sub-cladding using the ultrasonic synthetic aperture focusing technique (saft). *Insight-Non-Destructive Testing and Condition Monitoring*, *46*(1), 26–30.

Bohlen, T. (1998). *Viskoelastische fd-modellierung seismischer wellen zur interpretation gemessener seismogramme* (Unpublished doctoral dissertation). Christian-Albrechts-Universitat zu Kiel.

Bohlen, T. (2002a). Parallel 3-d viscoelastic finite difference seismic modelling. *Computers & Geosciences*, *28*(8), 887–899.

Bohlen, T. (2002b). Parallel 3-D viscoelastic finite difference seismic modelling. *Computers & Geosciences*, *28*(8), 887–899.

Bunks, C., Saleck, F. M., Zaleski, S., & Chavent, G. (1995). Multiscale seismic waveform inversion. *Geophysics*, *60*(5), 1457–1473.

Courant, R., Friedrichs, K., & Lewy, H. (1928). Über die partiellen differenzengleichungen der mathematischen physik. *Mathematische annalen*, *100*(1), 32–74.

Danilov, V., & Samokrutov, A. (2004). Simulation of operation of dry point contact probes in the emission regime. *Russian journal of nondestructive testing*, *39*(8), 577–588.

Fichtner, A. (2010). *Full seismic waveform modelling and inversion*. Springer Science & Business Media.

Köhn, D. (2011). *Time domain 2d elastic full waveform tomography* (Unpublished doctoral dissertation).

Köhn, D., Meier, T., Fehr, M., De Nil, D., & Auras, M. (2016). Application of 2d elastic rayleigh waveform inversion to ultrasonic laboratory and field data. *Near Surface Geophysics*, *14*(5), 461–467.

Krause, M., Milmann, B., Mielentz, F., Streicher, D., Redmer, B., Mayer, K., ... Schickert, M. (2008). Ultrasonic imaging methods for investigation of post-tensioned concrete structures: a study of interfaces at artificial grouting faults and its verification. *Journal of Nondestructive Evaluation*, *27*(1-3), 67–82.

Lay, T., & Wallace, T. C. (1995). *Modern global seismology*. Elsevier.

Levander, A. R. (1988). Fourth-order finite-difference p-sv seismograms. *Geophysics*, *53*(11), 1425–1436.

Müller, J. (2020). *2d elastic full-waveform inversion of ultrasonic data for non-destructive testing* (Unpublished master's thesis). Karlsruher Institut Technologie, XXX.

Müller, G. (2007). *Theory of elastic waves*. Geoforschungszentrum Potsdam.

Müller, S., Niederleithinger, E., & Bohlen, T. (2012). Reverse time migration: A seismic imaging technique applied to synthetic ultrasonic data. *International Journal of Geophysics*, *2012*.

Nguyen, L. T., & Modrak, R. T. (2018). Ultrasonic wavefield inversion and migration in complex heterogeneous structures: 2d numerical imaging and nondestructive testing experiments. *Ultrasonics*, *82*, 357–370.

Nguyen, T. D., Tran, K. T., & Gucunski, N. (2017). Detection of bridge-deck delamination using full ultrasonic waveform tomography. *Journal of Infrastructure Systems*, *23*(2), 04016027.

Nocedal, J., & Wright, S. (2006). *Numerical optimization*. Springer Science & Business Media.

Plessix, R.-E. (2006). A review of the adjoint-state method for computing the gradient of a functional with geophysical applications. *Geophysical Journal International*, *167*(2), 495–503.

Plessix, R.-E., & Mulder, W. (2004). Frequency-domain finite-difference amplitude-preserving migration. *Geophysical Journal International*, *157*(3), 975–987.

Polak, E., & Ribiere, G. (1969). Note sur la convergence de méthodes de directions conjuguées. *ESAIM: Mathematical Modelling and Numerical Analysis-Modélisation Mathématique et Analyse Numérique*, *3*(R1), 35–43.

Pratt, R. G. (1999). Seismic waveform inversion in the frequency domain, part 1: Theory and verification in a physical scale model. *Geophysics*, *64*(3), 888–901.

Rao, J., Ratassepp, M., & Fan, Z. (2016a). Guided wave tomography based on full waveform inversion. *IEEE transactions on ultrasonics, ferroelectrics, and frequency control*, *63*(5), 737–745.

Rao, J., Ratassepp, M., & Fan, Z. (2016b). Limited-view ultrasonic guided wave tomography using an adaptive regularization method. *Journal of Applied Physics*, *120*(19), 194902.

Schäfer, M., Groos, L., Forbriger, T., & Bohlen, T. (2014). Line-source simulation for shallow-seismic data. part 2: full-waveform inversion—a synthetic 2-d case study. *Geophysical Journal International*, *198*(3), 1405–1418.

Seidl, R. (2018). *Full waveform inversion for ultrasonic nondestructive testing* (Unpublished doctoral dissertation). Technische Universität München.

Seidl, R., & Rank, E. (2016). Iterative time reversal based flaw identification. *Computers & Mathematics with Applications*, *72*(4), 879–892.

Shevaldykin, V., Samokrutov, A., & Kozlov, V. (2002). Ultrasonic low-frequency transducers with dry dot contact and their applications for evaluation of concrete structures. In *2002 ieee ultrasonics symposium, 2002. proceedings.* (Vol. 1, pp. 793–798).

Shevaldykin, V. G., Samokrutov, A. A., & Kozlov, V. N. (2003). Ultrasonic low-frequency short-pulse transducers with dry point contact. development and application. In *International symposium non-destructive testing in civil engineering (ndt-ce) in berlin, germany.*

Tarantola, A. (1984). Inversion of seismic reflection data in the acoustic approximation. *Geophysics*, *49*(8), 1259–1266.

Thiel, N. (2018). *Acoustic and elastic fwi of marine dual-sensor streamer data in the presence of salt* (Unpublished doctoral dissertation). KIT-Bibliothek.

Thomas, G., Emadi, A., Mijares-Chan, J., & Buchanan, D. A. (2014). Low frequency ultrasound ndt of power cable insulation. In *2014 ieee international instrumentation and measurement technology conference (i2mtc) proceedings* (pp. 1126–1129).

van der Kruk, J., Kalogeropoulos, A., Hugenschmidt, J., Klotzsche, A., Busch, S., & Vereecken, H. (2014). Full-waveform inversion of gpr data for civil engineering applications. In *Egu general assembly conference abstracts* (p. 16051).

Virieux, J. (1986). P-sv wave propagation in heterogeneous media: Velocity-stress finite-difference method. *Geophysics*, *51*(4), 889–901.

Wright, S., & Nocedal, J. (1999). Numerical optimization. *Springer Science*, *35*(67-68), 7.

Zahradník, J. í., Moczo, P., & Hron, F. e. (1993). Testing four elastic finite-difference schemes for behavior at discontinuities. *Bulletin of the Seismological Society of America*, *83*(1), 107–129.

Zeng, C., Xia, J., Miller, R. D., & Tsoflias, G. P. (2012). An improved vacuum formulation for 2d finite-difference modeling of rayleigh waves including surface topography and internal discontinuities. *Geophysics*, *77*(1), T1–T9.

List of Figures

List of Tables

Chapter 9

Acknowledgements

I would like to thank first of all my supervisor Professor Thomas Bohlen for giving me the opportunity to continue the research already started by Jonas Müller. I am particularly grateful as he believed in me during this project and was always available for discussion about my results. I am also grateful Professor Joachim Richter who accepted to be my second supervisor.
I would like to thank the Fraunhofer Institute for Non-destructive Testing for giving me access to their laboratory and providing the test model and data for this work.
A special thanks goes to Martin Kurras, Lennart Friedrich and the IZFP Saabrücken, who kindly invited us to assist in the data acquisition on the the concrete block, and were always ready to answer our questions.
I will like to thank Thomas Hertweck for helping in administrative and IT issues.
This thesis wouldn't have been possible without Jonas. He raised my interest for FWI in NDT and his work helped me to better understand the subject.
I would like to acknowledge Tilman, Mark and Tan, who were always available to answer questions relative to the software.
I wish also to thank Benedikt, Sonia and Martin for proofreading this thesis. All your comments helped me improve the quality of this work-
I also want to thank my office mate Hoang, for the discussions we had. You made this period less stressing.
In addition, I would like to thank Armelle and Bessam, for always encouraging me.
My deep gratitude goes to all my family and most especially to my late dad.
Last but not least I will like to give glory to the God almighty for strengthening me along this journey.

Chapter 10

Declaration of oath

I declare that I have developed and written the enclosed thesis completely by myself, and have not used sources or means without declaration in the text.

Priscilla Ntengue

Appendix A

Location of the measurements points on the concrete block

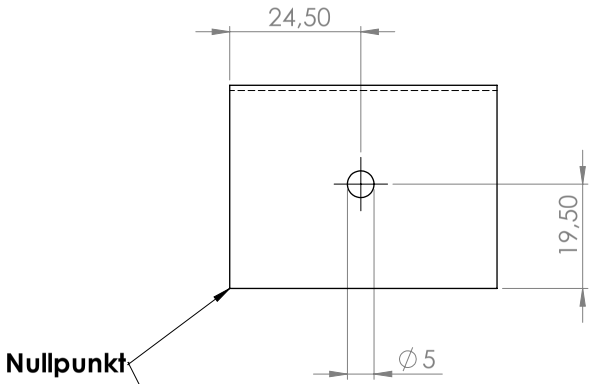

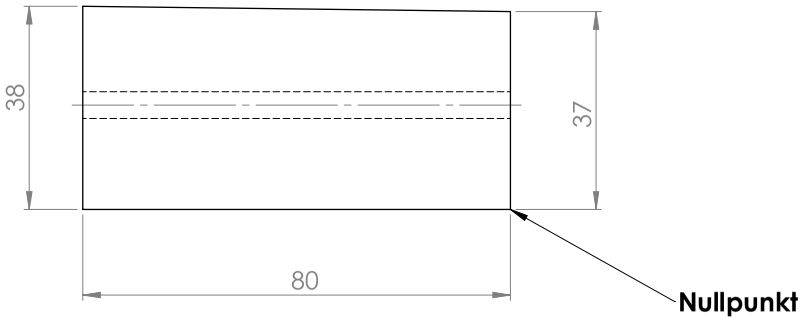

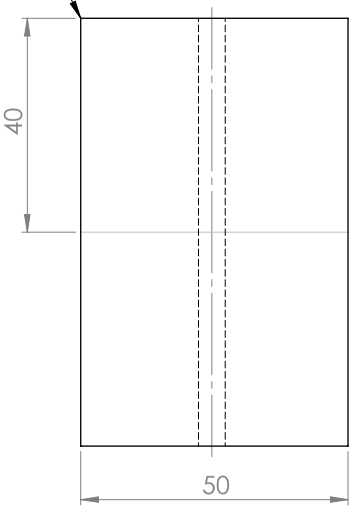

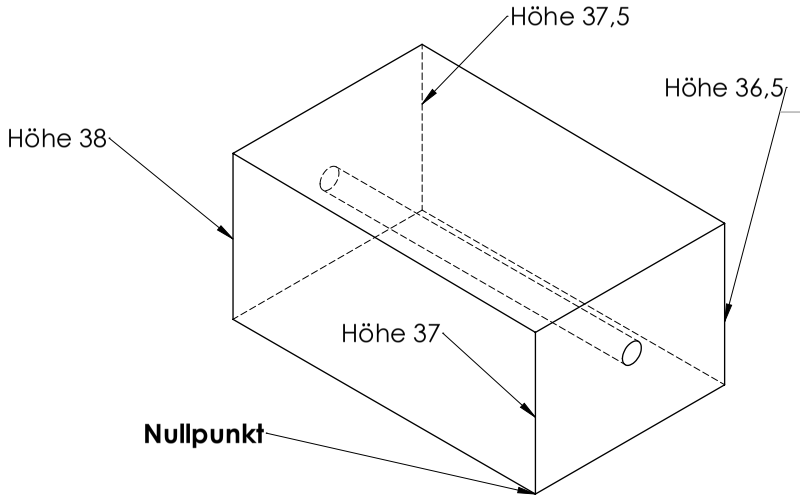

Koordinatenzuordnung nach Blockdimensionen X - Y - Z = 80 x 50 x 38

Alle angegebenen Maße in cm	OBERFLÄCHENGÜTE:				ZEICHNUNG NICHT SKALIEREN	ÄNDERUNG
	NAME	SIGNATUR	DATUM		BENENNUNG:	
GEZEICHNET					Betonblock mit Bohrung	
GEPRÜFT						
GENEHMIGT						
PRODUKTION						
QUALITÄT				WERKSTOFF: Estrich Beton	ZEICHNUNGSNR. FWI4US 01	A3
				GEWICHT: 350 kg		BLATT 1 VON 3

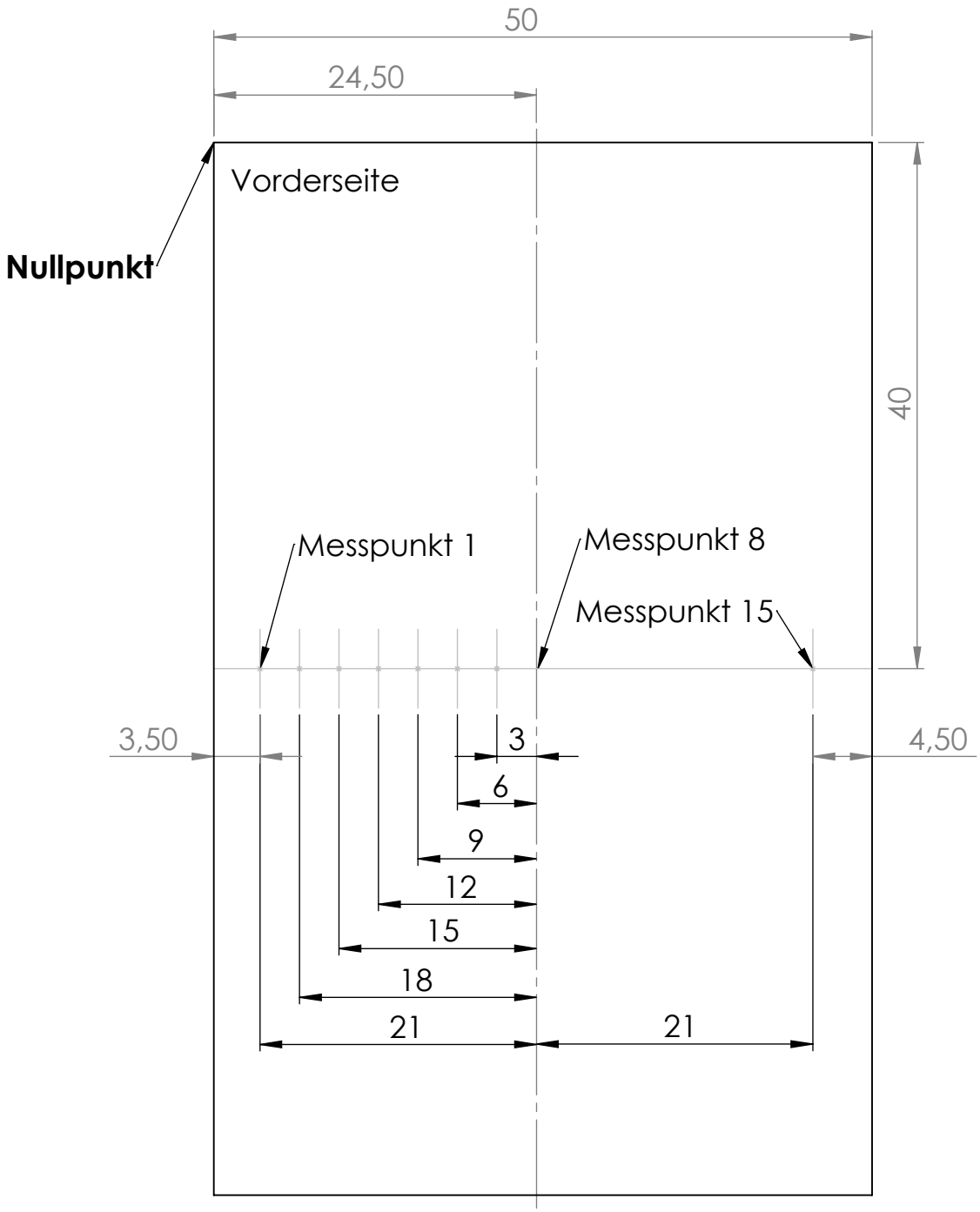

Messungen unter Ausnutzung der Sysmetrie, daher wurden die Messpunkte von der Bohrung nach aussen hin aufgetragen.
Auf der Vorderseite befinden sich die Messpunkte 1 - 15 und auf der Rückseite die Messpunkte 28 - 42.

Alle angegebenen Maße in cm	OBERFLÄCHENGÜTE:			ZEICHNUNG NICHT SKALIEREN	ÄNDERUNG	
	NAME	SIGNATUR	DATUM	BENENNUNG:		
GEZEICHNET				Betonblock mit Bohrung		
GEPRÜFT						
GENEHMIGT						
PRODUKTION						
QUALITÄT				WERKSTOFF:	ZEICHNUNGSNR.	A4
				Estrich Beton	FWI4US 01	
				GEWICHT: 350 kg		BLATT 2 VON 3

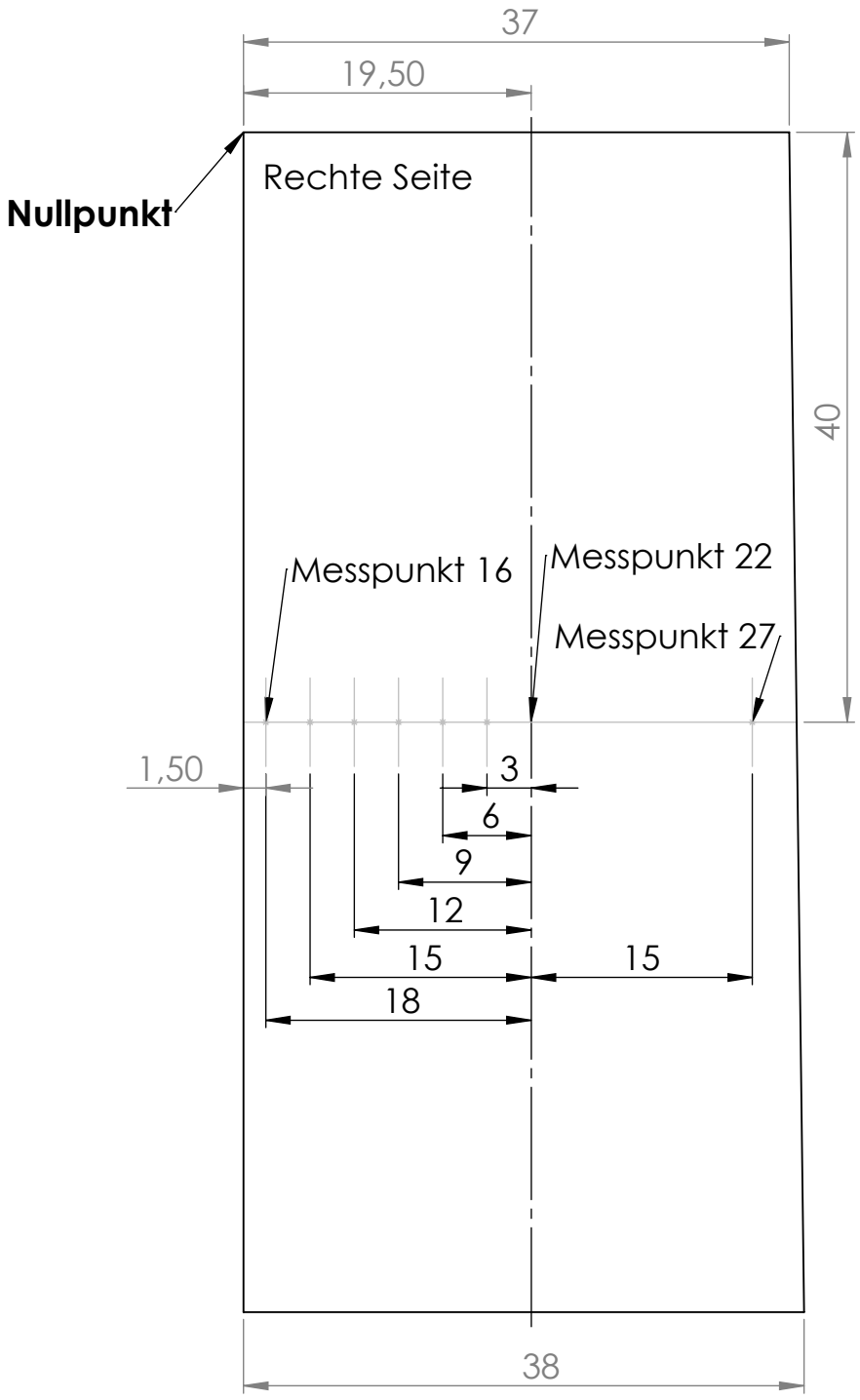

Messungen unter Ausnutzung der Sysmetrie, daher wurden die Messpunkte von der Bohrung nach aussen hin aufgetragen.
Auf der rechten Seite befinden sich die Messpunkte 16 - 27 und auf der linken Seite die Messpunkte 43 - 54.

Alle angegebenen Maße in cm	OBERFLÄCHENGÜTE:	ZEICHNUNG NICHT SKALIEREN	ÄNDERUNG

	NAME	SIGNATUR	DATUM
GEZEICHNET			
GEPRÜFT			
GENEHMIGT			
PRODUKTION			
QUALITÄT			

BENENNUNG:

Betonblock mit Bohrung

WERKSTOFF: Estrich Beton	ZEICHNUNGSNR. FWI4US 01	A4
GEWICHT: 350 kg		BLATT 3 VON 3

Appendix B

Example of a shot with a noisy trace

Figure B.1 shows shot 19. Trace 11 is a noisy trace which I completely muted before applying FWI.

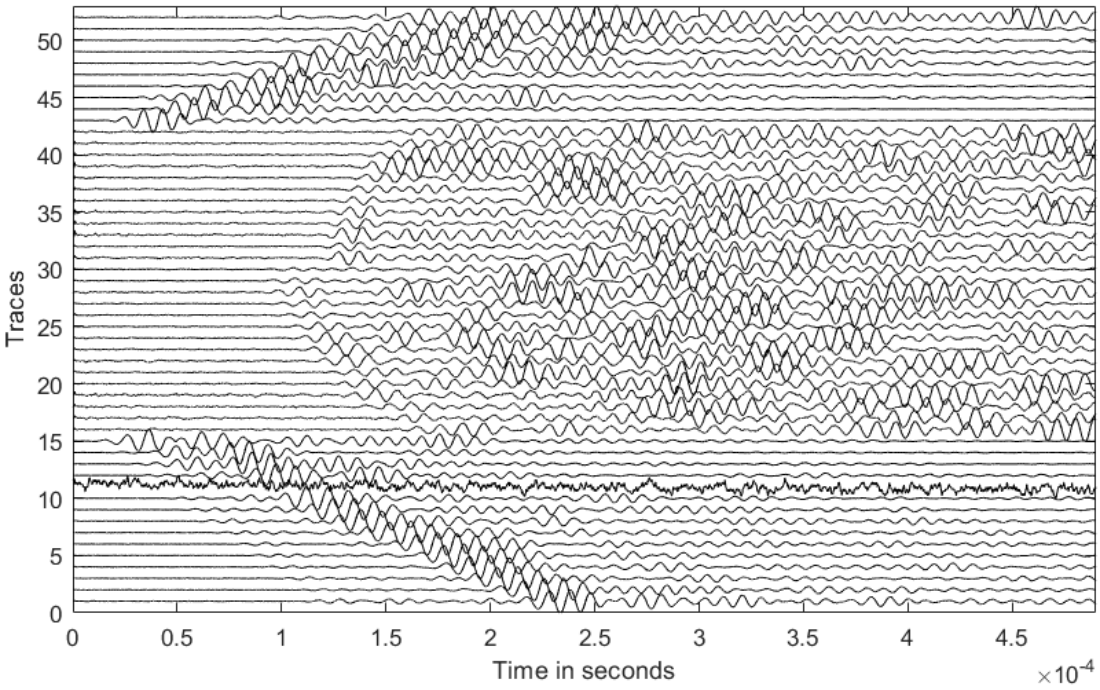

Figure B.1: Shot 19 located at the upper right of the model.